

**OBSERVED AND SIMULATED AIR-SEA FEEDBACKS ASSOCIATED
WITH ENSO AND MONSOON**

A DISSERTATION SUBMITTED TO THE GRADUATE DIVISION OF THE
UNIVERSITY OF HAWAI'I AT MĀNOA IN PARTIAL FULFILLMENT OF
THE REQUIREMENTS FOR THE DEGREE OF

DOCTOR OF PHILOSOPHY

IN

METEOROLOGY

DECEMBER 2011

BY

Baoqiang Xiang

Dissertation Committee:

Bin Wang, Chairperson

Kevin P. Hamilton

Fei-Fei Jin

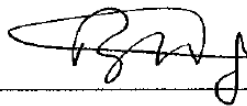
Tim Li

Niklas Schneider

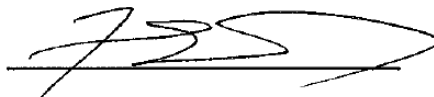
Keywords: Thermocline Feedback, central Pacific warming, Monsoon, western North Pacific Subtropical High

We certify that we have read this dissertation and that, in our opinion, it is satisfactory in scope and quality as a dissertation for the degree of Doctor of Philosophy in Meteorology.

DISSERTATION COMMITTEE



Chairperson



Jim G



Wallas Sauer

ACKNOWLEDGEMENTS

I would like to thank my advisor, Dr. Bin Wang. His continuous and tremendous support, encouragement and excellent guidance throughout my Ph.D. program have made this dissertation work possible. Thanks also are extended to the other members of my dissertation committee: Profs. Kevin Hamilton, Fei-Fei Jin, Tim Li and Niklas Schneider for their time and expertise. Their suggestions and comments led to a significant improvement of this dissertation.

Thanks also go to Drs. Xiouhua Fu, Qinghua Ding and Ping Liu for helping set up the ECHAM AGCM and great contribution to develop the coupled model we used in this dissertation. Great appreciation is also extended to our research group members Hyung-Jin Kim, June-Yi Lee, Yuxing Yang, Owen Shieh, Alejandro Ludert et al. who have improved this work in various ways. I'd also like to thank my friends in the Department of Meteorology at the University of Hawai'i for making my study fun.

A special note of thanks goes to my wife, Wen Liu. Without her love, understanding, patience and support this research would have been impossible. Special thanks also go to my parents, my sisters in-law for their love and support.

TABLE OF CONTENTS

1 Introduction and Motivation	1
1.1 ENSO simulations in current CGCMs.....	1
1.2 El Nino property changes in the recent decade	2
1.3 The interannual variability of the western North Pacific Subtropical High	4
1.4 Objectives and Tasks	6
2 POEM Coupled Model Development and Basic Performance	8
2.1 Introduction	8
2.2 POEM Coupled Model Development.....	9
2.2.1 <i>The POP ocean model</i>	9
2.2.2 <i>The ECHAM atmospheric model</i>	10
2.2.3 <i>Coupling strategies</i>	11
2.3 Data and Experiments	12
2.4 Annual Mean SST and Precipitation	13
2.5 Summer monsoon.....	13
2.6 MJO Simulation	15
2.7 Possible causes of excessive cold tongue extension	16
2.8 Summary and Discussion.....	19
3 Reduction of the thermocline feedback associated with the mean SST bias in ENSO simulation	21
3.1 Introduction	21
3.2 Model, Experiments and Validation data.....	24
3.2.1 <i>Model, Experiments</i>	24
3.2.2 <i>Validation datasets</i>	25
3.3 ENSO simulations.....	25
3.4 Air-sea coupling strength	27
3.5 Wind-thermocline coupling and thermocline-subsurface temperature coupling	29
3.6 Equatorial mean upwelling	31
3.6.1 <i>Dynamics determining the equatorial upwelling</i>	31

3.6.2	<i>Dynamic impacts associated with surface wind stress forcing</i>	33
3.6.3	<i>Thermodynamic impacts associated with upper-ocean convective mixing</i>	35
3.7	Summary and discussions	38
4	Predominance of the central Pacific El Nino after the late 1990s	45
4.1	Introduction.....	45
4.2	Data, Model and Methodology	46
4.3	Observed El Niño property change after the late 1990s.....	47
4.4	A new paradigm for the dominance of the CP-El Niño	49
4.5	Possible mechanism for the La Nina-like mean state change	54
4.6	Summary and Discussion.....	56
5	Dynamics and Predictability of the western North Pacific Subtropical High	58
5.1	Introduction	58
5.2	Data and Methodology.....	59
5.3	Results.....	61
5.3.1	<i>Dynamics controlling the variability of the WNPSH</i>	61
5.3.2	<i>Predictability of the WNPSH</i>	65
5.4	Summary and Discussion	66
6	Summary and Future Work	69
6.1	Summary	69
6.1.1	<i>Mean SST bias in the newly developed coupled model POEM</i>	69
6.1.2	<i>Reduction of the thermocline feedback associated with mean SST bias in ENSO simulation</i>	70
6.1.3	<i>Predominance of the central Pacific El Nino after the late 1990s</i>	71
6.1.4	<i>Dynamics and predictability of the WNPSH</i>	72
6.2	Future Work.....	72
	References	75

List of Tables

<u>TABLE</u>	<u>PAGE</u>
Table 2.1 List of experiments designed in this chapter	20
Table 3.1 List of experiments designed in this chapter	42
Table 3.2 List of models that participate in this study	43
Table 3.3 Quantitative evaluation of the individual coupling related to the thermocline feedback from observations, AMSC, and CTRL	44
Table 4.1 Cases of this new type of El Niño for different definitions.	57
Table 4.2 List of experiments designed in this chapter	57

List of Figures

Figure 1.1 a) Global mean temperature anomalies ($^{\circ}\text{C}$) derived from HadCRUT3 [Brohan *et al.*, 2006]. b) Equatorial (2°S - 2°N) SSH difference (cm) between the two epochs, 1999-2010 minus 1980-1998. Here the change of SSH signifies the change in thermocline depth. The orange lines mark the edge of the central Pacific where the maximum SST warming occurs but the thermocline depth becomes even deeper after the late 1990s.

Figure 2.1 Component of the coupled model POEM.

Figure 2.2 Left panel: Time-mean SST ($^{\circ}\text{C}$) from a) ERSST, b) CTRL, and c) CTRL-ERSST difference. Right panel: Time-mean precipitation (mm day $^{-1}$) from d) GPCP, e) CTRL, and f) CTRL-GPCP difference.

Figure 2.3 Boreal summer (JJA) mean precipitation (mm day $^{-1}$) from a) GPCP, b) POEM. The red boxes represent three major monsoon systems, the Indian Summer monsoon, the equatorial eastern Indian Ocean, the western North Pacific monsoon.

Figure 2.4 The first 3 leading EOF modes of boreal summer (JJA) precipitation from GPCP. a), b), c) are the corresponding spatial pattern of these three modes. The time series are shown in the lower right panel.

Figure 2.5 Same as Fig. 2.4 but from POEM.

Figure 2.6 Percentage of the variance of 20-100 day bandpass filtered zonal wind (850 hPa) to the total variance from ERA40 (upper panel) and POEM (lower panel). The left panel is for boreal winter (Nov-Apr) and the right panel is for boreal summer (May-Oct).

Figure 2.7 The first four leading EOF modes of 850 hPa zonal wind with 20-100 bandpass filtering during boreal winter. The left panel is from ERA40 and the right is from POEM.

Figure 2.8 The same as 2.7 but for boreal summer season.

Figure 2.9 Wavenumber-frequency spectra of 10N-10N averaged 850 hPa zonal wind ($\text{m}^2 \text{s}^{-2}$) for the ERA40 (upper panel) and POEM (lower panel). The left panel is for boreal winter season and the right panel is for boreal summer season.

Figure 2.10 a) time-mean SST difference ($^{\circ}\text{C}$) between a) CTRL and observations, b) OCN_obs and observations, c) CTRL and OCN.

Figure 2.11 Equatorial (5°S - 5°N) heat flux (upper panel in W m^{-2}) and surface wind stress (lower panel in N m^{-2}) from observations (solid), AMIP (dashed) and CTRL (circle). In the upper panel, red line/circle represents the shortwave radiation and blue line/circle denotes the latent heat flux. The corresponding black line/circle shows the net heat flux.

Figure 2.12 Time mean SST difference between OCN and OCN_obs experiments. Surface wind stress difference is shown as vectors (only shown when magnitude greater than 0.15 dyn cm^{-2}).

Figure 3.1 a) Horizontal map of the annual mean SST correction term (units: $^{\circ}\text{C}$ per 5 days), time-mean b) SST bias (AMSC-ERSST) and c) precipitation bias (AMSC-GPCP) for the AMSC run.

Figure 3.2 Standard deviations of SSTA ($^{\circ}\text{C}$) from a) ERSST, b) CTRL, c) AMSC, d) the ratio of CTRL-AMSC and AMSC (percent)..

Figure 3.3 Precipitation (shading in $\text{mm day}^{-1} \text{ } ^{\circ}\text{C}^{-1}$) and surface zonal wind stress (contours in $10^{-3} \text{ Nm}^{-2} \text{ } ^{\circ}\text{C}^{-1}$) anomaly regressed onto Niño-3 index from a) GPCP/ERA40, b) CTRL, and c) AMSC. By using a dry AGCM, the right panel (d-f) shows the low level wind response (contours in m s^{-1}) to the prescribed mid-tropospheric forcing with the same regressed precipitation pattern from the left panel.

Figure 3.4 a) Time-mean 1000 hPa wind speed (m s^{-1}) for AMSC, b) Time-mean 1000 hPa wind speed difference between CTRL and AMSC.

Figure 3.5 Thermocline depth (Z20) anomaly regressed onto equatorial zonal wind stress anomaly averaged over $160^{\circ}\text{E}-130^{\circ}\text{W}$, $5^{\circ}\text{S}-5^{\circ}\text{N}$ (in $\text{m cm}^2 \text{ dyn}^{-1}$) for the a) CTRL, b) AMSC. Zonal wind stress anomaly regressed onto equatorial zonal wind stress anomaly averaged over $160^{\circ}\text{E}-130^{\circ}\text{W}$, $5^{\circ}\text{S}-5^{\circ}\text{N}$ for the c) CTRL, d) AMSC.

Figure 3.6 Equatorial ($2^{\circ}\text{S}-2^{\circ}\text{N}$) temperature anomaly (shading in $^{\circ}\text{C m}^{-1}$) regressed onto equatorial thermocline depth anomaly averaged over $180^{\circ}-80^{\circ}\text{W}$, $2^{\circ}\text{S}-2^{\circ}\text{N}$ for the a) CTRL, b) AMSC, c) CTRL-AMSC. Contours in the a), b) are the

corresponding climatological temperature. Contours in c) is the climatological temperature difference between the CTRL and AMSC.

Figure 3.7 Time-mean equatorial (2°S-2°N) upwelling (shading in m day^{-1}) from a) CTRL, b) AMSC, and c) CTRL-AMSC difference.

Figure 3.8 a) Time-mean equatorial (5°S-5°N) zonal wind stress (dyn cm^{-2}) from the CTRL (black) and AMSC (red). b) Time-mean differences between CTRL and AMSC of SLP (shading in Pa) and surface wind stress (vectors with magnitude greater than 0.1 dyn cm^{-2}), c) same as b) but for precipitation (shading in mm day^{-1}) and 850 hPa wind (vectors with magnitude greater than 0.4 m s^{-1}).

Figure 3.9 a) Time-mean difference of a) SST ($^{\circ}\text{C}$), b) mixed layer depth (m), and c) equatorial (2°S-2°N) mean upwelling (m day^{-1}) differences between CTRL and OCN.

Figure 3.10 a), c) the meridional and zonal currents (cm s^{-1}) differences between CTRL and OCN averaged over the upper 30 m. b), d) are the corresponding meridional gradient of meridional currents and zonal gradient of zonal currents ($\times 10^{-7} \text{ s}^{-1}$).

Figure 3.11 Time-mean meridional currents (cm s^{-1}) averaged over the upper 30 m from a) CTRL, b) OCN. Vertical-Longitudinal diagram of time-mean meridional currents from c) CTRL, d) OCN. Contours in d) indicates the corresponding meridional currents difference between CTRL and OCN.

Figure 3.12 Time-mean horizontal viscous stress ($\text{cm}^2 \text{ s}^{-2}$) along a) 2.8°N and b) 2.8°S. The black and red lines indicate the results from the CTRL and OCN

experiments, respectively. The green line shows the difference between CTRL and OCN.

Figure 3.13 Estimated meridional Ekman currents (cm s^{-1}) from CTRL (black) and OCN (red) along 2.8°S and 2.8°N , based on the zonal viscous stress shown in Fig. 3.12.

Figure 3.14 Thermal damping measured by the monthly heat flux anomaly regressed onto Niño-3 SSTA for observations (upper), CTRL (middle) and AMSC (bottom). The left panel is for net heat flux, the middle for solar radiation and right panel for latent heat flux. Units: $\text{W/m}^2/\text{C}$.

Figure 3.15 The SST bias ($^{\circ}\text{C}$) from 12 CGCMs in comparison to the ERSST climatology. The period 1980-1999 is chosen to be consistent with the AMIP run.

Figure 3.16 The equatorial (5°S - 5°N) zonal wind stress (dyn cm^{-2}) differences between the fully coupled run and AMIP run.

Figure 3.17 Air-Sea coupling strength ($10^{-3} \text{Nm}^{-2} \text{C}^{-1}$) from ERA40 (black), NCEP (grey), AMIP runs (orange) and the corresponding coupled runs (dark cyan).

Figure 3.18 The power spectrum of the Niño-3 index from the CTRL (left) and AMSC (right). The unit of horizontal axis is years.

Figure 3.19 Lead-lag correlation between equatorial (5°S - 5°N) thermocline depth (SSH) anomaly and the zonal wind stress curl ($-\text{dTaux}/\text{dy}$) over the equatorial central Pacific (160°E - 130°W , 5°S - 5°N). Positive in the lead time means the

zonal wind stress curl leads the equatorial thermocline depth anomaly. The zonal wind stress curl multiplies -1 in the southern hemisphere.

Figure 3.20 Thermocline depth (SSH) change regressed onto the zonal wind stress curl ($-dT_{\text{aux}}/dy$) over the equatorial central Pacific (160°E-130°W, 5°S-5°N). The thermocline anomaly lags the surface wind stress curl anomalies 9 months. The zonal wind stress curl multiplies -1 in the southern hemisphere.

Figure 4.1 a) Epochal SST difference (1999-2010 minus 1980-1998) (°C), b) annual mean SST correction term (units: °C per 5 days) in the EXP_AO.

Figure 4.2 Longitude-time diagram of the equatorial (5°S-5°N) SSTA for 10 cases. The years with read marks denote the robust and standing CPW cases.

Figure 4.3 The leading EOF of monthly mean SSTA in the tropical Pacific domain during a) 1980-1998 and b) 1999-2010. The fractional variance that can be explained is 60.9%, 60.0%, respectively. c) and d) Linear regression of precipitation (shading in mm/day) and surface zonal wind stress (contours in dyn/cm^2) onto the time series of EOF-1 mode during these two epochs as shown in e) and f), respectively.

Figure 4.4 Evolution of the composite EPW (1982, 1997, upper panel), and CPW (2002, 2004, 2009, lower panel) averaged between 2°S and 2°N. Panels a) and c) show the anomalous zonal wind stress (shaded in dyn/cm^2) and precipitation (contours in mm/day). Panels b) and d) display the SSTA (shaded in °C) and

SSH anomaly (contours in cm). Note that the SSTA in b) and d) uses different intervals.

Figure 4.5 Epochal difference (1999-2010 minus 1980-1998) of a) SST ($^{\circ}\text{C}$), b) precipitation (mm/day), c) low-level (1000 hPa) wind convergence ($\times 10^{-7} \text{ s}^{-1}$), and d) SSH (shading in cm) and surface wind stress (dyn/cm²).

Figure 4.6 Mean low-level (1000 hPa) wind convergence ($\times 10^{-7} \text{ s}^{-1}$) during a) 1980-1998, b) 1999-2010.

Figure 4.7 Annual cycle change of the equatorial (2°S - 2°N) a) precipitation (shading) and SST (contours), b) SSH (shading) and zonal surface wind stress (contours).

Figure 4.8 Time evolution of composite SSH (shading in cm), SST (contours in $^{\circ}\text{C}$) and surface wind stress (dyn/cm²) anomalies from July-August (JA) in the developing year to May-June (MJ) in the next year. Three CPW cases are used, 2002, 2004, 2009. Here ‘0’ denotes the El Nino developing year and ‘1’ for the decaying year.

Figure 4.9 a), b) The first two leading EOF modes (shading) of SSH anomaly during 1999-2010. The contours in a) and b) are the linear regression of zonal current anomaly (cm/s) averaged over upper 35 m onto the time series of these two modes as shown in panel c). The fractional variance that can be explained by these two modes are 43.5%, 9.5%, respectively.

Figure 4.10 a), b) The first two leading EOF modes (shading) of SSH anomalies during 1980-1998. c) the time series of these two EOF modes.

Figure 4.11 The linear trend of SSTA ($^{\circ}\text{C}$ per decade) for the period between 1950 and 2000 from a) ERSST and b) HadISST [Rayner *et al.*, 2003]. The reason to use this period is twofold: The most evident global warming occurs during this period and large uncertainty for the SST data exists before 1950 due to the lack of observations over ocean.

Figure 4.12 Time-mean a) SST, b) precipitation and 850 hPa wind differences between EXP_AO and AMSC.

Figure 4.13 the same as Figure 4.11 but for boreal winter (DJF).

Figure 5.1 a) Standard deviation of H850 (black contours in m). The red contour line (5870 m at 500 hPa) outlines the western North Pacific Subtropical High (WNPSH). b) The normalized WNPSH index defined by the H850 anomaly averaged over the green box indicated in a). Blue dashed lines represent 70% of the standard deviation of the WNPSH index. c), The regressed patterns of 850 hPa wind vectors (not shown when smaller than 0.2 m/s) and precipitation (shading) onto the normalized WNPSH index during JJA.

Figure 5.2 The 3-month running mean WNPSH index (red) and Nino 3.4 SSTA (blue) for the 9 strong WNPAC years. JJA season is indicated by circles in the WNPSH index. Note that only 4 cases (1983, 1988, 1995, and 1998) occurred during El Niño decay summers.

Figure 5.3 Summertime (JJA) SSTA during 9 strong WNPAC cases. Note that 4 cases do not accompanied by Indian Ocean warming (1980,1993, 1995, and 1996).

Figure 5.4 a), b) The spatial patterns of the first two leading EOF modes of Asian summer (JJA) monsoon precipitation anomaly during 1979-2009. The fractional variance that can be explained by these two modes are 21.1%, and 9.9%, respectively. c) The corresponding principal components, PC-1 and PC-2 with the WNPSH index. The correlation coefficients of the WNPSH with the PC1 and PC2 are 0.58 and 0.56, respectively.

Figure 5.5 a) Interannual variations of the WNPSH intensity, East Asian summer monsoon (EASM) strength (reversed) and the total number of TS days (TSDs, reversed) over the subtropical WNP (20°N-35°N, 110°E-165°E). The WNPSH intensity is defined by the normalized H850 anomaly averaged over its maximum variability center (15°N-25°N, 115°E-150°E). The EASM strength is measured by the leading principal component of the precipitation, 850 and 200 hPa winds of the EASM system. The numbers in the brackets indicate correlation coefficients with the WNPSH intensity. The purple (green) polygons in the time series of WNPSH index indicate the strong (weak) WNPSH years with anomalous amplitudes exceeding 0.7 standard deviations. b), The long-term mean TSDs in JJA (contours in days per year) and the difference (shading) between 9 strongest and 9 weakest WNPSH years. The red line in b) shows the

coastal regions of TS landing. The interannual variation of the landing TS numbers has a significant correlation with the WNPSH ($r=0.66$).

Figure 5.6 a) The spatial pattern of H850 anomaly (contours) and correlated precipitation (shading). b) the corresponding principal component (PC-1). c) The correlated SSTA (shading) and 850 hPa wind anomalies. The correlation fields were made with reference to PC-1 and only correlations significant at 10% confidence level ($r>0.3$) are shown. d) Simulated JJA H850 (black contours in m) and precipitation (shading in mm/day) anomalies with ECHAM4 model forced by prescribed cold SSTA (red contours with interval of $0.1\text{ }^{\circ}\text{C}$).

Figure 5.7 Left panel: Schematic diagram to show the IO-WNP anticyclonic coupled mode. The double arrows denotes the mean flow in boreal summer (JJA). The red (blue) shading regions indicate the SST warming (cooling). The heavy lines wind arrows show the anomalous circulation. Right panel: JJA mean SST (shading) and 1000 hPa wind (vectors).

Figure 5.8 Same as Fig. 5.7d but for boreal spring (March-May) mean state. The solid red lines outline the SSTA forcing.

Figure 5.9 a) The correlation between PC-1, and 1000 hPa wind speed (shading), and SSTA (contours). b) Surface latent heat flux regressed onto PC-1 (shading, negative means loss heat flux from ocean surface), and the correlation between PC-1 and SSTA (contours).

Figure 5.10 a), b), c) are the same as Figure 5.7 but for EOF-2 mode. d) Low-level vorticity (contours in 10^{-7} m/s^2) in response to a mid-tropospheric heating (colour)

obtained from an intermediate atmospheric model with boreal summer (JJA) mean flow.

Figure 5.11 Atmospheric low-level vorticity responses ($\times 10^{-7} \text{ s}^{-1}$, contours) to the prescribed Pacific cooling (left panel) and maritime continental heating (right panel) (colour) in an intermediate atmospheric model. Upper panel shows the experiments without mean flow and the lower panel is with boreal summer (JJA) mean flow. Note that in the presence of mean flows, the response is enhanced over the monsoon regions due to the fact that a background easterly vertical shear can amplify Rossby wave responses (Wang and Xie 1996).

Figure 5.12 a) Reconstruction of the JJA WNPSH index with the first two principal components. Shown are the normalized WNPSH index (black) and the reconstructed (red) index based on PC1 and PC2 ($1.226 \times \text{PC-1} + 1.245 \times \text{PC-2}$). They have a correlation coefficient of 0.94. b) The observed WNPSH index (black) and the model simulated index (red) and re-forecasted index (blue). The simulation of the WNPSH intensity was made based on the Eq. (1) (See text). The correlation between the observed WNPSH index and the simulated (re-forecasted) WNPSH index is 0.81 (0.75).

Figure 5.13 Selection of predictors based on the correlation maps between a, the WNPSH (JJA) index and the April-May mean SSTA, b) the WNPSH (JJA) index and the May-minus-March SSTA, and c, the NAO (April-May) index and boreal summer (JJA) SSTA. Only values with significance level above 90% are

shown. The boxes in the panels a and b indicates the area where area-averaged SSTAs are selected for constructing the corresponding predictors.

Figure 5.14 The observed WNPSH index (black) from 1982 to 2005. The red line denotes the multi-model ensemble (MME) result using the June 1st initial condition (zero-month lead forecast). Results from three individual models (NCEP, GFDL, ABOM) are shown by dashed lines. The correlation between the observed WNPSH index, and MME, NCEP, GFDL, ABOM are 0.82, 0.73, 0.80, and 0.76, respectively. The hindcast experiments data were provided by NCEP (National Center for Environmental Prediction), GFDL (Geophysical Fluid Dynamics Laboratory), and ABOM (Australian Bureau of Meteorology) through APEC Climate Center(APCC)/ climate prediction and application to society (CliPAS) project (Wang et al. 2008, Lee et al. 2011).

Figure 5.15 Low level wind (vectors) and geopotential height response to the prescribed heating (shading in K/day) with a) no mean flow, b) boreal summer (JJA) mean flow. c) is the difference between b) and a). d) mean vertical shear (m/s) during JJA by the zonal wind difference between 200 hPa and 850 hPa. The model we used here is a two and half layer atmospheric model (Wang and Li 1993).

Figure 5.16 a) Summertime (JJA) SST difference between two epochs, 1999-2009 and 1979-1998. b) SSTA averaged over the blue box in a) during JJA. The blue box is the location of the WNP cooling associated with EOF-1.

Figure 5.17 a) The normalized WNPSH index (JJA) during 1948-2009 from NCEP-NCAR reanalysis dataset (Kalnay et al., 1996). b) The standard deviation of the WNPSH index with a 13-year window that moves year by year.

Abstract

Associated with the double ITCZ (Inter-tropical convergence zone) problem, a dipole SST bias pattern (cold in the equatorial central Pacific and warm in the southeast tropical Pacific) remains a common problem in current coupled models. Based on a newly-developed model, we demonstrated that a serious consequence of this SST bias is to suppress the thermocline feedback in El Niño/Southern Oscillation (ENSO) simulation. Firstly, the excessive cold tongue extension pushes the anomalous convection far westward, diminishing the convection-low level wind feedback and thus the air-sea coupling strength. Secondly, the equatorial surface wind anomaly exhibits weak meridional gradient, leading to a weakened wind-thermocline feedback. Thirdly, the equatorial cold SST bias induces a weakened upper-ocean stratification, yielding the underestimation of the thermocline-subsurface temperature feedback. Finally, the dipole SST bias underestimates the mean upwelling through both dynamic and thermodynamic effects.

In recent decades, El Niño events have occurred more frequently over the equatorial central Pacific (CP Warming, CPW). Here, we ascribe this predominance of the CPW to a dramatic decadal change in the Pacific mean state and annual cycle. The mean state change characterized by a decadal La Niña-like pattern tends to anchor convection and surface zonal wind anomalies to the vicinity of the dateline, facilitating surface warming to occur in the CP. The annual cycle change, with the trade winds intensifying during boreal winter and spring, prevents the warming

development but helps the warming decay in the EP. More CPW events are expected in the coming decade if the La-Niña-like pattern persists.

The western North Pacific (WNP) Subtropical High (SH) has profound impacts on Asian summer monsoon, North Pacific storms. The cause of the interannual variability of WNPSH, however, remains controversial. Here we show that the anomalous WNPSH is primarily determined by a remote cooling/warming in the equatorial central Pacific and a positive thermodynamic feedback between the local circulation and a dipole sea surface temperature in the Indo-Pacific warm pool. We demonstrate that a physical-empirical prediction model built on these physical understandings has comparable performance with those of three state-of-the-art coupled climate models in re-forecast of the strength of the WNPSH.

Chapter 1

Introduction and Motivation

1.1 ENSO simulations in current CGCMs

El Niño/Southern Oscillation (ENSO) acts as the strongest and most dominant mode on interannual time scale, which exerts worldwide impacts on climate, agriculture, and ecosystems. Coupled General Circulation Models (CGCMs) provide one important tool for the ENSO simulation and forecast. Although the ENSO simulation in the CGCMs has achieved steady progresses in recent decades (Mehoso et al. 1995; Latif et al. 2001; AchutaRao and Sperber 2002; Meehl et al. 2005; Randall et al. 2007), the simulated ENSO characteristics in terms of amplitude, period, irregularity, skewness and spatial pattern, still remain unrealistic in various degrees (e.g. Guilyardi 2006; AchutaRao and Sperber 2006; Guilyardi et al. 2009b). For example, some models have either too strong or too weak ENSO amplitude; some models show too short and regular period; some models have narrow meridional extension but too far westward extension (e.g., Guilyardi et al. 2009b).

Kim and Jin (2010) investigated the ENSO simulated by the CGCMs from Intergovernmental Panel on Climate Change (IPCC) Fourth Assessment Report (AR4) and concluded that the majority of current CGCMs underestimate the thermocline feedback. As a dominant process controlling the evolution of ENSO, weakened thermocline feedback would reduce the simulated ENSO amplitude. Meanwhile, the ENSO periodicity is largely controlled by the relative importance from the thermocline

feedback and zonal advection feedback, so that a weaker thermocline feedback is conducive to a relatively shorter ENSO cycle, and vice versa (An and Jin 2001; Fedorov and Philander 2000). Therefore, investigating the cause of the weak thermocline feedback is of particular importance for the further improvement of the ENSO simulation.

The double ITCZ (Inter-tropical convergence zone) problem characterized by excessive precipitation off the equator but insufficient precipitation on the equator is a long standing but challenging tropical bias existing in the last several generations of CGCMs. This double ITCZ problem is often accompanied by warm SST bias in the southeast Pacific (SEP) and an excessive and overly SST cold tongue that extends too far west into the western Pacific (Lin 2007). The question arises, whether and how this mean SST state bias could influence the thermocline feedback in ENSO simulation. Understanding this is expected to guide the improvement of ENSO simulation in coupled climate models, and may also provide important clues applicable to the study of ENSO property changes in a future warmer climate.

1.2 El Nino property changes in the recent decade

It is well known that ENSO experiences significant decadal changes after the mid-1970s, with respect to its intensity, periodicity and propagations (e.g., Wang 1995; An and Wang 2000). Usually the maximum interannual warming or cooling takes places over the equatorial eastern Pacific (EP), however, some recent studies found that one new type of El Nino with its maximum warming over the central Pacific (CP) has occurred more frequently recently (Larkin and Harrison 2005; Ashok et al. 2007; Kao and Yu 2009; Kug et al. 2009; Yeh et al. 2009). At the same time, the intensity of the central

Pacific Warming (CPW) has almost doubled in the past three decades (Lee and McPhaden 2010). In contrast to the conventional El Niño in the EP (eastern Pacific Warming, EPW), the CPW exhibits different impacts on worldwide climate, including a shift of anomalous equatorial convection (Weng et al. 2007; Weng et al. 2009), increased effectiveness in causing Indian drought (Kumar et al. 2006), reduction of rainfall along the west coast of North America (Weng et al. 2007), and increased hurricane frequency in the Atlantic Ocean (Kim et al. 2009a). Hence exploring the cause of this observed location shift of El Niño is critical for climate prediction and understanding the potential future changes of ENSO.

A recent study suggested that the westward shift of El Niño to the CP is due to anthropogenic forcing-induced global warming, which causes weakened trade winds and resultant thermocline flattening so that the thermocline feedback was suggested to be intensified over the CP (Yeh et al. 2009). However, this hypothesis is not well supported by investigating the El Niño property changes and the associated mean state changes in recent decades, especially after the late 1990s.

1) The leading empirical orthogonal function (EOF) mode of tropical SST anomaly has changed from an EP-type to a CP-type El Niño after 1998. However, the equatorial thermocline becomes more east-west tilted simultaneously and not shallower than before in the CP (Fig. 1.1). This structure is also apparent by examining the temperature trend within the recent three decades that shows anomalous temperature warming over the WP but cooling in the EP (not shown).

2) The global mean surface temperature has leveled off after the late 1990s (Fig. 1.1a) (Soloman et al. 2010), and the Walker circulation seems to be intensified together with

enhanced trades. Further, in the tropical Pacific the epochal mean SST difference (1999-2010 minus 1980-1998) features a La Niña-like global warming (Deser et al. 2010; Kucharski et al. 2011), which differs from the El Niño-like global warming pattern projected by ensemble means of 22 climate models that participated in the World Climate Research Program/Coupled Model Inter-comparison Project 3 (CMIP3) (Vecchi and Soden 2007).

3) Under global warming, thermocline depth is shallower but the mean upwelling also tends to be weakened associated with the weakened trades, so that the thermocline feedback may change little (Kim and Jin 2010).

4) Caution should be exercised when using reconstructed SST data, because the inferred SST before 1950s likely contains information of EPW embedded into (Giese and Ray 2011). Intriguingly, an ocean reanalysis suggests that the CPW dominates over the period between 1880s and 1950s without significant global warming contribution (Giese and Ray 2011).

The above arguments and evidences imply that the observed El Niño property changes in the last three decades must involve other mechanisms other than this global warming-induced uplifted thermocline mechanism. In this study, we provide an alternative hypothesis that decadal mean state change is critical in determining the Niño property changes especially after the late 1990s.

1.3 The interannual variability of the western North Pacific

Subtropical High

The western North Pacific subtropical high (WNPSH) is a primary circulation system of the East Asia (EA)-WNP summer monsoon (Tao and Chen 1987). The anomalous WNPSH arising from the changes in its intensity and position has profound impacts on the EA-WNP monsoon rainfall (Nitta 1987; Huang and Wu 1989) and downstream over North America (Wang et al. 2001; Lau and Weng 2002). The prominent WNP anticyclonic anomaly occurring during a decaying El Niño (or transition to La Nina events) conveys a delayed impact of ENSO to enhance EA subtropical rainfall (Wang et al. 2000; Chang et al. 2000) and to reduce dramatically WNP tropical cyclones (Wang and Chan 2002). The anomalous WNP anticyclone (AC) emerges during the fall of an El Niño developing year over the northern Philippine island (Wang and Zhang 2002), and develops in northern winter and by spring becomes a dominant anomalous system in the entire Asian-Australian monsoon system (Wang et al. 2003). From the fall to the ensuing spring, two mechanisms have been recognized to be critical to the development and maintenance of the WNPSH: a remote forcing from anomalous central Pacific warming (Zhang et al. 1996) and a positive thermodynamic feedback between convectively coupled Rossby waves and the underlying SST cooling (Wang et al. 2000; Lau et al. 2005).

However, exactly how this anticyclonic anomaly maintains itself against dissipation during the following summer remains a fundamental but highly debated issue. The Indian Ocean (IO) warming after the peak El Niño is positively correlated with the intensity of the anomalous WNPSH and EA summer precipitation (Ye and Huang 1996). Wu and Liu (1995) demonstrated that an anomalous warming in the equatorial IO can induce enhanced WNPSH using numerical experiments. This view has been amplified by some

recent studies (Yang et al. 2007; Wu et al. 2009; Kim et al. 2009b; Li et al. 2008; Xie et al. 2009; Chowdary et al. 2010). However, a key problem is that the most significant IO warming is not collocated with enhanced precipitation and the atmosphere cannot feel warm SST effect without invoking precipitation heating. Further, in the heavily precipitating summer monsoon region, SST is essentially not a cause but sometimes a result of the atmospheric forcing (Wang et al. 2005). As such, the linkage between the WNPSH and the anomalous IO SST warming remains as an important issue for deliberation.

Most of previous studies focused on the anticyclonic activities over the WNP following El Nino year, however, we notice that many strong anomalous WNPSH years are not related to the El Nino decay years. It indicates that some other processes may also play some role in governing the anomalous WNPSH. This calls for further investigation of the dynamics controlling the interannual variability of the WNPSH, which may help predict the interannual variability of the WNPSH.

1.4 Objective and Tasks

As mentioned above, some issues associated with ENSO and monsoon are not well understood. Here we tend to address the following several issues related to ENSO and monsoon. First, we build an ocean-atmosphere coupled model which exhibits serious double ITCZ problem associated with excessive cold tongue extension and warm SST bias over the SEP. Based on this coupled model, we will examine how this dipole SST bias influences the simulation of thermocline feedback which holds key for ENSO evolution. Second, we try to explore the possible reasons for the more frequent

occurrence of CPW particularly in the recent decade. Here we propose one possible explanation for the more frequent occurrence of CPW by emphasizing the decadal mean state and annual cycle changes. This newly developed coupled model will be employed to testify the hypotheses we proposed about the mechanism leading to the mean state change. Finally, we will investigate the mechanisms controlling the interannual variability of the WNPSH. Based on this, we will further build an empirical model to predict the interannual variability of the WNPSH. The data, models and methodology are described in each chapter.

Chapter 2

POEM Coupled Model Development and Basic Performance

2.1 Introduction

We have developed a coupled model, which couples the Parallel Ocean Program (POP, v2.0) ocean model (Smith et al. 1992; Dukowicz and Smith 1994) and the Max-Planck-Institute (MPI) ECHAM (v4.6) atmosphere model (Roeckner et al. 1996) via the Ocean-Atmosphere-Sea Ice-Soil (OASIS, v3.0) coupler (Valcke et al. 2003). The main purpose to develop this coupled model is to study the dynamics and interactions among ENSO, monsoon and MJO. For convenience, hereinafter we refer to it as the POEM coupled model (Fig. 2.1). The POP is a descendent of the Bryan-Cox-Semtner class of ocean models first developed by Kirk Bryan and Michael Cox (Brown 1969) at the NOAA Geophysical Fluid Dynamics Laboratory (GFDL) in Princeton in the late 1960s. It is also the ocean component of the CESM (Community Earth System Model) climate model. The atmospheric model we used here is the ECHAM model in that the ECHAM family usually has relatively better monsoon, MJO (Madden-Julian Oscillation) simulations (Sperber and Annamalai 2008).

The major purpose to develop this coupled model is to study the dynamics, prediction and interactions among ENSO, monsoon and MJO. In this chapter, we aim to introduce the basic performance of POEM and discuss the potential processes resulting a dipole SST bias pattern. The chapter is organized as the following. Section 2.2 briefly describes the individual component of the coupled system. Section 2.3 described the data and experiments. The annual mean SST and precipitation are introduced in section 2.4.

Section 2.5 and 2.6 present the simulations of boreal summer monsoon and MJO, respectively. In section 2.7, we further discuss the possible causes of excessive cold tongue extension in POEM coupled model. Finally, we summarize the results in section 2.8.

2.2 POEM Coupled Model Development

2.2.1 The POP ocean model

The POP (v2.0) ocean model is developed at Los Alamos National Laboratory under the sponsorship of the Department of Energy's CHAMMP program (Smith et al. 1992; Dukowicz and Smith 1994). The original motivation to develop the POP model is to improve massively parallel computation. But the current version of POP model also substantially improves model physics in realistic representation of the ocean, for example, the treatment of the barotropic mode, free-surface boundary condition and general orthogonal horizontal coordinates. The most significant improvements can be found in Smith et al. (1992) and Dukowicz et al. (1993).

This model is a Bryan-Cox-type, level-coordinated model with Boussinesq approximation. The model solves the primitive equations in general orthogonal coordinates in the horizontal direction subject to the hydrostatic approximation. The barotropical equation is solved by using a linearized, implicitly free-surface formulation. The Gent and McWilliams (1990) horizontal isopycnal transport scheme is adopted for tracer equations. The main advantage to use Gent and McWilliams scheme is to include the eddy effect and limit climate drift for coupled model. The momentum equations use

the anisotropic horizontal viscosity. The K-profile parameterization (KPP, Large et al. 1994) is used to determine vertical mixing.

The KPP scheme adopts two different turbulence models within ocean boundary layer and ocean interior, and these two models are coupled through continuity of turbulence diffusivities and their derivatives at the base of the boundary layer (Large et al. 1997). The vertical viscosity is a factor of 10 (the Prandtl number) larger than diffusivity. Within the ocean boundary layer, the turbulence diffusivities are parameterized by cubic functions with coefficients determined by surface wind stress, buoyancy flux, and boundary conditions at the base of the boundary layer (Large et al. 1997). Below the surface boundary layer, the vertical fluxes follow the downgradient transport hypothesis, with turbulence diffusivities being expressed as the superposition of the contributions from shear-driven mixing, internal waves breaking, double diffusion, and molecular diffusion (Large et al. 1997).

The basic model configuration for the POP model is borrowed from a low resolution version of CCSM3 (Community Climate System Model) model (Yeager et al. 2006), with horizontal 100 (zonal) \times 116 (meridional) grid points (meridionally about 0.6° in the near equatorial region) and 25 vertical levels. The vertical resolution is about 10 m at the upper 100 m. We also embedded a solar absorption component based on specified monthly mean surface chlorophyll concentration (Ohlmann 2003) that is also borrowed from CCSM3.

2.2.2 The ECHAM atmospheric model

The prognostic variables in the ECHAM model include vorticity, divergence, temperature, surface pressure, water vapor, and cloud water. The surface fluxes of momentum, heat, water vapor and cloud water are calculated based on the Monin-Obukhov similarity theory. The vertical diffusion in the model is computed with a high order closure scheme depending on the turbulent kinetic energy. The parameterization of convection is based on the mass flux concept, in which cumulus clouds are represented by a bulk model including the effects of entrainment and detrainment on both convective updraft and downdraft mass fluxes (Tiedtke1989). The organized entrainment and detrainment are related to in-cloud buoyancy, and an adjusted-type closure is used, which is based on the convective available potential energy (CAPE) with the large-scale moisture convergence as a trigger (Nordeng 1995). We used the T42 resolution corresponding to a horizontal resolution about 2.8° . The model has 19 vertical layers extending from the surface to 10 hPa.

2.2.3 Coupling strategies

The coupler OASIS (v3.0), developed at the European Centre for Research and Advanced Training in Scientific Computation (CERFACS), France, is used to exchange variables from the atmospheric and oceanic components (Valcke et al. 2003). Heat flux conservation interpolation is adopted to keep the energy conservation, thereby avoiding the climate drift in the coupled system. Atmosphere and ocean exchange information once a day. The atmosphere model provides daily mean surface wind stress, heat and freshwater fluxes to the ocean model. The latter sends daily mean SST and ocean surface currents (without daily cycle) back to the former. Ocean surface currents are used to

calculate the surface wind stress according to the relative velocity, which could, to a certain degree, eliminate the cold SST bias in the equatorial Pacific (Luo et al. 2005). Currently, the fully coupled region is confined between 60°S to 60°N. Beyond this region, the underlying SST and sea surface ice are specified as the climatological monthly mean derived from the 16-yr (1979-94) dataset, which were used as the boundary conditions in the Atmospheric Model Intercomparison Project (AMIP) II experiments (Taylor et al. 2000). At this stage, POEM is a partially coupled model.

2.3 Data and Experiments

In this section, we use several monthly datasets. Monthly-mean SST (1958-2009) from NOAA Extended Reconstructed SST (ERSST, v3b) (Smith et al. 2008), monthly-mean precipitation (1979-2009) from GPCP datasets (Adler et al. 2003), surface wind stress (1958-2001) from European Center for Medium-Range Weather Forecasts (ECMWF) Re-Analysis (ERA-40) data (Uppala et al 2005), and ocean surface heat fluxes (1984-2007) from objectively analyzed air-sea fluxes (OAFlux) (Yu and Weller 2007).

Besides the fully coupled run (CTRL, 100 years after 300 years spinup), we conducted two sensitivity experiments to detect the possible causes that lead to the excessive cold tongue extension (Table 2.1). One is an ocean forced run with observed wind stress (ERA-40) and heat flux OAFlux (OCN_obs, 20 years). The other adopts the daily wind stress forcing from CTRL but with observational heat flux (OCN, 50 years). The shortwave radiation (SWR) and longwave radiation are from the International Satellite Cloud Climatology Project Flux Data (ISCCP-FD) (Zhang et al 2004), and climatological precipitation is from GPCP (Adler et al. 2003). Surface winds, air

temperature and specific humidity from the National Centers for Environmental Prediction (NCEP) in combination with ocean model SST are used to calculate surface latent and sensible heat fluxes. Meanwhile, an AMIP experiment with observational SST from 1979 to 1999 was also carried out.

2.4 Annual Mean SST and Precipitation

Figure 2.2 compares the annual mean SST and precipitation over the tropics and extra-tropics obtained from the observations and the CTRL. In most of the ocean basins, SST is simulated reasonably well with realistic spatial patterns. However, a severe warm bias in excess of 1.5 °C appears off the western coasts of the America and Africa, which is likely linked to errors in simulating stratus clouds (e.g. Ma et al. 1996) and the marine boundary air-sea feedbacks. A considerable cold SST bias is found in the equatorial Pacific (Fig. 2.2c), which was suggested to be caused collectively by excessive Bjerknes feedback (Bjerknes 1969), overestimated SST-Latent heat flux (LHF) feedback and insufficient SST-SWR feedback (Lin 2007). Meanwhile, insufficient precipitation occurs over the equatorial western Pacific (WP) and the northern ITCZ regions, and excessive precipitation presents over the south of equatorial regions (so-called, the double ITCZ problem). Of particular note is that the largest underprediction (>3 mm/day) is seen in the WP (Fig. 2.2f), which may act as a critical factor affecting ENSO simulation by altering air-sea feedbacks in the tropical Pacific.

2.5 Summer monsoon

Monsoon simulations and forecasts remain one of the most challenging issues in current coupled models. For the current CGCMs participated in the World Climate Research Program/Coupled Model Inter-comparison Project 3 (CMIP3), only 6 out of 18 models were found to have relatively realistic monsoon climatology (Annamalai et al. 2007). Here we only focus on the summer monsoon (Jun-Aug, JJA) as shown in Fig. 2.3. Three monsoon centers are observed, the Indian summer monsoon, the Eastern Equatorial IO, and the WNP monsoon. AMIP simulation fails to capture the large precipitation centers over the Indian summer monsoon and WNP monsoon regions, but suffers heavier loading in the eastern Equatorial IO (not shown). Coupled model POEM is able to capture the observed intensity and spatial pattern reasonably well, despite of the insufficient precipitation over the WNP (Fig. 2.3b). It indicates the importance of air-sea interaction in simulating the summer monsoon (Fu et al. 2002; Wang et al. 2005; Kim et al. 2008). During boreal summer season, a high spatial correlation (about 0.77) with GPCP observations, can be obtained for the region 40°E-160°E, 20°S-40°N. Therefore, it also belongs to the group with better monsoon simulations in current state-in-art coupled models (Sperber and Annamalai 2008).

We further present, in Fig. 2.4, the first 3 leading EOF modes of boreal summer (JJA) precipitation in the domain 40°E-160°E, 20°S-40°N from observations. These three modes capture about 21.7%, 9.5% and 8.5% of the total variance, respectively. The first mode (EOF-1) is characterized by suppressed precipitation over the equatorial western Pacific which extends northwestward to the Bay of Bengal, and enhanced precipitation over the Maritime continent and IO (Fig. 2.4a). The major loading in EOF-2 is trapped over the western Pacific which shows a southwest-northeast orientated structure. These

first two leading EOF modes have been demonstrated to be able to well capture the WNP subtropical high, associated with the La Nina development and local thermodynamic feedback (Wang and Xiang, submitted). The first two principle modes are referred to as the La Nina developing mode and anticyclone-dipole SST mode (Wang and Xiang, submitted). The EOF-3 mode acts as a typical IO dipole (IOD) mode with suppressed convection over the southeast tropical IO and enhanced convection over the western IO, together with a strong suppressed convection over the WNP (Fig. 2.4c).

Interestingly, our coupled mode is also able to well capture these three observed precipitation modes despite of some displacement of the convection center (Fig. 2.5). This provides a prerequisite for the seasonal forecast of the boreal summer monsoon system.

2.6 MJO Simulation

Lin et al. (2006) investigated current CGCMs, and found that the majority of them have difficulty in realistically representing the basic characteristics of MJO (or Intraseasonal Oscillation), with respect to its intensity, propagation, spatial pattern. Our coupled model shows some capacity in simulating MJO. Here we will very briefly introduce its performance in simulating the MJO both in boreal winter (May-October) and boreal summer (November-April) by adopting a 20-100-day bandpass-filtering of the daily anomalies. Figure 2.6 displays the percentage variance of zonal wind at 850 hPa (U850) accounted by ISO. It is clear that POEM reasonably captures the major loading with relatively strong ISO signals, measured by the percent variance accounted for by the

20-100-day band relative to variance filtered with a wider bandwidth. The intraseasonal variance of U850 tends to be constrained in the summer hemisphere.

We also performed the EOF analysis of the bandpass filtered 850 hPa zonal wind during boreal winter (Fig. 2.7) and boreal summer (Fig. 2.8). During boreal summer, the first mode (EOF-1) is characterized by enhanced convection over the Indian Ocean and suppressed convection over the western Pacific. EOF-2 mode shows the eastward propagation of the anomalous convection to the maritime continent. POEM reasonably simulates the first 4 leading EOF modes but EOF-3 is corresponding to EOF-4 in observations and EOF-4 represents the EOF-3 in observations.

Wavenumber-frequency spectra analyses for equatorial precipitation and U850 are also examined in Fig. 2.9. Observations show that U850 shows a clear peak period of 30-90-day with zonal wavenumber 1, and zonal wavenumbers 1-3 for precipitation. The eastward power is dominating (4 times larger) over the westward component. In general, coupled model POEM obtains a reasonable results compared with observations although the component of the eastward propagation is stronger in boreal summer but slightly weaker during boreal summer (Fig. 2.9).

2.7 Possible causes of excessive cold tongue extension

Many different aspects can contribute to the excessive cold tongue extension problem. In brief, deficiencies in individual model component and air-sea feedbacks are suggested to be responsible for this. From the oceanic point of view, cold SST bias in the equatorial Pacific could be a consequence of deficiency in ocean dynamics, surface heat flux and

dynamic wind stress biases. Indeed, these factors cannot be exactly separated, while we can find some clues by comparing several experiments.

First, we regard the difference between the OCN_obs and observational SST is due to the ocean dynamics deficiencies since OCN_obs uses the observed heat flux and surface wind stress forcing. It is interesting that significant cold SST bias is found over the equatorial CP with its maximum ($-1.5\text{ }^{\circ}\text{C}$) locating near 120°W (Fig. 2.10b). This maximum SST cooling collocates with the strongest mean upwelling over the equatorial Pacific (Fig. 3.6). As a result, we suggest that this could be related to too strong upwelling and/or vertical mixing. The experimental difference between CTRL and OCN is due to heat flux bias in the CTRL run since they share the same surface wind stress forcing. Notice that pronounced cold SST bias appears over the CP and WP with its maximum ($-1.5\text{ }^{\circ}\text{C}$) slightly to the east of the international dateline (Fig. 2.10c).

The question arises, however, which component among the heat flux contributes to this cold SST bias as shown in Fig. 2.10c. To address this question, we plotted the equatorial heat flux averaged over 5°S - 5°N (Fig. 2.11) from observations, AMIP, and CTRL. It is clear that, in the AMIP run, the SWR is underestimated but the LHF is overestimated so that the net heat flux is grossly underestimated. The weakened net heat flux exhibits a relatively uniform structure in the zonal direction, while the resultant SST bias does displace westward. It implies that mean circulation and air-sea feedback tend to shift the most prominent cold SST bias westward.

Strikingly, the CTRL run attains similar net heat flux with observations which is primarily due to the reduced LHF (Fig. 2.11), longwave and sensible heat flux (not shown). Similar magnitude of SWR is obtained in the CTRL and AMIP runs. It gives an

indication that air-sea coupling acts to reduce the cold SST bias through SST-LHF feedback and SST-upwelling feedback.

Now, let us focus on the dynamic effect from surface wind stress bias. As shown in Fig. 2.12, in comparison with observation, surface wind stress in the CTRL is slightly weaker over the region east of 160 °W but stronger over the region west of 160 °W. To detect the impacts from surface wind stress bias, we compare the SST difference between OCN and OCN_obs. These two experiments share the same surface heat flux from observations but with different surface wind stress forcings. In the far EP, wind stress bias (compared with observations) displays strong cross equatorial flow from northeasterly to northwesterly (Fig. 2.12). This wind stress can produce a dipole SST bias pattern with SST cooling over the north of the equator but SST warming over the south of the equator. Considerable easterly bias is evident over the WP but it can only generate a moderate SST cold bias (-0.5 °C). Therefore, we conclude the dynamic effect from surface wind stress bias tends to amplify the SST warming bias over the SEP but plays less important role in driving the excessive cold tongue extension in our coupled model—POEM. Nevertheless, caution should be made in that this conclusion may not be applicable for other coupled climate models. We notice in particular that large discrepancy of zonal surface wind stress is seen between the CTRL and the corresponding AMIP run (Fig. 2.11). In comparison with the AMIP run, the CTRL produces significantly underestimated (overestimated) easterly wind over the region east (west) of dateline. In other words, in comparison with observations, the relatively ‘reasonable’ surface zonal wind stress from the CTRL acts as a result of air-sea feedback.

It is caused by the reduced zonal SST gradient as shown in Fig. 2.2c. We will discuss this in detail in the next chapter.

2.8 Summary and Discussion

We have developed a coupled model—POEM, by coupling POP (v2.0) ocean model and ECHAM (v4.6) atmospheric model with the aid of the coupler OASIS (v3.0). It is coupled in the region between 60°S and 60°N and climatological SST and sea ice are implanted beyond these latitudes. The main purpose to develop this coupled model is to study the dynamics and interactions of ENSO, monsoon and MJO. Results show that this model can well capture several maximum monsoon center during boreal summer. The first 3 leading EOF modes of precipitation (La Nina developing mode, Anticyclone-dipole SST coupled mode and IOD mode) are also reproduced in the fully coupled run during boreal summer. Reasonable MJO simulations are also obtained with respect to its intensity and propagation features.

This model suffers a serious double ITCZ problem. The counterpart of the double ITCZ problem in SST is characterized by a dipole bias pattern with excessive cold tongue extension and warm SST bias over the SEP. We argue that the main problems contributing this excessive cold tongue extension are from two different aspects. One is caused by deficiencies in ocean dynamics possibly related to upwelling and turbulent mixing. The other is tightly linked to the atmospheric model with less SWR but more LHF over the equatorial Pacific. One possible cause of the underestimated SWR is that parameterized cumulus precipitation is excessively sensitive to low-level moisture convergence so that deep convection is easy to form. The overestimated LHF is likely

caused by less moisture in the near-surface atmosphere. It provides two different directions to further improve this coupled model performance.

Table 2.1 List of experiments designed in this chapter

<i>Experiments</i>	Descriptions
CTRL	Fully coupled run with 100 years after 300 years spinup
OCN	Climatological daily wind stress forcing is from CTRL, and SWR and longwave radiative fluxes are from the International Satellite Cloud Climatology Project Flux Data (ISCCP-FD) (Zhang et al. 2004), and climatological precipitation from the GPCP. Surface winds, air temperature and specific humidity from the National Centers for Environmental Prediction (NCEP) in combination with ocean model SST are used to calculate surface latent and sensible heat fluxes.
OCN_obs	Forced with observational wind stress (ERA-40) and heat flux as same as the OCN run.
AMIP	Atmospheric forced run with observed SST from 1979-1999.

Chapter 3

Reduction of the Thermocline Feedback associated with the Mean SST Bias in ENSO Simulation

3.1 Introduction

The simulation of El Niño/Southern Oscillation (ENSO) in the coupled General Circulation Models (CGCMs) has achieved steady progresses in recent decades (Mechoso et al. 1995; Latif et al. 2001; AchutaRao and Sperber 2002; Meehl et al. 2005; Randall et al. 2007). However, the physical processes related to ENSO are unrealistically simulated in various degrees. For example, the majority of current coupled model achieve weak thermocline feedback and zonal advection feedback together with weak thermal damping effect (Kim and Jin 2010). From this point of view, although some current CGCMs achieve comparable ENSO amplitude with observations (Guilyardi et al. 2009b), it does not guarantee the realistic representation of the model physics in governing ENSO behaviors. More importantly, it would largely influence the fidelity how ENSO property will change under external anthropogenic forcing.

Understanding and improving ENSO simulation are of particular importance and highly desirable for a number of reasons. Firstly, the reality of ENSO representation seriously affects the skill and confidence of climate predictability from synoptic to interannual time scales (e.g. Vitart et al. 2003; Guldberg et al. 2005). Secondly, the diverse (or even opposite) results on the projected changes of ENSO properties in response to anthropogenic forcing (Merryfield 2006; Guilyardi 2006; Philip and van

Oldenborgh 2006; Latif and Keenlyside 2009; Kim and Jin 2010) are more often attributable to the notorious deficiencies in representing ENSO under the present-day climate. Thirdly, realistic ENSO simulation largely determines the capability and fidelity of a model in reproducing the most prominent tropical and tropical-extratropical teleconnections (e.g. Joseph and Nigam 2006).

Diagnosing the possible sources of systematic biases is an essential step to understand and alleviate these biases in ENSO simulation. Usually, systematic biases in a coupled system can be traced back to shortcomings of individual model components. For example, the convection scheme in an atmospheric model has been known to have profound influences on ENSO simulation in a coupled system (Kim et al. 2008; Neale et al. 2008; Guilyardi et al. 2009a). From the oceanic point of view, Meehl et al. (2001) highlighted the importance of vertical diffusivity and claimed that weaker vertical diffusivity is able to produce stronger ENSO amplitude due to the resultant sharp thermocline gradients. Another essential process is the atmosphere-ocean feedback that may exacerbate any model's intrinsic biases and further cause a mean-state drift away from the observed climate, which, in turn, will also affect ENSO simulation.

The strong interactions between annual mean state and ENSO have been extensively investigated in previous studies in both observations and numerical models (e.g. Li and Hogan 1999; Fedorov and Philander 2000; Wang and An 2001; An et al. 2010). By the same token, the mean state biases in a coupled system could undermine the quality of ENSO simulation (Wittenberg et al. 2006; Large and Danabasoglu 2006; Spencer et al. 2007; Manganello and Huang 2009). Spencer et al. (2007) suggested that ENSO amplitude is very sensitive to not only the imposed heat flux corrections but also its

meridional extent (i.e. tropical versus equatorial regions). Manganello and Huang (2009) pointed out that the warm SST bias in the Southeast Pacific (SEP) tends to induce a stronger ENSO amplitude. Kim and Jin (2010) investigated the ENSO simulated by the CGCMs from IPCC AR4 and concluded that the majority of current CGCMs underestimate the thermocline feedback, but the causes are not clear. In this study, we mainly focus on exploring the possible factors leading to the weakened thermocline feedback in a coupled system.

As the dominant factor controlling the development of ENSO events, weakened thermocline feedback will reduce the simulated ENSO amplitude. Meanwhile, it may also alter the periodicity of ENSO. Previous studies have shown that the time scale of ENSO is primarily determined by the relative contribution from the thermocline feedback and the zonal advection feedback (An and Jin 2001; Fedorov and Philander 2000), so that a weaker thermocline feedback is conducive to a relatively shorter ENSO cycle, and vice versa. Therefore, investigating the cause of the weak thermocline feedback is of particular importance to improve the ENSO simulation. However, to the best of our knowledge, this has not been systematically addressed in the literature. In this study, we aim to investigate how the mean SST bias influences the thermocline feedback. The finding of this study is expected to guide the improvement of atmosphere-ocean models in terms of better ENSO simulation, and may also provide important clues applicable to the study of ENSO property changes in a future warmer climate.

For convenience, we divided the equatorial Pacific into three regions, the WP (west of 180 °), equatorial central Pacific (CP, 180 °-120 °W), and equatorial eastern Pacific (EP, east of 120 °W).

This paper is organized as follows. Section 3.2 introduce the model, experiments and validation datasets used in this study. The simulated ENSO properties are described in section 3.3. We further discuss the air-sea coupling strength in Section 3.4. The wind-thermocline coupling and thermocline-subsurface temperature coupling are discussed in section 3.5. Section 3.6 investigates the impacts of mean state biases on the equatorial mean upwelling. Section 3.7 summaries our major findings and discusses remained issues.

3.2 Model, Experiments and Validation data

3.2.1 Model, Experiments

The coupled model we used here is the POEM model which was introduced in Chapter 2. Several experiments are conducted in this study. The first is a fully coupled run for 100 years after 300 years spinup. Hereinafter we refer to this experiment as the control run (CTRL). In addition, two sensitivity experiments are carried out to demonstrate the potential impact of mean SST bias on ENSO simulation: the annual-mean SST correction (AMSC) run and the ocean-forced (OCN) run (Table 3.1). For the AMSC, we use a flux adjustment to ‘correct’ the annual mean SST field. Briefly, we first carry out a 30-year coupled integration with a strong SST restoring force (a restoring timescale of 5 day) towards the observed climatology, from which the corresponding Newtonian damping term can be estimated and extracted. We, then, average this long-term damping (Fig. 3.1a) and add it to the SST equation in the coupled AMSC run. Similar to CTRL, we integrate the AMSC for 100 years.

A 50 years ocean forced run with daily wind stress forcing from the CTRL experiment, and shortwave radiation (SWR) and longwave radiation from the

International Satellite Cloud Climatology Project Flux Data (ISCCP-FD) (Zhang et al 2004), and climatological precipitation from the Global Precipitation Climatology Project (GPCP). Surface winds, air temperature and specific humidity from the National Centers for Environmental Prediction (NCEP) in combination with ocean model SST are used to calculate surface latent and sensible heat fluxes.

3.2.2 Validation datasets

Several datasets have been used to validate model simulations: Monthly-mean SST (1958-2009) from NOAA Extended Reconstructed SST (ERSST, v3b) (Smith et al. 2008), monthly-mean precipitation (1979-2009) from GPCP datasets (Adler et al. 2003), surface wind stress (1958-2001) from European Center for Medium-Range Weather Forecasts (ECMWF) Re-Analysis (ERA-40) data (Uppala et al 2005), and ocean surface heat fluxes (1984-2007) from objectively analyzed air-sea fluxes (OAFlux) (Yu and Weller 2007). A reanalysis of ocean climate using Simple Ocean Data Assimilation (SODA, v2.0.2) is also used (Carton et al. 2005), which is forced by ECMWF surface wind stress from 1958 to 2001. We also used the Climate of the Twentieth Century (20C3M) simulation from 12 CGCMs from IPCC AR4 (<http://www.ipcc-data.org/ar4/scenario-20C3M.html>), along with their corresponding available AMIP runs (1980-1999). Table 3.2 lists all these models along with their brief descriptions.

3.3 ENSO simulations

As is well known, the growth of ENSO is ascribable to several positive ocean-atmosphere feedbacks that encompass interactions of atmospheric convection, ocean

dynamics and the equatorial surface winds (e.g. Jin et al. 2006; Guilyardi et al. 2009b; An et al. 2010). Among them, the most dominant contribution comes from the thermocline feedback, which carries subsurface variability to surface through mean upwelling. The thermocline feedback can be expressed as $-\overline{W} \frac{DT_e}{Dz} \propto R(u,T)R(Z20,u)R(Te,Z20)\overline{W}$, where \overline{W} represents the equatorial mean upwelling and T_e denotes the subsurface temperature anomaly (Liu et al. 2011). From this, the intensity of thermocline feedback can be found to be related to four different factors, a) the air-sea coupling strength ($R(u, T)$) that measures surface wind stress (u) response to SST anomaly (SSTA, T), b) wind-thermocline coupling ($R(Z20, u)$) where the 20 °C isothermal line ($Z20$) is used as a proxy of the thermocline depth, c) thermocline-subsurface temperature coupling ($R(Te, Z20)$), and d) mean upwelling (\overline{W}).

With an annual-mean Newtonian damping (Fig. 3.1a), the AMSC corrects, to a great degree, the SST bias inherent in the coupled system (Fig. 3.1b). The double ITCZ problem is also largely eliminated compared with the CTRL (Fig. 3.1c versus Fig. 2.2f). In this study, we consider the AMSC to be a best realization although some other fields, such as surface wind stress and precipitation still show non-trivial biases. Figure 3.2 displays the standard deviation of SSTA from observations, the CTRL and AMSC. In comparison to AMSC, the overall ENSO amplitude in the CTRL does not change much but with a reduced (enhanced) variation over the CP (WP and far EP) (Fig. 3.2d). Nevertheless, the thermocline feedback in the CTRL is substantially underestimated to be only about 27% of that in the AMSC (Table 3.3). The weakened thermocline feedback is attributed to the underestimation of air-sea coupling strength (42%), wind-thermocline coupling (16%), thermocline-subsurface temperature coupling (25%) and mean

upwelling (27%) (Table 3.3). We will discuss these four factors in the following several sections.

3.4 Air-sea coupling strength

Surface zonal wind anomaly acts as an integral component of the Bjerknes feedback that couples the atmospheric anomalous convection and ocean subsurface variability, so that air-sea coupling strength $R(u, T)$ largely determines the intensity of the thermocline feedback. Kim and Jin (2010) found that the majority of current CGCMs underestimate the air-sea coupling strength in comparison to observations. Further, Liou et al. (2010) concluded that air-sea coupling strength is usually weaker in coupled runs than in the corresponding AMIP runs. However, the physical explanation is unclear. Here we demonstrate that the weakened air-sea coupling strength is closely linked to the mean SST bias.

We present, in Fig. 3.3, the spatial pattern of precipitation and zonal wind stress anomalies that were regressed onto the Niño-3 index from the observations, the CTRL and AMSC. Observational results illustrate that a maximum anomalous precipitation is located near the international dateline, with large portion of precipitation anomaly expanding to the ITCZ region (Fig. 3.3a). It also indicates that ENSO is strongly convectively coupled with prominent precipitation and surface wind stress anomalies. In the AMSC, ENSO-related maximum precipitation is stronger than that in observations but largely absent in the equatorial EP, so that the resultant zonal wind stress displaces westward (Fig. 3.3c and 3.3a). This is possibly due to the fact that the AMSC still has about 0.5 °C cold bias in the EP (Fig. 3.1b).

However, in the CTRL, ENSO-related precipitation anomaly resembles a horseshoe-like pattern, with two parallel bands of intense precipitation straddling the equator across the equatorial Pacific (Fig. 3.3b). Note that the CTRL also fails to capture the maximum precipitation anomaly near the international dateline but with a maximum center migrating far west. Therefore, when the anomalous convection moves eastward during El Niño events, it tends to move along the zones of warmest SST at 5°S and 5°N, avoiding the cold equatorial region. This bias has direct impacts on the air-sea coupled system with a combination of two effects. First, the suppressed precipitation anomaly, to a great extent, decouples the atmosphere and ocean through reducing the convection-low level wind feedback. Second, the westward displacement of the anomalous convection acts to reduce surface westerly anomaly over the CP. Consequently, surface zonal wind stress anomaly exhibits a zonally elongated but significantly weakened amplitude (Fig. 3.3b).

Since the maximum zonal wind stress anomaly appears in the CP, we propose to use the zonal wind stress anomaly in the CP, rather than that over the Niño-4 region as Guilyardi et al. (2009a) did, to quantitatively measure the intensity of the air-sea coupling strength. According to this definition, the CTRL produces a much weaker coupling strength than that derived from the AMSC and ERA-40 (Table 3.3). The air-sea coupling strength is reduced about 42% in the CTRL in comparison to the AMSC. It further confirms that the errors of coupling strength indeed arise, or at least partly, from the mean SST bias.

To distinguish the convection-induced surface wind anomaly, we use a dry AGCM model which is built based on a dry version of Princeton AGCM with five sigma levels (Jiang and Li 2005; Li 2006; Xiang et al. 2011). This dry AGCM is forced by prescribed

heating. It is clear that low-level wind response exhibits distinct patterns with different prescribed mid-tropospheric heating (Fig. 3.3d-f). For the case with the heating similar to the regressed precipitation pattern from the CTRL, the dry AGCM produces much weaker low level wind anomalies than those from the AMSC and observations. Both from the fully coupled and dry AGCM simulation, one important feature is that the zonal wind stress anomaly related to the precipitation from the CTRL exhibits weak meridional gradient. In the near-equatorial region, the horizontal pressure gradient is weak so that the SST gradient-induced zonal wind is suggested to have weak meridional gradient. However, the observational zonal wind anomaly in the CP mainly represent the Rossby wave component with the precipitation heating, which actually decays rapidly in the meridional direction. Further, in the CTRL, the maximum zonal wind anomaly is residing to the east of the maximum convection (Fig. 3.3b). Considering the fact that the surface wind stress is nonlinearly related to surface wind (McGregor et al., submitted), we then compared the mean surface (1000 hPa) wind speed between two experiments (Fig. 3.4b). It is clear that the surface wind speed is significantly weakened in the CP but stronger in the WP. As such, the nonlinearity tends to induce intensified (reduced) wind stress response in the WP (CP), however, it is opposite in the CTRL run (Fig. 3.3b). Thus the zonal wind anomaly in the CTRL mainly arises from the zonal SST gradient instead of convective anomaly.

3.5 Wind-thermocline coupling and thermocline-subsurface temperature coupling

We now focus on another important issue of the thermocline feedback, namely, how the thermocline responds to the surface wind stress forcing and how the subsurface temperature varies with respect to the thermocline depth changes. As is well known, equatorial zonal wind stress forcing can excite eastward propagating Kelvin waves and westward propagating Rossby waves, prompting to form an east-west thermocline contrast pattern. The linear regression of thermocline anomaly regressed onto the CP zonal wind stress anomaly is calculated to estimate the strength of the wind-thermocline coupling $R(Z20, u)$.

We present, in Fig. 3.5a, b, the thermocline change regressed onto the equatorial zonal wind anomaly averaged over 160°E-130°W, 5°S-5°N. Based on the spatial distribution, the wind-thermocline coupling $R(Z20, u)$ is defined as the regressed thermocline depth averaged over 180°E-80°W, 2°S-2°N. Both the AMSC and CTRL obtain weaker wind-thermocline coupling than observations, while the wind-thermocline coupling in the CTRL is weaker about 16% than the AMSC (Table 3.3). The question arises, however, what causes this weakened wind-thermocline coupling in the CTRL? We argue that this is tightly related to the equatorial zonal wind stress pattern (Fig. 3.5c, d). As mentioned in section 4, the convection-induced westerly anomaly displays strong meridional gradient structure as part of Rossby wave response, however, zonal wind stress in response to zonal SST gradient may have weak meridional gradient. The regressed equatorial (1°S-1°N) zonal wind anomaly averaged over 160°E-130°W is larger in the AMSC than that from the CTRL (1.51 versus 1.38) although the most intense center from the AMSC shifts to the south of the equator (Fig. 3.5c, d). Hence, the

AMSC attains stronger wind-thermocline coupling since equatorial zonal wind is more effective to drive equatorial waves than that of the off-equatorial winds.

The wind-induced thermocline depth changes can alter subsurface temperature. We plot the linear regression of equatorial temperature anomaly onto the Z20 anomaly averaged over 180 °80 °W, 2 °S-2 °N (shading in Fig. 3.6). It can be seen that the CTRL bears close resemblance to the AMSC in representing the maximum temperature changes at the center of the thermocline with strongest mean vertical temperature gradient. Yet, it is significantly weaker at the bottom of the mixed layer depth (60 m) from the CTRL (shading in Fig. 3.6c). The thermocline-subsurface temperature coupling, $R(T_e, Z20)$, is quantitatively measured by the regressed subsurface temperature averaged over 180 °80 °W, 2 °S-2 °N (Table 3.3). Results show that $R(T_e, Z20)$ in the CTRL is weaker about 25% than that in the AMSC. This is attributed to the cold SST bias which induces an underestimation of mean upper-ocean stratification at the bottom of mixed layer (contours in Fig. 3.6c).

3.6 Equatorial mean upwelling

3.6.1 Dynamics determining the equatorial upwelling

Mean equatorial upwelling holds key for ENSO growth, however, it is relatively difficult to measure it directly due to its small magnitude. The equatorial upwelling is usually estimated by calculating the transports of the meridional overturning cell (Johnson et al. 2001; Meinen et al. 2001; Cronin and Kessler 2009) or horizontal divergence.

In the regions away about one Rossby radius ($\sim 2.2^\circ$ latitude) from the equator, the geostrophic and Ekman components are expected to account for the lowest-order dynamics of the near-surface velocity (Lagerloef et al. 1999). In the equatorial Pacific, the meridional geostrophic currents typically show a convergence effect occurring in the upper 200 m, whereas the Ekman currents tend to have a divergence effect within a much shallower depth (Meinen et al. 2001). However, only about half of the Ekman divergence can be counterbalanced by the meridional geostrophic convergence in the upper 50 m. Based on mass conservation, this combination effect from the Ekman divergence and geostrophic convergence necessitates vertical motion with its maximum at the depth around 50 m (Meinen et al. 2001; Johnson et al. 2001).

The divergent Ekman flow, balanced with the Coriolis force and vertical gradient of horizontal viscous force, is by far the largest component contributing to the equatorial upwelling. The meridional Ekman current can be estimated by:

$$-fv_{ek} = \frac{1}{\rho_o} \frac{\partial \tau_x}{\partial z} \quad (1)$$

where f is the vertical component of the Coriolis parameter, v_{ek} is the meridional Ekman velocity, and ρ_o is the background density. The zonal viscous stress τ_x can be related to the shear profile through the turbulent viscosity parameter A_v ,

$$\tau_x(z) = \rho_o A_v \frac{\partial u(z)}{\partial z} \quad (2)$$

Taking (2) into (1) yields,

$$-fv_{ek} = A_v \frac{\partial^2 u}{\partial z^2} \quad (3)$$

The boundary condition can be provided with the balance of the shear stress and surface wind stress τ_o ,

$$\tau_{xo} = \rho_o A_v \frac{\partial u}{\partial z} \quad \text{at } z=0; \quad (4)$$

$$\tau_{-H} = 0 \quad \text{at } z=-H; \quad (5)$$

Integrating (1) from the surface to the bottom of the Ekman layer ($-H$) shows that the Ekman transport is to advect waters exactly to the right of the wind stress in the northern hemisphere, to the left in the southern. Although the Ekman transport is only related to the surface wind stress and the Coriolis parameter, the upper ocean Ekman current, especially in the upper 30 m where the poleward divergence is largest (Johnson et al. 2001; Cronin and Kessler 2009), highly depends on the vertical turbulent mixing and the vertical distribution of the zonal currents. Thus, the impacts of mean state biases on the mean upwelling are investigated separately by examining the effects of surface wind stress forcing and interior ocean turbulent mixing.

3.6.2 Dynamic impacts associated with surface wind stress forcing

Figure 3.7 displays the longitude-depth diagram of the vertical velocity along the equatorial Pacific from the CTRL and AMSC. For the AMSC, the maximum upwelling is located in the CP around 140 °W at the depth of about 60 m (Fig. 3.7b), with a magnitude of about 1.6 m/day. Compared with AMSC, the CTRL features a substantially weaker upwelling in the CP but slightly stronger upwelling over the WP. The maximum reduction in the CTRL is found at the depth of about 60 m, collocated with AMSC's maximum mean upwelling.

Since the equatorial upwelling velocity is, to the first order approximation, proportional to the intensity of the equatorial easterly wind stress, we examined the surface wind stress difference between these two experiments. Figure 3.8a shows that the AMSC run has an enhanced (reduced) easterly wind stress in the equatorial CP (WP), which is dynamically consistent with the mean upwelling difference shown in Fig. 3.7c.

Then, what causes the wind stress difference? Physically, surface wind stress is driven by two different ways, namely convection and lower boundary SST gradient (Lindzen and Nigam 1987). In order to identify the responsible mechanisms, we analyzed the mean state differences in sea level pressure (SLP), precipitation and 850 hPa wind between the CTRL and the AMSC (Fig. 3.8b, c). Note that in the tropical region, the 850 hPa (above the atmospheric boundary layer) wind can be approximately regarded as convectively driven. The surface wind stress and 850 hPa wind difference both show enhanced trades in the equatorial WP, coherent with the underestimated precipitation there. By contrast, large discrepancy appears in the equatorial CP between 850 hPa wind and surface wind stress. At 850 hPa, strong northerly wind is seen in the CP, which is suggestively driven by the excessive precipitation over the south of the equator (Fig. 3.8c). This is different from surface wind stress difference that shows a large westerly component (Fig. 3.8b).

This implies that the westerly wind stress difference in the CP (Fig. 3.8b) is not convectively driven associated with the double ITCZ problem. Actually, it mainly represents a divergent wind component that agrees well with the zonal gradients of SLP difference (Fig. 3.8b). A SLP dipole pattern is apparent with its maximum in the equatorial Pacific around 180°E and minimum in the SEP (Fig. 3.8b), driving a

northwesterly wind with strong westerly component. As such, we argue that this CP wind stress difference primarily originates from the reduced SST zonal gradients (Lindzen and Nigam 1987) (Fig. 2.1c).

The above arguments highlight the importance of dynamic effects of surface wind stress in determining the intensity of equatorial upwelling. In addition, the thermodynamic effect may also affect the mean upwelling by altering the upper ocean momentum viscosity as well as the Ekman divergence. However, the above comparison between CTRL and AMSC cannot separate these two different processes. In fact, given the same surface wind stress forcing, the equatorial mean upwelling could be different due to the convection-induced mixing in the upper ocean, which is addressed in the next section.

3.6.3 Thermodynamic impacts associated with upper-ocean convective mixing

As discussed in section 6.1, meridional Ekman divergence plays a dominant role in driving the equatorial upwelling so as to maintain the cold SST in the equatorial EP. Meanwhile, the Ekman currents are tightly linked to the turbulent vertical diffusion, which plays a very important role in realistically representing the SST, vertical mixed-layer structure, and upper ocean currents (Blanke and Delecluse 1993). Schneider and Muller (1994) found that both the meridional and vertical velocity in the near-surface are very sensitive to the intensity of mixing, and particularly increasing eddy yields reduced equatorial upwelling in the surface layer. To reveal the thermodynamic impacts associated with the excessive cold tongue extension on the equatorial mean upwelling, we compare the CTRL with the OCN. The latter is forced with observed monthly heat

and freshwater fluxes, but daily wind stress forcing from the output of the CTRL. Thus, the model difference between them must originate from heat and/or freshwater fluxes forcing. The purpose to use daily wind stress forcing for the OCN is to retain high frequency wind variability which may substantially influence the upper ocean vertical mixing.

Compared with the OCN, the CTRL also displays pronounced SST cooling between 160 °E and 120 °W with its maximum cooling of about -1.5 °C near 160 °W (Fig. 3.9a). Consistently, a deepened mixed layer is evident over the equatorial region (Fig. 3.9b). In terms of the mean upwelling, the CTRL exhibits a prominently underestimated upwelling in the region generally collocated with the region of pronounced SST cooling (Fig. 3.9c). One striking feature is that the reduced upwelling is located in a relatively shallower depth compared with the case mainly due to the dynamic wind stress forcing effect (Fig. 3.9c versus Fig. 3.7c).

Equatorial upwelling is mainly driven by the meridional Ekman divergence and the zonal current gradient plays less important role. The difference between CTRL and OCN also confirms that the weakened upwelling is primarily caused by the meridional currents difference rather than the zonal currents difference (Fig. 3.10). To understand the cause of this, we present the meridional currents averaged in the upper 30 m (Fig. 3.11a, b). Clearly, the CTRL experiment has much weaker meridional currents and features weaker meridional gradient in the region between 160 °E and 130 °W. Meanwhile, a baroclinic structure with near-surface divergence and subsurface convergence is evident in the vertical-meridional diagram of the mean meridional currents averaged over 160 °E-130 °W. The difference between the CTRL and OCN (contours in Fig. 3.11d) illustrates

an opposite structure to the mean pattern with near surface convergence and subsurface divergence indicating weaker divergence in CTRL (Fig. 3.11c). This meridional current difference readily accounts for the weaker upwelling in the CP in the CTRL.

Since these two experiments share the same daily wind stress forcing, the meridional currents difference should originate from thermodynamic effect related to the upper-ocean buoyancy. From the definition of Ekman currents (Eq. 3), vertical mixing acts as a necessary condition to produce Ekman currents as well as upwelling. However, cold SST bias could enhance the convective eddy-induced mixing and turbulent viscosity, which also reduces the vertical shear of currents because currents with strong vertical shear can only come out the region with stable stratification.

Results also show that sea surface height (SSH) patterns derived from these two experiments are very similar (not shown), indicating that the convergent geostrophic currents are almost identical. As a result, the meridional currents difference mentioned above should be attributed to Ekman currents. To help visualize a more complete picture, we plot the zonally (160°E-130°W) averaged mean viscous stress along 2.8°N and 2.8°S (Fig. 3.12). As expected, the zonal viscous stress is stronger in the upper ocean in the CTRL, except at sea surface where it is identical to surface wind stress. The maximum of the intensified viscous stress is residing at the depth of about 30 m (Fig. 3.12), leading to a reduced (increased) vertical shear of zonal viscous stress in the depth range above (below) 30 m. Based on the viscous stress, we further estimated the meridional Ekman currents, and the CTRL depicts weaker meridional Ekman currents at the depth above 30 m but stronger below this (Fig. 3.13), which is responsible for generating a weakened upwelling shown in Fig. 3.9c.

3.7 Summary and discussions

Although contemporary climate models have achieved substantial improvements in ENSO simulation (Latif et al. 2001; AchutaRao and Sperber 2002; Meehl et al. 2005; Randall et al. 2007), great challenges remain in many aspects. The thermocline feedback serves as the most dominant process for the development of ENSO, however, the majority of current CGCMs exhibit underestimated thermocline feedback (Kim and Jin 2010). Mean state biases inherent in the current CGCMs could be one alternative candidate for the underestimation of thermocline feedback. Thus, understanding the impact of the systematic biases on ENSO is instrumental for finding the causes of the deficiencies and improving ENSO simulation.

Associated with the double ITCZ problem, mean SST bias typically resembles a dipole pattern with excessive cold tongue extension in the equatorial CP and excessive warm SST in the SEP. This stays as a long standing and challenging issue inherent in many contemporary CGCMs. Based on a newly-developed coupled model—POEM, we reveal that this systematic SST bias can severely suppress the thermocline feedback, through reducing the air-sea coupling strength, wind-thermocline coupling, thermocline-subsurface temperature coupling and equatorial mean upwelling.

Firstly, the equatorial cold SST bias weakens and pushes the mean Walker circulation westward, which leads to a significant underestimation of convection-low level wind feedback as well as air-sea coupling strength. Secondly, with the suppression of anomalous deep convection over the CP, the equatorial surface zonal wind anomaly exhibits weak meridional gradient that is suggestively responsible for the underestimated

wind-thermocline coupling. Thirdly, equatorial cold SST bias leads to a weakened mean stratification, yielding a reduced thermocline-subsurface temperature feedback. Finally, both dynamic and thermodynamic effects from this SST bias contribute to the weakened mean equatorial upwelling. The dynamic effect arises from the weakened easterly wind stress in the CP because of the reduced east-west zonal SST gradient. Meanwhile, the equatorial cold SST bias considerably enhances the upper-ocean vertical mixing but reduces the vertical shear of meridional currents, resulting in a weakened upper ocean Ekman divergence and mean upwelling.

One intriguing feature is that although the thermocline feedback is largely underestimated, the simulated ENSO amplitude in the CTRL is comparable with that in the AMSC. We argued that the decrease of thermal damping effect largely compensates the effect of the reduced thermocline feedback. The SWR and LHF feedbacks are two dominant components for the thermal damping (Jin et al. 2006). Thermal damping can be measured by the heat flux anomaly (net, SWR, LHF) regressed onto SSTA (Fig. 3.14). Observational results show strong thermal damping on the equatorial region with SWR feedback dominating over LHF feedback in the region between 140 °E and 140 °W, and the opposite is true in the region east of 140 °W. Different CGCMs show large diversity particularly due to large uncertainty in SWR feedback (Lloyd et al. 2010; Kim and Jin 2010). Strikingly, the AMSC realistically captures both the SWR and LHF feedbacks, whereas these feedbacks are significantly underestimated in the CTRL. The weak SWR feedback in the CTRL can be a consequence of the weakened and westward migration of anomalous convection. The reduced LHF feedback is conceivable to be ascribed to the

reduced mean southeasterly trade wind speed (Fig. 3.4b) and lower specific humidity associated with cold SST bias.

How does the SST bias influence the ENSO amplitude may be model-dependent, as the ENSO amplitude also relies on some other processes, such as the zonal advection feedback, nonlinearity (e.g., An 2008) and noise level (e.g., Zavala-Garay et al. 2003; Jin et al. 2007). Nevertheless, those processes affecting the thermocline feedback proposed in this study are suggested to be applicable for other CGCMs. For example, we investigated 12 CGCMs from IPCC AR4 together with their corresponding AMIP runs (Table 3.2). The results show that most of them have cold SST bias in the CP and WP and warm bias in the SEP (Fig. 3.15), and the accompanying excessive (underestimated) easterly wind is evident in the far WP (CP) (Fig. 3.16). Therefore, the upwelling bias due to the dynamic surface wind stress is expected to be a common problem for current state-of-the-art CGCMs. The thermodynamic effect is also bound to influence the mean upwelling, particularly for those with serious cold SST bias in the equatorial Pacific. Similar to Lloyd et al. (2010), we also noticed that the air-sea coupling strength is weaker in the majority of the studied coupled model from IPCC AR4 than their corresponding AMIP simulations (Fig. 3.17).

Here it is also emphasized that the reduced thermocline feedback may shorten the simulated ENSO amplitude since the ENSO amplitude is largely controlled by the relative importance between thermocline feedback and zonal advection feedback (An and Jin 2001; Fedorov and Philander 2000). By comparing the power spectrum of Nino-3 SSTA in two experiments (Fig. 3.18), it is seen that AMSC obtains two power spectrum peaks, 2 years and 5 years, while the CTRL produces discrete 1-3 years peak. Further

analysis shows that the CTRL fails to capture the discharge-recharge mode (Jin 1997; Li 1997) from the EOF analysis of SSH anomaly, but the AMSC is able to capture both the tilt mode and discharge-recharge mode (not shown). The lead-lag correlation between the CP zonal wind stress curl and SSH anomaly indicates that the CP zonal wind stress in the AMSC is able to drive a shallowed thermocline with some months lag, however, it does not in the CTRL (Fig. 3.19, Fig. 3.20). Since the discharge-recharge theory can well explain the 3-5 period oscillation of ENSO. The failure to simulate the discharge mode in the CTRL provides an explanation of the shortened ENSO period than the AMSC.

Atmosphere-ocean mean state bias will result in serious problems in representing the ENSO simulation in CGCMs. Thus, a prerequisite to have reasonable and realistic ENSO simulation is to get a realistic annual-mean state. Considerable efforts have been made to alleviate the double ITCZ problem in current CGCMs, through modifications of atmospheric cumulus parameterizations (Kim et al. 2008; Song and Zhang 2009), upper ocean stratification by considering diurnal cycle effects (Danabasoglu et al. 2006), and so on. Yet, reducing the systematic biases in CGCMs still remains a thorny and challenging issue.

Table 3.1 List of experiments designed in this chapter

<i>Experiments</i>	Descriptions
CTRL	Fully coupled run with 100 years after 300 years spinup
OCN	<p>Climatological daily wind stress forcing is from CTRL, and SWR and longwave radiative fluxes are from the International Satellite Cloud Climatology Project Flux Data (ISCCP-FD) (Zhang et al. 2004), and climatological precipitation from the GPCP. Surface winds, air temperature and specific humidity from the National Centers for Environmental Prediction (NCEP) in combination with ocean model SST are used to calculate surface latent and sensible heat fluxes.</p>
AMSC (annual mean SST correction)	A constant but spatially varying SST damping term is applied to the SST equation (100 years).

Table 3.2 List of models that participate in this study

Modeling group	IPCC ID	Atmospheric resolution	Oceanic resolution
CNRM, France	CNRM-CM3	T63, L45	(0.5° - 2°) × 2°, L31
NOAA GFDL, USA	GFDL-CM21	2.0° × 2.5°, L24	(0.3° - 1°) × 1°
NASA GISS, USA	GISS-ER	4° × 5°, L20	4° × 5°, L13
IAP, China	FGOALS-g1.0	T42, L26	1° × 1°, L16
INM, Russia	INM-CM3.0	4° × 5°, L21	2° × 2.5°, L33
IPSL, France	IPSL-CM4	2.5° × 3.75°, L19	2° × 2°, L31
CCSR/NIES, Japan	MIROC3.2 (hires)	T106, L56	0.2° × 0.3°, L47
CCSR/NIES, Japan	MIROC3.2 (medres)	T42, L20	(0.5° - 1.4°) × 1.4°, L43
MPI, German	ECHAM5/MPI-OM	T63, L31	1.5° × 1.5°, L40
MRI, Japan	MRI-CGCM2.3.2	T42, L30	(0.5° - 2°) × 2.5°, L23
NCAR, USA	CCSM3.0	T85, L26	(0.3° - 1°) × 1°, L40
Hadley Center, UK	UKMO-HadGEM1	1.3° × 1.9°, L38	(0.3° - 1°) × 1°, L40

Table 3.3 Quantitative evaluation of the individual coupling related to the thermocline feedback from observations, AMSC, and CTRL.

	R(u, T)	R(Z20,u)	R(Te,Z20)	\bar{W}	TH
Observation	10.7	63.2	0.87	1.0	549.8
AMSC	8.1	38.4	1.02	1.13	358.5
CTRL	4.7	32.1	0.76	0.83	95.2
CTRL/AMSC	58%	84%	75%	73%	27%

Note: R(u,T): air-sea coupling strength (10^{-2} dyn cm $^{-2}$ °C $^{-1}$) measured by the linear regression of equatorial zonal wind stress (160 °E-130 °W, 5 °S-5 °N) onto the Niño-3 SSTA; R(Z20,u): thermocline depth (Z20) change (averaged over 180 °-80 °W, 2 °S-2 °N) in response to CP (160 °E-130 °W, 5 °S-5 °N) surface wind stress forcing (m cm 2 dyn $^{-1}$); R(Te,Z20): subsurface (60 m) temperature change in response to local thermocline depth (Z20) change (averaged over 180 °-80 °W, 2 °S-2 °N) (10^{-1} °C m $^{-1}$); \bar{W} : mean upwelling (m day $^{-1}$) at 60 m averaged over 180 °-80 °W, 2 °S-2 °N. TH: the intensity of the thermocline feedback. R(u, T) in observation is estimated from ERA40/ERSST and other couplings are observations is from SODA2.0.2.

Chapter 4

Predominance of the central Pacific El Niño after the late 1990s

4.1 Introduction

The interannual variability over the equatorial central Pacific (CP) has received much attention recently that is mainly stimulated by the finding of a new type of El Niño with its maximum warming occurring over the CP (Larkin and Harrison 2005; Ashok et al. 2007; Kao and Yu 2009; Kug et al. 2009; Yeh et al. 2009). In contrast to the conventional El Niño in the eastern Pacific (eastern Pacific Warming, EPW), we refer this El Niño as the central Pacific Warming (CPW). This CPW has occurred more frequently, and the intensity of the CPW has almost doubled in the past three decades together with case 2009 as the strongest CPW on record (Lee and McPhaden 2010).

Comparing with the canonical EPW, the CP-type El Niño exerts distinctly different impacts on worldwide climate, including a shift of anomalous equatorial convection (Ashok et al. 2007; Weng et al. 2007; Weng et al. 2009), increased effectiveness in causing Indian drought (Kumar et al. 2006), reducing rainfall along the west coast of North America (Weng et al. 2007), and increased hurricane frequency in the Atlantic Ocean (Kim et al. 2009). Understanding the mechanism causing the more frequent occurrence of CPW remains a scientific matter of societal importance, which is also of great importance to climate prediction and understanding future changes in ENSO.

A recent study (Yeh et al. 2009) posed one mechanism by emphasizing the contribution from external anthropogenic forcing. Global warming can induce weakened trade winds (Vecchi et al. 2007) and flattened equatorial thermocline. Thus, the CP thermocline depth will be shallower than before, which would enhance the thermocline feedback through vertical advection effect. By investigating the CGCMs from the IPCC AR4, this hypothesis was further supported with the fact that the occurrence ratio of CPW to EPW is projected to increase about 5 times under global warming (Yeh et al. 2009).

However, the uplifted thermocline does not necessitate an enhanced thermocline feedback since mean trades are weakened so that mean upwelling could be suppressed. However, McPhaden et al. (2011) pointed out that the change of background state in recent decades is opposite to those expected from anthropogenic forcing. It is characterized by enhanced trade wind and more tilted thermocline (McPhaden et al. 2011), together with the fact that global warming has leveled off (e.g., Solomon et al. 2010). But it is not well understood how the mean state change influences the El Niño property change. In this study, we offer a mechanism by spotlighting the importance of decadal mean state and annual cycle change.

4.2 Data, Model and Methodology

We use several monthly mean datasets, including surface wind stress from NCEP-DOE (National Centers for Environmental Prediction–Department of Energy) AMIP-II Reanalysis products (Kanamitsu et al. 2002), precipitation from GPCP (Global Precipitation Climatology Project, v2.2) (Adler et al. 2003), and SST from ERSST

(NOAA Extended Reconstructed SST, v3b) (Smith et al. 2008). We also use a ocean reanalysis dataset GODAS (Global Ocean Data Assimilation System) (Behringer and Xue 2004), forced with NCEP-DEO AMIP-II surface wind stress. Due to data availability, the study period is between 1980 and 2010. The anomalous fields are obtained by subtracting them from climatological fields during 1980-2010. To the first-order approximation, we interpret a rising sea surface height (SSH) as a deepened thermocline.

To detect the possible factor governing the decadal variability over the tropical basin, we use the coupled model POEM which couples POP (v2.0) ocean model and ECHAM (v4.6) through the coupler OASIS (v3.0). Two experiments are conducted (Table 4.1). One is the annual mean SST correction (AMSC) run integrating for 100 years. The AMSC is a coupled run but with a 5-day damping term to the SST equation so as to largely eliminate the dipole SST bias problem. More details about model physics and the AMSC experiment can be found in Chapter 2 and 3. The other sensitivity experiment (EXP_AO) is similar with the AMSC run but with an additional annual mean SST nudging (5-day restoring scale) over the Atlantic basin. The SST nudging term is estimated based on the spatial pattern of SST difference between two epochs, 1999-2010 and 1980-1998 (Fig. 4.1b).

4.3 Observed El Niño property change after the late 1990s

The terminologies in describing this new type of El Niño have been diverse (e.g., Ashok et al. 2007; Kug et al. 2009; Kim et al. 2009; Yeh et al. 2009; Kao and Yu 2009; McPhaden et al. 2011), and totally 10 cases in the past three decades have been identified based on various definitions (Table 4.2). Among them there are only 4 robust cases (1994,

2002, 2004, 2009) that exhibit quite similar evolution pattern (Fig. 4.2), and the other 6 are “disputable” cases (1986, 1987, 1990, 1991, 1992, 2001) (Table 4.2). In particular, three out of four robust CPW occurred in the first decade of the 21st century while only one occurred before that. Further, the intensity of the CPW is also increasing and it has almost doubled in the recent three decades (Lee and McPhaden 2010).

Since three out of four robust CPW occurred after the late 1990s, one would wonder whether the behavior of the leading mode of SST anomaly (SSTA) has changed. Figure 4.3 indicates that the first leading empirical orthogonal function (EOF) mode of the tropical SSTA has indeed changed after the late 1990s with its maximum center shifting to the CP. It largely reflects the fact that, during the latter epoch, 3 out of 4 cases are robust CPW cases except one weak EPW event (2006).

What is the major difference between EPW and robust CPW? To address this question, we first compare their time evolutions. Based on the fact that the EPW (CPW) dominates over the first (second) epoch and the majority of the robust CPW occur in the second epoch, we use the cases 1982, 1997 as EPW and 2002, 2004, 2009 as robust CPW to make the composite analysis (Fig. 4.4). For the EPW, deepened thermocline emerges in the equatorial western Pacific (WP) as a precursor of the El Niño, which then proceeds eastward steadily. Once the thermocline anomaly reaches the CP, it propagates eastward rapidly, ending up with a prominent warming in the equatorial EP. Through *Bjerknes* (1969) feedback, the EP warming reinforces anomalous convection and surface westerly anomalies to the west, so that the convection and westerly anomalies migrate eastward accordingly and further feed back to the EP warming (Fig. 4.4a, b). After boreal winter,

warm SSTA also decays from the CP to the EP so that the EP SST warming sustains for a longer period.

By contrast, for the robust CPW, initiation of the deepening thermocline occurs in the region near the dateline (160 °E-160 °W). Although the maximum warming and the deepest thermocline anomaly areas expand toward the EP slowly, both of the maxima never reach the EP, indicating a standing feature. After boreal winter, the weak EP warming decays abruptly while the CP warming persists till the next summer (Fig. 4.4d). In other words, the EP warms up slowly but decays rapidly, resulting in an aborted warming in the EP. In accord with the quasi-stationary oceanic anomalies, the enhanced convection and westerly anomalies are trapped in the region west of 160 °W without clear eastward propagations. Compared with the EPW, this relatively westward shifted anomalous convection and zonal wind stress anomaly (about 20 degrees of longitude) are also apparent in Fig. 4.3c and 4.3d.

In summary, the epochal change of El Niño property is evident. The second epoch has three standing CPW but only one weak EPW (2006), while the 1980-1998 period has only one (1994) standing CPW but two strongest EPW events (1982, 1997) in the 20th century. As such, the leading EOF mode has changed since the late 1990s and the standing CPW becomes dominant mode, which corroborates very well with the change in the frequency of occurrence of the robust or standing CPW events. Then, the question arises, why the warming center tends to preferably occur in the CP and why the warming center does not move into the EP after the late 1990s?

4.4 A new paradigm for the dominance of the CPW

Since ocean-atmosphere mean state variation has a profound impact on ENSO behaviors (e.g. Wang 1995; Fedorov and Philander 2000; An and Wang 2000), investigation of mean state change may be instrumental in clarifying the basic mechanism for the predominance of the standing CPW since the late 1990s.

Figure 4.5 portrays the mean state differences between these two epochs (1999-2009 minus 1980-1998). The SST decadal change exhibits a La Niña-like pattern characterized by SST cooling in the equatorial CP and subtropical eastern Pacific, and SST warming in other regions of the Pacific domain (Fig. 4.5a). The associated mean convection is severely suppressed in the equatorial Pacific particularly near the dateline, cohesive with *in situ* enhanced trades (Fig. 4.5d). We also examine the mean precipitation (averaged over 5°S-5°N, 170°E-130°W), and results show that it are reduced about 27%. An interesting decadal change in the annual cycle is that the equatorial SST cooling and suppressed convection vary coherently with maximum intensity occurring in boreal winter and spring seasons (Fig. 3b).

Considering the short studied period, the decadal mean state change may be partially attributed to the asymmetry of ENSO extreme events [Ashok et al. 2007; Kug et al. 2009; McPhaden et al. 2011]. To examine this possibility, we first remove two extreme El Niño events (1982-83, 1997-98), and this La Niña-like mean state change stays robust (not shown). Further, extreme La Niña events in the second epoch could be another candidate to result in a similar mean state change. Here we adopt 2001-2005 as the second epoch during which there are two El Niño but without La Niña, while the epochal SST difference still exhibits pronounced east-west SST gradient in the equatorial Pacific although the SST cooling is not evident in the EP (not shown). In view of these evidences,

we consider this mean state change mainly a reflection of the decadal variability rather than due to the asymmetry of ENSO events.

How does the mean state change alter the ENSO behaviors? As is well known, anomalous convection to a great degree depends on mean SST and low level wind convergence (e.g., Zebiak 1986; Zebiak and Cane 1987). In association with the SST and precipitation pattern, the mean low-level convergence is significantly reduced over the CP (Fig. 4.5). In the first epoch, there is a weak low-level convergence over the CP (5°S-5°N, 170°E-130°W), while it shows pronounced low-level divergence in the second epoch (Fig. 4.6). Therefore, for the anomalous convection to heat the mid-troposphere, it has to first overcome the mean suppressed convection so that the convection-low level convergence feedback becomes significantly weakened in the second epoch. Both the SST cooling in the EP and enhanced zonal SST gradient in the CP are proposed to be critical in generating the strong low-level divergence and suppressed convection (Fig. 4.5). As such, this mean state change would largely inhibit the development of anomalous deep convection over the CP, causing the nearly stationary convection and low-level wind anomalies confined in the WP. How the mean state change alters the location of anomalous convection has been demonstrated in the current climate models, and the location of convective anomaly largely determines the ability of coupled models in successfully simulating two types of El Niño [Ham and Kug 2011].

In the near-equatorial region, the zonal gradient of thermocline anomaly is approximately proportional to the intensity of zonal wind stress anomaly. Thus, the maximum thermocline anomaly should take place in the region where surface wind changes from westerly to easterly anomalies. In agreement with the surface wind

anomalies, the observed maximum thermocline deepening and SST warming collocate in the CP near 140 °W (Fig. 4.5d). Hence, the decadal change in the annual mean state, to certain extent, accounts for the preferred occurrence of El Niño in the CP during the recent decade.

The westward shifted convection and surface wind anomalies directly influence the periodicity of ENSO. The dominant period of CPW events during 1999-2010 (1-3 years) is shorter than that of the EPW episodes during 1980-1998 (3-5 years) (Fig. 4.3e, f). Based on the “delayed” oscillator mechanism (e.g. Suarez and Schopf 1988; Cane et al. 1990), the ENSO period mainly relies on the time of westward propagating Rossby waves. As seen in Fig.5 of Cane et al. (1990), the westward shifted zonal wind anomaly shortens the distance for the westward propagation of Rossby waves, which shortens the delay and hence shortens the period (An and Wang 2000). This mechanism is a plausible explanation to the relatively shorter periodicity of the CPW in the recent decade.

The above argument emphasizes the favorable mean condition for the development of El Niño in the CP. The predominance of the standing CPW may also be understood from another perspective, that is, El Niño development was not favored in the EP as evidenced by the slow/weak development but rapid decay of SSTA in the EP (Fig. 4.5d). This is arguably caused by the decadal change in the annual cycles of SST and associated easterly trade winds. During boreal winter and spring, the strengthened easterlies make the thermocline shoal to the east and deepen to the west (Fig. 4.5d). The SSH seasonal cycle anomaly attains strongest amplitude with about –6 cm during boreal winter, which would substantially offset the rising SSH associated with an El Niño (Fig. 4.4d). This

readily explains the slow eastward extension of the thermocline anomaly during the onset/development phase of the CPW (Fig. 4.4d).

We further argue that the rapid decay of the EP warming for the standing CPW is attributed to several processes. Firstly, the changed annual cycle can induce strongest thermocline shoaling in the EP during boreal winter and spring, which can result in conspicuous SST cooling (Fig. 4.7b). This cooling is further amplified through intensifying easterlies because of the resultant westward SST gradients (Fig. 4.4, Fig. 4.8). Secondly, the anomalous easterlies in the EP (Fig. 4.2d) associated with the westward shift of the anomalous convection can also contribute to suppress the EP SST warming because of the resultant enhanced latent heat release, upwelling and entrainment. Thirdly, the thermocline shoaling in the CP and EP could also originate from the reflection of oceanic Rossby waves at the western boundary and generation of the eastward propagating upwelling Kelvin waves. After the peak El Niño, the equatorial westerly anomalies are reduced dramatically with their maximum center migrating to the south of the equator (Fig. 4.8) due to the annual cycle change. Consequently, the east-west anomalously tilted thermocline cannot sustain itself, prompting the eastward propagation of upwelling Kelvin wave. This is consistent with “delayed” oscillator mechanism (e.g. Suarez and Schopf 1988; Cane et al. 1990).

For the CPW, the damping mechanism of the CP SST warming is different from that in the EP. The eastward propagation of upwelling Kelvin waves can induce westward geostrophic current by altering the meridional gradient of thermocline anomaly. Associated with the cold zonal advection, this westward current was demonstrated to dominantly determine the decay of the CP warming (Kug et al. 2009). An EOF analysis

of SSH anomaly during the second epoch is performed (Fig. 4.9), and the first two modes are in sharp contrast with those during the first epoch, 1980-1998 (Fig. 4.10). The EOF-1 mode represents the SSH anomaly pattern during El Niño peak phase, with most deepened thermocline over the CP (Fig. 4.9a). Interestingly, a weak westward current is seen near the dateline. We note in particular that the second EOF mode of SSH anomaly closely resembles the eastward propagation of upwelling Kelvin waves and the resultant westward current effect (Fig. 4.9b), which has maximum correlation with EOF-1 mode with a 6-month lag.

4.5 Possible mechanism for the La Nina-like mean state change

Since the La Niña-like mean state change plays the key role in driving the El Niño behavior change in the recent decade, the question arises as to whether this La Niña-like decadal pattern is driven by external anthropogenic forcing or internal natural variability. The majority of climate model experiments suggest that increasing greenhouse gases forcing leads to an El Niño-like global warming together with a weakening Walker circulation (e.g. Vecchi and Soden 2007). Analysis of observed SST for the second half of the 20th century, during which major global warming took place and observations are relatively reliable, indicates that different SST datasets yield a consistent El Niño-like global warming (Fig. 4.11), which seems to corroborate the model results. Hence we advocate that the recent La Niña-like pattern is a manifestation of natural multi-decadal variability.

Besides the La Nina-like pattern over the Pacific domain, it is found that the Atlantic Ocean shows a simultaneous basin wide warming (Fig. 4.1a). Exploring the Atlantic

Multi-decadal Oscillation (AMO) index also reveals that it changed from a negative to a positive phase during around 1995-96, so that the basin wide warming in the Atlantic Ocean in the recent decade may represent the contribution from the AMO. We hypothesize that the basin-wide warming in the Atlantic Ocean is responsible for driving the La Nina-like pattern.

To test this hypothesis, we compare the annual mean state difference between the EXP_AO and AMSC (Fig. 4.12). The Pacific La Nina-like pattern is well reproduced with SST cooling over the equatorial Pacific and SST warming over the subtropical region, although the equatorial maximum cooling ($-0.4\text{ }^{\circ}\text{C}$) displaces westward compared with observations. The resultant low level easterly wind and suppressed precipitation are also apparent over the WP (Fig. 4.12), consistent with observations. Further exploring the seasonal mean state difference reveals that this La Nina-like pattern is most prominent over boreal winter (Fig. 4.13). Therefore, the Atlantic Ocean warming provides one possible mechanism for the formation of the decadal La Nina-like pattern over the Pacific domain.

The influence of Atlantic Ocean SST change on the Pacific climate has been extensively studied in previous studies (Wu et al. 2005; Timmermann et al. 2007; Zhang and Delworth 2007; Xie et al. 2008). Wu et al. (2005) demonstrated that the SST warming in the Atlantic Ocean can drive a cross-equatorial wind over the EP with southeasterly to the south of the equator and southwesterly to the north of the equator. With the aid of wind-evaporation feedback and ocean dynamics, this cross-equatorial wind tends to cause a dipole SST pattern in the EP, SST warming (cooling) to the north (south) of the equator. But this dipole SST pattern is asymmetric about the equator with

the southern cooling much stronger (Fig. 3a in Wu et al. 2005), which further intensifies during the following season associated with Bjerknes (1969) feedback.

4.6 Summary and Discussion

After the late 1990s, El Niño events are observed to occur preferably in the CP with a standing character and shortened periodicity. We describe this type of El Niño as standing CPW or robust CPW. We offer a new mechanism by ascribing this El Niño property change to mean state variation characterized by a La Niña-like pattern. Firstly, this mean state change characterized by a La Niña-like pattern displaces the anomalous convection and zonal wind stress anomalies westward to the vicinity of the dateline, facilitating the SSTA to appear in the CP rather than the EP. Secondly, the associated annual cycle change largely determines the slow development but rapid decay of the EP SST warming, providing an unfavorable condition for El Niño to form in the EP.

Hence we advocate that the recent La Niña-like pattern is a manifestation of natural multi-decadal variability, and we anticipate more CPW events in the coming decades if the La Niña-like pattern would persist. Based on observational and numerical results, we advocate that this La Nina-like mean state change can be driven by the simultaneous Atlantic basin wide warming. Further, the Atlantic basin wide warming is closely linked to the AMO with a typical 60 years period. The changes in El Niño intensity and periodicity have important ramifications on climate predictability.

Table 4.1 Cases of this new type of El Niño for different definitions.

El Niño Modoki (Ashok et al., 2007)	Warm Pool El Niño (Kug et al., 2009)	CPW (Yeh et al., 2009)	CP Warming (Kim et al., 2009)	CPW (McPhaden et al., 2011)
86, 90, 91, 92, 94, 02, 04, 09	90, 94, 02, 04, 09	90, 94, 01, 02, 04, 09	91, 94, 02, 04, 09	87, 94, 02, 04, 09

Table 4.2 List of experiments designed in this chapter

<i>Experiments</i>	Descriptions
AMSC (annual mean SST correction)	A constant but spatially varying SST damping term is applied to the SST equation (100 years).
AO_EXP	Similar with the AMSC run but with an additional annual mean SST nudging (5-day restoring scale) over the Atlantic basin (Fig. 4.1b).

Chapter 5

Dynamics and Predictability of the western North Pacific

Subtropical High

5.1 Introduction

The North Pacific subtropical high (SH) (or anticyclone, AC), covering one third of the northern hemisphere subtropics, is a primary atmospheric circulation system during boreal summer. An enhanced WNP SH (WNPSH) can suppress convection in the WNP monsoon trough (Nitta 1987), causing pluvial Meiyu/Baiu in East Asia (Huang and Wu 1989), reducing *in situ* typhoon activity (Wang and Chan 2002), and causing deficient summer rainfall over the Great Plains of the United States (Wang et al. 2001; Lau and Weng 2002). Opposite situations occur when the WNPSH is weak. Understanding the mechanism and predictability of the WNPSH is a scientific matter of societal importance.

It has been traditionally thought that an enhanced WNPSH occurs during El Niño decaying summer (Wang and Zhang 2002). What causes the enhancement of the WNPSH after a peak El Niño remains debatable. Local air-sea interaction between the AC and sea surface cooling has been suggested as a maintenance mechanism (Wang et al. 2000; Lau and Nath 2003; Wang et al. 2003), but the positive feedback seems to weaken from the spring to summer. Since the Indian Ocean (IO) warming trails a peak El Niño, it has been proposed that the IO warming may change the WNPSH (Wu and Liu 1995). This view has been augmented by some recent studies (Yang et al. 2007; Li et al. 2008; Kim et al. 2009b; Xie et al. 2009; Chowdary et al. 2010; Wu et al. 2009). However, a puzzle is that

the summer IO warming often results from atmospheric forcing without locally enhanced precipitation (Lau and Nath 2000; Wang et al. 2005). Thus, the cause-and-effect relationship between the WNPSH and the IO warming needs re-evaluation. Sui et al. (2007) and Chung et al. (2011) argued that the fluctuation of the WNPSH can be separated into two oscillations, one is 2-3 years and the other is 3-5 years. The 2-3 year oscillation is mainly driven the maritime continent heating and the 3-5 year oscillation is forced by the local SSTA in the WNP. However, it is not clear about the physical explanation of the period selection for these two different forcing effects.

First, we point out that more than half of the strong anomalous WNPSH cases do not concur with decaying El Niño and IO warming. Similar to Sui et al. (2007), we measure the strength of WNPSH by an index defined by the 850 hPa geopotential height (H850) anomaly averaged in the region (15°N-25°N, 115°E-150°E), where maximum interannual variability is located (Fig. 5.1a). Figure 5.1b shows pronounced interannual variation of the WNPSH index. Among 9 strong WNPSH events (1980, 1983, 1987, 1988, 1993, 1995, 1996, 1998, and 2003), only 4 (1983, 1988, 1995, and 1998) concurred with El Niño decay (Fig. 5.2) and 5 (1983, 1987, 1988, 1998, and 2003) concurred with IO warming (Fig. 5.3). This suggests a necessity for broadening our conventional thinking on the causes of the WNPSH variation.

5.2 Data and Methodology

Several datasets are used in this study, including 1) monthly mean SST from NOAA Extended Reconstructed SST (ERSST,v3b) (Smith et al. 2008); 2) monthly mean precipitation from Global Precipitation Climatology Project (GPCP, v2.1) datasets (Adler

et al. 2003); and 3) monthly mean 850 hPa wind, geopotential height and sea level pressure from National Centers for Environmental Prediction–Department of Energy (NCEP–DOE) Reanalysis 2 products (Kanamitsu et al. 2002). We also use Joint Typhoon Warning Center (JTWC) “best track” data to estimate the positions of TS (www.npmoc.navy.mil/jtwc.html). The “best track” data for TS positions are first transformed into an area-averaged TS frequency at 5×5 degree point. The TSDs are then defined as the averaged TS occurrence divided by 4 since the “best track” data for TS positions are reported every 6 hours. Ocean surface latent heat fluxes (1979-2009) is from objectively analyzed air-sea fluxes (OAFlux) (Yu and Weller 2007). Summer (July-August, JJA) anomalies are calculated by the deviation of JJA mean from the 31-year climatology (1979-2009).

Two atmospheric models, the ECHAM4 model (Roeckner et al. 1996) with T42 resolution in the horizontal and 19 levels in the vertical and an intermediate atmospheric model (Fu and Wang, 1999; Wang and Li 1993, also referred to as WLF model) are adopted in this study. Two sets of experiments are carried out by using ECHAM4 model. One is a control run (20-yr) forced with observed climatological SST and sea ice, and the other is a sensitivity experiment (20 ensemble members) with imposed cold SSTA (red contour lines in Fig. 5.7d) in the WNP during JJA (Xiang et al. 2011).

The north Atlantic Oscillation (NAO) index used in this study is defined by the difference of the normalized sea level pressure (SLP) anomaly (zonal averaged from 80°W to 30°E) between 35°N and 65°N over the North Atlantic sector (Li and Wang 2003). The cross validation method (Michaelsen 1987) is used to make a re-forecast of the WNPSH intensity by using the three predictors. The cross-validation method

systematically deletes 3 year from the period 1979–2008, derives a forecast model from the remaining years, and tests it on the deleted cases.

5.3 Results

5.3.1 Dynamics controlling the variability of the WNPSH

A WNPSH positive index represents an enhanced AC centered at (20°N, 140°E), with suppressed rainfall to its southeast flank and above-normal rainfall to its northwest and southwest (Fig. 5.1c). In fact, both the first and second empirical orthogonal functions of the Asian summer precipitation are significantly correlated with the WNPSH index with $r = 0.58$ and 0.56 , respectively (Fig. 5.4). The abundant rainfall in the subtropical East Asia (the Chinese Meiyu, Japanese Baiu, and Korean Changma), corresponds to a strong East Asian Summer Monsoon, which can be measured by the leading principal component of the precipitation and East Asian circulation (Wang et al. 2008). The WNPSH index is highly indicative of the EASM intensity with a correlation coefficient $r = -0.92$ (Fig. 5.5a). Further, an enhanced WNPSH signifies reduced tropical storm days (TSDs) over the WNP and East Asian coastal zones (Fig. 5.5b) as evidenced by the significant correlations between the WNPSH index and the total number of TSDs occurring over the subtropical WNP ($r = -0.73$) and the landing TS over the East Asian coastal zones ($r = -0.66$) for 1979-2009 (Fig. 5.5a). Therefore, understanding the mechanisms and predictability of the WNPSH has critical implication in improving the prediction of the TS over the WNP.

To unravel the origin of the WNPSH fluctuation, we first identify the major modes of the variability. An empirical orthogonal function (EOF) analysis of H850 reveals two

leading modes that are statistically distinguished from each other and other modes; they account for 31.2% and 20.9% of the total variance over the entire Asian-Australian monsoon region. The EOF-1 is characterized by an intense southwest-northeast oriented WNPSH, which concurs with suppressed rainfall on its southeast flank and enhanced rainfall in the equatorial Pacific and the subtropical East Asia (Fig. 5.6).

How can this mode sustain itself given the chaotic nature of the atmospheric motion? A clue lies with the coexistence of an enhanced WNPSH and a dipolar SST anomaly (SSTA), i.e., the cooling to the southeast of the AC in the WNP and the warming to the southwest of the AC over the northern IO (NIO) (Fig. 5.6c). This “coupled” pattern suggests a positive feedback between the WNPSH and underlying Indo-Pacific dipole SSTA.

At the southeast of the AC, anomalous northeasterlies tend to cool the ocean surface by strengthening mean easterlies, thereby enhancing evaporation and entrainment (Fig. 5.7). The resultant ocean surface cooling along with the southward dry advection would in turn reduce *in situ* precipitation heating, hence generating descending Rossby waves that reinforce the AC in their westward decaying journey (Wang et al. 2000). Numerical experiments with an atmospheric general circulation model forced by the SST cooling in the WNP can reproduce realistic precipitation and H850 anomalies (Fig. 5.6d). Note that during boreal summer, even a moderate-magnitude SST perturbation can induce prominent precipitation anomaly in the WNP, but with boreal spring mean state the same SST cooling cannot replicate the observed WNPSH anomaly (Fig. 5.8).

To the southwest of the AC, the easterly anomalies associated with the WNPSH ridge extend from the South China Sea to the NIO (Fig. 5.6c), which weakens southwest

monsoon and suppresses monsoon precipitation/cloudiness, thereby warming the NIO through reduced surface latent heat flux (Du et al. 2009) and increased insulation. Then how does the NIO warming feed back to the WNPSH without anomalous precipitation (Fig. 5.6a)? If there were no local warming, the Indian monsoon rainfall would be deficient due to the subsidence associated with the WNPSH ridge (Chowdary et al. 2010). A deficient monsoon would weaken the WNPSH by exciting low-level equatorial westerlies over the western Pacific (Kelvin wave response) and generating off-equatorial cyclonic shear vorticity over the Philippine Sea (Gill 1980). Thus the NIO warming tends to increase local rainfall (albeit invisible), offsetting the otherwise deficient rainfall and indirectly sustaining the WNPSH.

Therefore, we refer to the EOF-1 mode as an IO-WNP anticyclonic coupled mode, and the local cold SSTA in the southeast flank of the anticyclone acts as a critical component of this coupled system. This system can be self-maintained associated with the increases wind speed and enhanced latent heat flux especially to the southeast flank of the AC (Fig. 5.9). However, we do not preclude some other processes that may also contribute to this cold SSTA, for example, as a persisted cold SSTA from boreal spring (Wu et al. 2010), cold SSTA migrating from the north Pacific (personal communication with Tim Li).

The EOF-2 features an anomalous high pressure in the WNP and low pressure over the tropical IO and maritime continent (Fig. 5.10a). The anticyclonic ridge tilts in a northwest-southeast orientation, and the associated suppressed convection extends from the Philippine Sea to the equatorial western Pacific. The enhanced AC is concurrent with a notable cooling in the equatorial central Pacific (Fig. 5.10c). In fact, the majority of the

enhanced SH cases are in accord with developing or persisting La Niña events (1988, 1995, 1996, 1998, 1999, 2000, 2007, and 2008), while the weakened AC cases concur with El Niño development over the central Pacific (1982, 1986, 1997, 2002, and 2004) (Fig. 5.10b).

The central Pacific cooling can reinforce the WNPSH through shifting the Walker cell, thus reducing convection in the equatorial western Pacific (around 160°E) and increasing convection over the maritime continent (Fig. 5.10a). The suppressed convection around 160°E can directly boost the WNPSH by emanation of descending Rossby waves (Gill 1980; Terao and Kubota 2005). The reinforced maritime continental convection can also enhance the WNPSH via drawing equatorial easterlies over the western Pacific, which generates off-equatorial anticyclonic shear vorticity over the Philippine Sea. These explanations are confirmed by numerical experiments with an intermediate atmospheric model: Both the reduced heating in the equatorial western Pacific and enhanced heating over the maritime continent can generate anticyclonic vorticity over the WNP (Fig. 5.11). With the aid of boundary friction, this negative vorticity can induce boundary layer divergence, which, in the presence of moisture feedback, would further suppress convection and reinforce the WNPSH anomaly. Different from Sui et al. (2007) and Chung et al. (2011), here we emphasize the importance of the forcing from the equatorial central Pacific rather than the maritime continent heating. There are two reasons. Firstly, the SST warming in the maritime continent can be a part of La Niña forcing, at least partly. Secondly, the central Pacific cooling induces more stronger low-level vorticity over the WNP (Fig. 5.11) and can explain the southeast-northwest tilt structure in EOF-2.

5.3.2 Predictability of the WNPSH

The interannual variation of the WNPSH intensity can be faithfully reconstructed by using the two principal components (PCs): $(1.226 \times \text{PC-1} + 1.245 \times \text{PC-2})$, which together account for about 88% of the total variance of the WNPSH (Fig. 5.12a). Interestingly, the EOF-2 is more closely correlated ($r = 0.73$) with the WNPSH index than the EOF-1 mode ($r = 0.60$), suggesting the importance of the central Pacific SST forcing.

Skillful prediction of the WNPSH is of utmost importance to the seasonal forecast of the Asian-Pacific climate. Encouraged by the successful reconstruction with these two modes, we built a physics-based empirical model for prediction of the WNPSH intensity:

$$\text{WNPSH} = 1.756 \times \text{SSTA (IO-WNP)} - 0.435 \times \text{ENSO}_{\text{develop}} - 0.282 \times \text{NAOI} \quad (1)$$

where SSTA (IO-WNP) represents the SSTA difference between the IO (10 °S-10 °N, 50 °E-110 °E) and the WNP (0 °-15 °N, 120 °E-160 °E) during April-May, $\text{ENSO}_{\text{develop}}$ denotes the May-minus-March SSTA in the central Pacific (5 °S-5 °N, 170 °W-130 °W), and NAOI is North Atlantic Oscillation index (Li and Wang, 2003) in April-May. The IO-WNP dipole SSTA is significantly correlated with EOF-1 mode ($r = 0.76$), whereas the $\text{ENSO}_{\text{develop}}$ and NAOI are significantly correlated with EOF-2 mode ($r = -0.52$ and $r = -0.41$, respectively). The selection of NAOI is based on recent studies that identify NAOI as a complementary predictor for East Asian-WNP summer monsoon (Wu et al. 2009; Gong et al. 2011). Physically, the NAOI foresees the equatorial Pacific SSTA, which links to EOF-2. The physical linkage between these three predictors and the WNPSHI is illustrated in Fig. 5.13. The coefficient of each predictor is determined based on multivariate regression method. The simulation using equation (1) reproduces the

WNPSH index with a high correlation ($r= 0.81$) (Fig. 5.12b). To test the predictive capability of this model, a cross-validation method (Michaelsen 1987) is used to re-forecast the WNPSH index (1979-2009) by choose a leaving-three-out approach (Blockeel and Struyf 2002). The correlation coefficient between the observation and the 31-year cross-validated estimates of the empirical model is 0.75 (Fig. 5.12b).

As a comparison, we have also assessed the performance of three state-of-the-art coupled climate models in seasonal hindcast of the WNPSH index for the 24-year period during 1982-2005. These models have participated in the APEC Climate Center/Climate Prediction and its Application to Society (CliPAS) project (Wang et al. 2009; Lee et al. 2011) (Fig. 5.14). The results indicate that the physical-empirical model yields a comparable skill with the state-of-the-art dynamical models (r varies from 0.73 to 0.80). Similarly, by using these three factors, we examined the hindcast skill of this empirical model for the WNP TSDs and landing TS to the east Asia. The correlation can reach 0.60, 0.54 with observations, respectively. Since the predictors can be easily monitored in real time, this empirical model can be used in operational forecasts without relying on pre-forecasted SST.

5.4 Summary and Discussion

The WNPSH has profound impacts on Asian summer monsoon, North Pacific storms and North American summer rainfall. Skillful prediction of the WNPSH is of utmost importance to the seasonal forecast of Asian-Pacific climate, especially the strength of East Asian summer monsoon and the tropical storms days affecting East Asian countries. Here we show that the variation of the WNPSH is primarily determined by a remote

cooling/warming in the equatorial central Pacific and a positive thermodynamic feedback between the local circulation and a dipole sea surface temperature in the Indo-Pacific warm pool. A surprise is that an empirical model established based on the characteristics of these two processes can capture about 88% of the intensity variation at the WNPSH action center. We demonstrate that a physical-empirical prediction model built on these physical understandings has comparable performance with those of three state-of-the-art coupled climate models in re-forecast of the strength of the WNPSH for the period 1979-2009. These results have important implications for predicting East Asian summer monsoon and WNP tropical storms.

Some previous studies emphasized the importance of the IO warming on the maintenance of the WNPSH. In this study, we prefer to regard that the IO warming provides a precondition for the development of the WNPSH, while it is not essential in driving the anomalously suppressed precipitation and the associated high pressure over the WNP. By comparing two experiments with and without boreal summer mean flow, the easterly anomaly is weaker in the NIO for the case without mean flow (Fig. 5.15). This is due to the strong mean easterly shear in the NIO during boreal summer, which can enhance the low level Rossby wave response (Wang and Xie 1996). From this point of view, the NIO warming, to some degree, reflects the remote forcing effect from the intensified WNPSH.

The mechanisms revealed in this study bear important implications for better understanding and prediction of the East Asian summer monsoon and Pacific tropical storm activity. However, we have noticed the non-stationary nature of interannual variation of the WNPSH. The EOF-1 has weakened since the late 1990s (Fig. 5.6b). This

is likely a consequence of the prominent warming in the western Pacific that is hostile for developing the interannual cooling to the southeast of the AC (Fig. 5.16) and deteriorates the positive thermodynamic feedback that sustains the AC. It is also noted that the interannual variability is much weaker before the mid-1970s (Fig. 5.17). These aspects of interdecadal variability call for further investigations of the potential roles of the natural variability and external anthropogenic forcing.

Chapter 6

Summary and Future Work

6.1 Summary

6.1.1 Mean SST bias in the newly developed coupled model POEM

We have build a coupled model, namely POEM, which couples the POP (v2.0) ocean model and ECHAM (v4.6) atmospheric model through the coupler OASIS (v3.0). The main purpose to develop this coupled model is study the dynamics and interactions among ENSO, monsoon and MJO. This model has produced reasonable boreal summer monsoon system and MJO simulation both in boreal summer and winter. Thus it provides a potential to have intraseasonal and seasonal forecast.

However, this model suffers serious double ITCZ problem. The counterpart of the double ITCZ problem in SST exhibits an excessive cold tongue extension and warm SST bias over the SEP. The warm SST bias over the SEP tends to be mainly caused by the errors in simulating low-level clouds (e.g. Ma et al. 1996) and the marine boundary air-sea feedbacks. The cold SST bias over the equatorial Pacific can reach $-0.4\text{ }^{\circ}\text{C}$ which is attributed to two different processes. The first one is due to the deficiency of ocean dynamics (likely related to upwelling and turbulent mixing) which can produce $-1.5\text{ }^{\circ}\text{C}$ equatorial cooling. The second is associated with the heat flux bias from the atmospheric model. This heat flux bias can also induce a significant cold SST bias (about $-1.5\text{ }^{\circ}\text{C}$) but with its maximum center shifting westward to the WP. It provides two different

directions to alleviate this problem which still remains a common and challenging problem for the majority of current CGCMs.

6.1.2 Reduction of the thermocline feedback associated with mean SST bias in ENSO simulation

Based on three experiments, we demonstrated that the thermocline feedback is grossly suppressed in the fully coupled run (CTRL), which is only 27% of that in a sensitivity experiment with annual mean SST correction (AMSC). The underestimated thermocline feedback is explained through four different underestimated processes, the air-sea coupling strength, wind-thermocline feedback, thermocline-subsurface temperature coupling and mean upwelling. All these processes can be explained by the dipole SST bias pattern. Firstly, excessive cold tongue extension tends to push the anomalous convection westward, and the amplitude of anomalous convection is also reduced because of the cold SST bias-induced less low-level moisture and its convergence. Therefore, the surface wind in response to SSTA becomes weaker. Secondly, in the CTRL, zonal wind anomaly mainly results from zonal SSTA gradient instead of anomalous convection, which exhibit weak meridional gradient structure. This meridionally uniform pattern of zonal wind stress is arguably responsible for the weakened wind-thermocline feedback. Thirdly, the equatorial cold SST bias is able to enhance turbulent mixing so that the stratification is reduced at the bottom of the mixed layer. The same magnitude of thermocline fluctuation can induce less subsurface temperature anomaly associated with the weakened stratification so that the thermocline-subsurface temperature coupling is underestimated. Finally, both dynamic and

thermodynamic effects associated with the dipole SST bias pattern contribute to a weakening mean upwelling over the equatorial Pacific. The dipole SST bias underestimates the mean upwelling through (a) undermining equatorial mean easterly wind stress, and (b) enhancing convective mixing and thus reducing the upper ocean stratification, which weakens vertical shear of meridional currents and near-surface Ekman-divergence.

6.1.3 Predominance of the central Pacific El Niño after the late 1990s

In recent decades, El Niño events have occurred more frequently over the equatorial central Pacific (CP). This location shift from the eastern Pacific (EP) to the CP largely alters its conventional atmospheric teleconnection pattern as well as its global climate impacts. Global warming has been proposed to be one mechanism responsible for this location shift associated with the weakening trade winds and the flattening of the equatorial thermocline (Yeh et al. 2009]. Here, we show that since the late 1990s the standing CPW becomes a dominant mode, but the trade winds have strengthened and the equatorial thermocline slope has increased. We ascribe this predominance of the standing CPW to a dramatic decadal change in the Pacific mean state and annual cycle. The mean state change characterized by a decadal La Niña-like pattern tends to anchor convection and surface zonal wind anomalies to the vicinity of the dateline, facilitating surface warming to occur in the CP. The annual cycle change, with the trade winds intensifying during boreal winter and spring, prevents the warming development but helps the warming decay in the EP. Based on a sensitivity experiment, we demonstrated that the La Niña-like pattern could be a result of the decadal/multidecadal Atlantic Ocean warming.

More CPW events are expected in the coming decade if the La Niña-like global warming pattern would persist.

6.1.4 Dynamics and predictability of the WNPSH

At the western edge of the SH, the WNPSH shows strong interannual variability that exerts profound impacts on the Asian-Pacific climate and tropical cyclone activities. Investigation of its mechanisms and practicability is a scientific matter of societal importance. By using an EOF analysis, we unveil that two different mechanisms are proposed to be dominantly responsible for the pulse of the WNPSH. One is associated with the remote forcing associated with the central Pacific cooling, and the other is related to a local thermodynamic feedback in the Indo-Pacific warm pool region. These two processes can account for 88% of the total variance of the WNPSH. Based on these results, we built an empirical model which has high prediction skill comparable to that in three state-of-the-art coupled climate models. This study also provides potential implications for the prediction of the WNP TDs and landing TS.

6.2 Future Work

I plan to further work on three issues related to this dissertation.

- 1) Alleviating the mean SST bias in the POEM coupled model. The excessive SST warming in the SEP is usually a result of the simulated deficient low-level clouds and the associated local air-sea feedbacks. We can find that both the ocean and atmospheric models contribute about half-half of the excessive cold tongue extension

- problem. It implies that we need to work on two different aspects to alleviate this SST bias, while I also realize this is a very challenging and long-term project.
- 2) We provide one possible mechanism of the predominance of the CPW in recent decades. We admit both the frequency and intensity changes are not statistically significant by only focusing on the recent three decades. Thus, we plan to investigate the historical SST data and coupled model simulations to test our current hypothesis of the CPW and mean state relationship. Especially, we will conduct some sensitivity experiments by using the coupled model POEM to test whether an imposed La Nina-like pattern will help produce more CPW events. Another sensitivity experiment can be done is to study its development for an initial SST warming perturbation with different background mean state.
 - 3) We will investigate what causes the anomalous SST cooling in the southeast flank of the WNPSH, due to local thermodynamic feedback, mid-latitude forcing or as a cold SSTA persisting from boreal spring to boreal summer? Further, the first two leading EOF modes of H850 are not evident during the period of 1948-1979, and the intensity of the WNPSH has increased significantly after the late 1970s. We aim to further investigate the possible reasons for this decadal variability. Our hypothesis is related to the fact that after the late 1970s, the majority of the ENSO is emerging from the CP which has more direct impacts on the WNP. Further, the local thermodynamic feedback is also suggested to be enhanced. Both these two processes are arguably to control the decadal intensity change of the WNPSH. Another future work is to investigate the hindcast model performance in simulating the IO-WNP anticyclonic mode, ENSO developing mode and NAO mode which are closely related to the

prediction of the WNPSH. In terms of WNPSH prediction during boreal summer (JJA), we will further study its prediction skill with one month lead and we expect that the empirical model can achieve better prediction skill than the dynamical models.

References:

- AchutaRao K. Sperber K. (2002) Simulation of the El Niño Southern Oscillation: Results from the Coupled Model Intercomparison Project. *Clim Dyn* 19:191–209
- AchutaRao K. Sperber K. (2006) ENSO simulation in coupled ocean-atmosphere models: Are the current models better? *Clim Dyn* 27:1–16
- Adler RF, and Coauthors (2003) The Version-2 Global Precipitation Climatology Project (GPCP) monthly precipitation analysis (1979-present). *J Hydrometeor* 4:1147–1167
- An S-I (2008) Interannual variations of the tropical ocean instability wave and ENSO. *J Clim* 21:3680–3686
- An S-I, Jin F-F (2001) Collective role of thermocline and zonal advective feedbacks in the ENSO mode. *J Clim* 14:3421–3432
- An S-I, Ham Y-G, Kug J-S, Timmermann A, Choi J, Kang I-S (2010) The inverse effect of annual-mean state and annual-cycle changes on ENSO. *J Clim* 23:1095–1110
- An S-I, Wang B (2000), Interdecadal change of the structure of ENSO mode and its impact on the ENSO frequency. *J Clim* 13:2044–2055
- Annamalai H, Hamilton K, and Sperber KP (2007) South Asian Summer Monsoon and its relationship with ENSO in the IPCC AR4 simulations. *J Clim* 20:1071–1092
- Ashok, Behera KS, Rao AS, Weng H, and Yamagata T (2007), El Niño Modoki and its teleconnection. *J Geophys Res* 112, C11007, doi:10.1029/2006JC003798
- Annamalai H, Hamilton K, Sperber KR (2007) South Asian Summer Monsoon and its relationship with ENSO in the IPCC AR4 simulations. *J Clim* 20:1071–1092
- Barnett TP, Latif M, Kirk E, Roeckner E (1991) On ENSO physics. *J Clim* 4:487–515

- Behringer DW, Xue Y (2004) Evaluation of the global ocean data assimilation system at NCEP: The Pacific Ocean. Eighth Symposium on Integrated Observing and Assimilation Systems for Atmosphere, Oceans, and Land Surface, AMS 84th Annual Meeting, Washington State Convention and Trade Center, Seattle, Washington, 11–15
- Bjerknes J (1969) Atmospheric teleconnections from the equatorial Pacific. *Mon Wea Rev* 97:163–172
- Blanke B, Delecluse P (1993) Variability of the tropical Atlantic ocean simulated by a general circulation model with two different mixed layer physics. *J Phys Oceanogr* 23:1363–1388
- Blokeel H, Struyf J (2002) Efficient algorithms for decision tree cross- validation. *J Mach Learning Res* 3:621–650
- Brohan P, Kennedy JJ, Harris I, Tett SFB, Jones PD (2006) Uncertainty estimates in regional and global observed temperature changes: a new dataset from 1850. *J Geophys Res* 111, D12106, doi:10.1029/2005JD006548
- Brown K (1969) A numerical method for the study of the circulation of the world ocean. *J Comput Phys* 4:347
- Cane MA, Matthias M, Zebiak SE (1990) A study of self-excited oscillations of the tropical ocean-atmosphere system. Part I: Linear analysis. *J Atmos Sci* 47:1562–1577
- Carton JA, Giese BS, Grodsky SA (2005) Sea level rise and the warming of the oceans in the SODA ocean reanalysis, *J Geophys Res* 110 doi:10.1029/2004JC002817
- Chang C-P, Zhang Y, and Li T (2000) Interannual and interdecadal variations of the East Asian summer monsoon and the tropical sea-surface temperatures. Part I: Roles of the subtropical ridge. *J Clim* 13:4310–4325

- Chowdary JS et al. (2010) Predictability of Northwest Pacific climate during summer and the role of the tropical Indian Ocean. *Clim Dyn*, doi:10.1007/s00382-009-0686-5
- Chung PH, Sui C-H, Li T (2011) Interannual relationships between the tropical sea surface temperature and summertime subtropical anticyclone over the western North Pacific. *J Geophys Res* 116, doi:10.1029/2010JD015554
- Cronin MF, Kessler WS (2009) Near-Surface shear flow in the tropical Pacific cold tongue front. *J Phys Oceanogr* 39:1200–1215
- Danabasoglu G, Large WG, Tribbia, JJ, Gent PR, Briegleb BP (2006) Diurnal coupling in the tropical oceans of CCSM3. *J Clim* 19:2347–2365
- Deser C, Phillips AS, Alexander MA (2010) Twentieth century tropical sea surface temperature trends revisited. *Geophys Res Lett* 37:L10701. Doi:10.1029/2010GL043321
- Du Y, Xie S-P, Huang G, Hu K (2009) Role of air-sea interaction in the long persistence of El Niño-induced North Indian Ocean warming. *J Clim* 22:2023–2038
- Dukowicz JK, Smith RD, Malone RC (1993) A reformulation and implementation of the bryan-cox-semtner ocean model on the connection machine. *Atmos Ocean Tech* 10:195-208.
- Dukowicz JK, Smith RD (1994) Implicit free-surface method for the bryan-cox-semtner ocean model. *J Geophys Res* 99:7991–8014
- Fedorov AV, Philander SGH (2000) Is El Niño changing? *Science* 288:1997–2002.
- Fu X, Wang B (1999) The role of longwave radiation and boundary layer thermodynamics in forcing tropical surface winds. *J Clim* 12:1049–1069
- Gent PR, McWilliams JC (1990) Isopycnal mixing in ocean circulation models. *J Phys Oceanogr* 20:150–155

- Giese BS, Ray S (2011) El Nino variability in simple ocean data assimilation (SODA), 1871-2008. *J Geophys Res* 116:C02024, doi:10.1029/2010JC006695
- Gill AE (1980) Some simple solutions for heat-induced tropical circulation. *Quart J Roy Meteor Soc* 106:447–462
- Gong D-Y et al. (2011) Spring Arctic Oscillation-East Asian summer monsoon connection through circulation changes over the western North Pacific. *Clim Dyn*, doi:10.1007/s00382-011-1041-1
- Guilyardi E, Braconnot P, Jin F-F, Kim ST, Kolasinski M, Li T, Musat I (2009a) Atmosphere feedbacks during ENSO in a coupled GCM with a modified atmospheric convection scheme. *J Clim* 22:5698–5718
- Guilyardi E, Wittenberg A, Fedorov A, Collins M, Wang C, Capotondi A, Oldenborgh GJV, Stockdale T (2009b) Understanding El Niño in ocean-atmosphere general circulation models. *Bull Amer Meteor Soc* 90:325–340
- Guilyardi E (2006) El Niño-mean state-seasonal cycle interactions in a multi-model ensemble. *Clim Dyn* 26:329–348
- Guldberg A, Kaas E, Deque M, Yang S, Vester T S (2005) Reduction of systematic errors by empirical model correction impact on seasonal prediction skill. *Tellus* 57A:575–588
- Ham Y-G, Kug J-S (2011) How well do current climate models simulate two-type of El Niño? *Clim Dyn*, doi:10.1007/s00382-011-1157-3.
- Huang R, Wu Y (1989) The influence of ENSO on the summer climate change in China and its mechanism. *Adv Atmos Sci* 6:21–32
- Jiang X, Li T (2005) Re-initiation of the boreal summer intraseasonal oscillation in the tropical Indian Ocean. *J Clim* 18:3777–3795

- Jin F-F (1997) An Equatorial Ocean Recharge Paradigm for ENSO. Part I: Conceptual Model. *J Atmos Sci* 54:811–829.
- Jin F-F, Kim ST, Bejarano L (2006) A coupled stability index for ENSO. *Geophys Res Lett* 33:L23708. doi:10.1029/2006GL027221
- Jin F-F, Lin L, Timmermann A, Zhao J (2007) Ensemble-mean dynamics of the ENSO recharge oscillator under state-dependent stochastic forcing. *Geophys Res Lett* 34:L03807. doi:10.1029/2006GL027372
- Johnson GC, McPhaden MJ (2001) Equatorial Pacific Ocean horizontal velocity, divergence, and upwelling. *J Phys Oceanogr* 31:839–849
- Joseph R, Nigam S (2006) ENSO evolution and teleconnections in IPCC's twentieth-century climate simulations Realistic representation? *J Clim* 19:4360–4377
- Kalnay E et al. (1996) The NCEP/NCAR 40-year reanalysis project. *Bull Am Meteorol Soc* 77:437–471
- Kanamitsu M et al. (2002) NCEP-DEO AMIP-II Reanalysis (R-2). *Bull Amer Met Soc* 83:1631–1643
- Kao H-Y, Yu J-Y (2009) Contrasting eastern-Pacific and central Pacific types of El Niño. *J Clim* 22:615–632, doi:10.1175/2008JCLI2309.1
- Kim D, Kug J-S, Kang I-S, Jin F-F, Wittenberg AT (2008) Tropical Pacific impacts of convective momentum transport in the SNU coupled GCM. *Clim Dyn* 31:213–226
- Kim H, Webster P, Curry J (2009a) Impact of shifting patterns of Pacific Ocean warming on north Atlantic tropical cyclones. *Science* 325:77–80
- Kim J-E, Yeh S-W, Hong S-Y (2009b) Two types of strong Northeast Asian summer monsoon. *J Clim* 22:4406–4417

- Kim ST, Jin F-F (2010) An ENSO stability analysis Part II: results from the twentieth and twenty-first century simulations of the CMIP3 models. *Clim Dyn* doi10.1007/s00382-010-0872-5
- Kucharski F, Kang I-S, Farneti R & Feudale L (2011), Tropical Pacific response to 20th century Atlantic warming. *Geophys Res Lett* 38, L03702, doi:10.1029/2010GL046248
- Kug J-S, Jin F-F, and An S-A (2009) Two types of El Niño events: Cold tongue El Niño and warm pool El Niño. *J Clim* 22:1499–1515, doi:10.1175/2008JCLI2624.1
- Kumar KK, Rajagopalan B, Hoerling M, Bates G, Cane M (2006) Unraveling the mystery of Indian Monsoon failure during El Niño. *Science* 314:115–119
- Lagerloef GSE, Mitchum GT, Lukas RB, Niller PP (1999) Tropical Pacific near-surface currents estimated from altimeter, wind, and drifter data. *J Geophys Res* 104(C10): 23313–23326
- Large WG, McWilliams JC, Doney SC (1994) Oceanic vertical mixing A review and a model with a nonlocal boundary layer parameterization. *Rev Geophys* 32:363–403
- Large WG, Danabasoglu G, Doney SC, McWilliams JC (1997) Sensitivity to surface forcing and boundary layer mixing in a global ocean model Annual-mean climatology. *J Phys Oceanogr* 27:2418–2447
- Large WG, Danabasoglu G (2006) Attribution and impacts of upper-ocean biases in CCSM3. *J Clim* 19:2325–2346
- Larkin NK, Harrison DE (2005) Global seasonal temperature and precipitation anomaly during El Niño autumn and winter. *Geophys Res Lett* 32, L16705, doi:10.1029/2005GL022860

- Latif M, and co-authors (2001) ENSIP: the El Niño simulation intercomparison project. *Clim Dyn* 18:255–276
- Latif M, and Keenlyside NS (2009) El Niño/Southern Oscillation response to global warming. *PNAS* 106: 20578–20583
- Lau KM, Weng H (2002) Recurrent teleconnection patterns linking summertime precipitation variability over East Asia and North America. *J Meteorol Soc Japan* 80:1309–1324
- Lau N-C, Nath MJ (2000) Impact of ENSO on the variability of the Asian-Australian monsoons as simulated in GCM experiments. *J Clim* 13:4287–4309
- Lau N-C, Nath MJ (2003) Atmosphere-ocean variations in the Indo-Pacific sector during ENSO episodes. *J Clim* 16:3–20
- Lau N-C, Leetmaa A, Nath MJ, Wang H-L (2005) Influences of ENSO-induced Indo-Western Pacific SST anomalies on extratropical atmospheric variability during the boreal summer. *J Clim* 18:2922–2942
- Lee J-Y et al. (2011) How predictable is the Northern Hemisphere summer upper-tropospheric circulation? *Clim Dyn*, In Press, doi: 10.1007/s00382-010-0909-9
- Lee T, McPhaden MJ (2010) Increasing intensity of El Niño in the central-equatorial Pacific. *Geophys Res Lett* 37, L14603, doi:10.1029/2010GL044007
- Li J, Wang J (2003) A new North Atlantic Oscillation index and its variability. *Adv Atmos Sci* 20(5):661–676
- Li S, Lu J, Huang G, Hu K (2008) Tropical Indian Ocean basin warming and East Asian summer monsoon: A multiple AGCM study. *J Clim* 21:6080–6088

- Li T (1997) Phase transition of the El Niño-Southern Oscillation: A stationary SST mode. *J Atmos Sci* 54:2872–2887
- Li T (2006), Origin of the summertime synoptic-scale wave train in the western North Pacific. *J Atmos Sci* 63:1093–1102
- Li T, Hogan TF (1999) The role of annual-mean climate on seasonal and interannual variability of the tropical Pacific in a coupled GCM. *J Clim* 12:780–792
- Lin J-L (2007) The double-ITCZ problem in IPCC AR4 coupled GCMs Ocean-Atmosphere feedback Analysis. *J Clim* 20:4497–4525
- Lindzen RS, Nigam S (1987) On the role of sea surface temperature gradients in forcing low-level winds and convergence in the tropics. *J Atmos Sci* 44, 2418–2436
- Lloyd J, Guilyardi E, Weller H (2010) The role of atmosphere feedbacks during ENSO in the CMIP3 models Part II using AMIP runs to understand the heat flux feedback mechanisms. *Clim Dyn* doi10.1007/s00382-010-0895-y
- Liu L, Yu W, Li T (2011) Dynamic and thermodynamic air-sea coupling associated with the Indian Ocean dipole diagnosed from 23 WCRP CMIP3 models. *J Clim*, doi: 10.1175/2011JCLI4041.1
- Luo J-J, Masson S, Roeckner E, Madec G, Yamagata T (2005) Reducing climatology bias in an ocean-atmosphere CGCM with improved coupling physics. *J Clim* 18:2344–2360
- Ma C-C, Mechoso CR, Robertson AW, Arakawa A (1996) Peruvian stratus clouds and tropical Pacific circulation a coupled ocean-atmosphere GCM study. *J Clim* 9:1635–1645
- Manganello JV, Huang B (2009) The influence of systematic errors in the Southeast Pacific on ENSO variability and prediction in a coupled GCM. *Clim Dyn* doi10.1007/s00382-008-0407-5

- McGregor S, Timmermann A, Schneider N, The effect of the South Pacific Convergence Zone on the termination of El Niño events and the meridional asymmetry of ENSO. Submitted to J Clim.
- McPhaden MJ, Lee L, McClurg D (2011) El Niño and its relationship to changing background conditions in the tropical Pacific Ocean. *Geophys Res Lett* 38, L15709, doi:10.1029/2011GL048275
- Mechoso CR, and Coauthors (1995) The seasonal cycle over the tropical Pacific in coupled ocean-atmosphere general circulation models. *Mon Wea Rev* 123:2825–2835
- Meehl GA, Gent PR, Arblaster JM, Otto-Bliesner BL, Brady EC, Craig A (2001) Factors that affect the amplitude of El Niño in global coupled climate models. *Clim Dyn* 17:515–526
- Meehl GA, Covey C, McAvaney B, Latif M, Stouffer RJ (2005) Overview of the Coupled Model Intercomparison Project. *Bull Amer Meteor Soc* 86:89–93
- Meinen CS, McPhaden MJ, Johnson GC (2001) Vertical velocities and transports in the Equatorial Pacific during 1993-99. *J Phys Oceanogr* 31:3230–3248
- Merryfield WJ (2006) Changes to ENSO under CO2 doubling in a multimodel ensemble. *J Clim* 19:4009–4027
- Michaelsen J (1987) Cross-validation in statistical climate forecast model. *J Appl Meteorol* 26:1589–1600, doi:10.1175/1520-0450
- Neale RB, Richter JH, Jochum M (2008) The impact of convection on ENSO: From a delayed oscillator to a series of events. *J Clim* 21:5904–5924
- Nitta T (1987) Convective activities in the tropical western Pacific and their impact on the Northern Hemisphere summer circulation. *J Meteor Soc Japan* 65:373–390

- Nordeng TE (1995) Extended versions of the convective parameterization scheme at ECMWF and their impact on the mean and transient activity of the model in the tropics
ECMWF Research Dept Tech Memo, 206, European Centre for Medium-Range Weather
Forecasts, Reading, United Kingdom, 41pp
- Ohlmann JC (2003) Ocean radiant heating in climate models. *J Clim* 16:1337–1351
- Philip SY, Van Oldenborgh GJ (2006) Shifts in ENSO coupling processes under global
warming. *Geophys Res Lett* 33:L11704. doi:10.1029/2006GL026196
- Randall DA, and Coauthors (2007) Climate models and their evaluation. *Climate Change
2007: The Physical Science Basis*, S Solomon et al, Eds, Cambridge University Press,
589–662
- Rayner NA et al. (2003) Global analyses of sea surface temperature, sea-ice and night
marine air temperature since the late nineteenth century. *J Geophys Res* 108,
doi:10.1029/2002JD002670
- Roeckner E, and coauthors (1996) The atmospheric general circulation model ECHAM-4:
Model description and simulation of present-day climate. Max-Planck-Institute for
Meteorology Rep 218, 90 pp
- Schneider, N., and P. Muller (1994) Sensitivity of the surface equatorial ocean to the
parameterization of vertical mixing. *J Phys Oceanogr* 24(7):1623–1640
- Smith RD, Dukowicz JK, Malone RC (1992) Parallel ocean general circulation modeling.
Physica D 60:38–61
- Smith TM, Reynolds RW, Peterson TC, Lawrimore J (2008) Improvements to NOAA's
Historical Merged Land-Ocean Surface Temperature Analysis (1880-2006), *J Clim*
21:2283–2293

- Soloman S. et al. (2010) Contributions of stratospheric water vapor to decadal changes in the rate of global warming. *Science* 327, 1219–1223
- Song X, Zhang GJ (2009) Convection parameterization, Tropical Pacific double ITCZ, and upper-ocean biases in the NCAR CCSM3. Part I: Climatology and atmospheric feedback. *J Clim* 22:4299–4315
- Spencer H, Sutton R, Slingo JM (2007) El Niño in a coupled climate model Sensitivity to changes in mean state induced by heat flux and wind stress corrections. *J Clim* 15:2273–2298
- Sperber KR, Annamalai H (2008) Coupled model simulations of boreal summer intraseasonal (30-50 day) variability, Part 1: systematic errors and caution on use of metrics. *Clim Dyn* 31:345–372.
- Suarez MJ, Schopf PS (1988) A delayed action oscillator for ENSO. *J Atmos Sci* 45:3283–3287
- Sui CH, Chung PH, Li T (2007) Interannual and interdecadal variability of the summertime western North Pacific subtropical high. *Geophys Res Lett* 34, doi:10.1029/2006GL029204
- Tao SY, Chen LX (1987) A review of recent research on the East Asian monsoon in China In: *Monsoon Meteorology*. Ed. By Chang C-P and Krishnamurti TN, Oxford University Press, London, 60–92
- Taylor KE, Williamson D, Zwiers F (2000) The sea surface temperature and sea-ice concentration boundary condition for AMIP II simulations, PCMDI Rep 60, Program for Climate Model Diagnosis and Intercomparison, Lawrence Livermore National Laboratory, Livermore, CA, 25 pp

- Terao T, Kubota T (2005) East-west SST contrast over the tropical oceans and the post El Niño western North Pacific summer monsoon. *Geophys Res Lett* 32 L15706, doi:10.1029/2005GL023010
- Tiedtke M (1989) A comprehensive mass flux scheme for cumulus parameterization in large-scale models. *Mon Wea Rev* 117:1779–1800
- Timmermann A et al. (2007) The influence of a weakening of the Atlantic Meridional Overturning Circulation on ENSO. *J Clim* 20:4899–4919
- Uppala SM, and Coauthors (2005) The ERA-40 Re-Analysis. *Quart J Roy Meteor Soc* 131:2961–3012
- Valcke S, Caubel A, Declat D, Terry L (2003) OASIS3 Ocean Atmosphere Sea Ice Soil user's guide Tech Rep TR/CMGC/ 03/69, CERFACS, Toulouse, France, 57 pp
- Vecchi GA, Soden BJ (2007) Global warming and the weakening of the tropical circulation. *J Clim* 20:4316–4340
- Vitart F, Balmaseda MA, Ferranti L, Anderson D (2003) Westerly wind events and the 1997/98 El Niño event in the ECMWF seasonal forecasting system: A case study. *J Clim* 16:3153–3170
- Wang B, Li T (1993) A simple tropical atmospheric model of relevance to short-term climate variation. *J Atmos Sci* 50:260–284
- Wang B (1995) Interdecadal changes in El Niño onset in the last four decades. *J Clim* 8:267–258
- Wang B, Xie X (1996) Low-Frequency Equatorial Waves in Vertically Sheared Zonal Flow. Part I: Stable waves. *J Atmos Sci* 53(3):449–467

- Wang B, Chan JCL (2002) How strong ENSO events affect tropical storm activity over the Western North Pacific. *J Clim* 15:1643–1658
- Wang B, Zhang Q (2002) Pacific-East Asian teleconnection, part II: How the Philippine Sea anticyclone established during development of El Niño. *J Clim* 15:3252–3265
- Wang B, Wu R, Fu X (2000) Pacific-East Asia teleconnection: How does ENSO affect East Asian climate? *J Clim* 13:1517–1536
- Wang B, An S-I (2001) Why the properties of El Niño changed during the late 1970s. *Geophys Res Lett* 28:3709–3712
- Wang B, Wu R, Lau KM (2001) Interannual variability of Asian summer monsoon: Contrast between the Indian and western North Pacific-East Asian monsoons. *J Clim* 14:4073–4090
- Wang B, Wu R, Li T (2003) Atmosphere-Warm Ocean interaction and its impact on Asia-Australian Monsoon variation. *J Clim* 16:1195–1211
- Wang B. et al. (2005) Fundamental challenges in simulation and prediction of summer monsoon rainfall. *Geophys Res Lett* 32, doi: 10.1029/2005GL022734
- Wang B. et al. (2008) How to measure the strength of the East Asian summer monsoon. *J Clim* 21:4449-4461
- Wang B et al. (2008) How accurately do coupled climate models predict the Asian-Australian monsoon interannual variability? *Clim Dyn* 30:605–619, doi:10.1007/s00382-007-0310-5 (2008)
- Wang B et al. (2009) Advance and prospectus of seasonal prediction: Assessment of APCC/CliPAS 14-model ensemble retrospective seasonal prediction (1980-2004). *Clim Dyn* 33:93-117

- Wang B, Xiang B, Pulse of the western North Pacific Subtropical High and associated Summer Monsoon and Tropical Storms. Submitted to Nature Geosci.
- Weng H, Ashok K, Behera WK, Rao SA, Yamagata T (2007) Impacts of recent El Niño Modoki on dry/wet conditions in the Pacific rim during boreal summer. *Clim Dyn* 29:113-129
- Weng H, Behera S, Yamagata T (2009) Anomalous winter climate conditions in the Pacific Rim during recent El Niño Modoki and El Niño events. *Clim Dyn* 32:663–674, doi:10.1007/s00382-008-0394-6
- Wittenberg AT, Rosati A, Lau N-C, Ploshay JJ (2006) GFDL’s CM2 Global Coupled Climate Models Part III Tropical Pacific Climate and ENSO. *J Clim* 19:698–722
- Wu B, Li T, Zhou T (2010) Relative contributions of the Indian Ocean and local SST anomalies to the maintenance of the western North Pacific anomalous anticyclone during El Niño decaying summer. *J Clim* 23:2974–2986, doi:10.1175/2010JCLI3300.1
- Wu G, Liu H (1995) Neighbourhood Response of Rainfall to Tropical Sea Surface Temperature Anomalies Part I: Numerical Experiment. *Scientia Atmospherica Sinica* 19 (4):422–434
- Wu L, He F, Liu Z (2005) Coupled ocean-atmosphere response to north tropical Atlantic SST: Tropical Atlantic dipole and ENSO. *Geophys Res Lett* 32:L21712, doi:10.1029/2005GL024222
- Wu Z, Wang B, Li J, Jin F-F (2009) An empirical seasonal prediction model of the East Asian summer monsoon using ENSO and NAO. *J Geophys Res* 114, doi:10.1029/2009JD011733

- Xiang B, Yu W, Li T, Wang B (2011) The critical role of the boreal summer mean state in the development of the IOD. *Geophys Res Lett* 38:L02710. doi:10.1029/2010GL045851
- Xie S-P et al. (2009) Indian Ocean capacitor effect on Indo-western Pacific climate during the summer following El Niño. *J Clim* 22:730–747
- Xie S-P, Okumura Y, Miyama T, Timmermann A (2008) Influences of Atlantic climate change on the tropical Pacific via the central American Isthmus. *J Clim* 21:3914–3928
- Yang J, Liu Q, Xie S-P, Liu Z, Wu L (2007) Impact of the Indian Ocean SST basin mode on the Asian summer monsoon. *Geophys Res Lett* 34:L02708, doi: 10.1029/2006GL028571
- Ye DZ, Huang RH (1996) On variations of droughts and floods in Reaches of Yangtze and Yellow Rivers. Academic Press of Shandong, Jinan 222–236 (in Chinese)
- Yeager SG, Shields CA, Large WG, Hack JJ (2006) The low-resolution CCSM3. *J Clim* 19:2545–2566
- Yeh S-W, Kug J-S, Dewitte B, Kwon M-H, Kirtman B, Jin F-F (2009) El Niño in a changing climate. *Nature* 461:511–514, doi:10.1038/nature08316
- Yu L, and Weller RA (2007) Objectively Analyzed air-sea heat Fluxes for the global ice-free oceans (1981–2005). *Bull Ameri Meteor Soc* 88:527–539
- Zavala-Garay J, Moore AM, Perez CL, Kleman R (2003) The response of a coupled model of ENSO to observed estimates of stochastic forcing. *J Clim* 16:2827–2842
- Zebiak SE (1986) Atmospheric convergence feedback in a simple model for El Niño. *Mon Wea Rev* 114:1263–1271
- Zebiak SE, Cane MA (1987) A Model El-Niño Southern Oscillation. *Mon Wea Rev* 115:2262–2278

Zhang R, Sumi A, Kimoto M (1996) Impact of El Nino on the East Asia Monsoon: A diagnostic study of the '86/87 and '91/92 events. *J Meteor Soc Japan* 74: 49–62

Zhang R, Delworth T L (2007) Impact of the Atlantic Multidecadal Oscillation on North Pacific climate variability. *Geophys Res Lett* 34:L23708, doi:10.1029/2007/GL031601

Zhang Y, Rossow WB, Lacis AA, Oinas V, Mishchenko MI (2004) Calculation of radiative fluxes from the surface to top of atmosphere based on ISCCP and other global data sets: Refinements of the radiative transfer model and the input data. *J Geophys Res* 109:D19105, doi:10.1029/2003JD004457

APPENDIX: FIGURES

Chapter 1

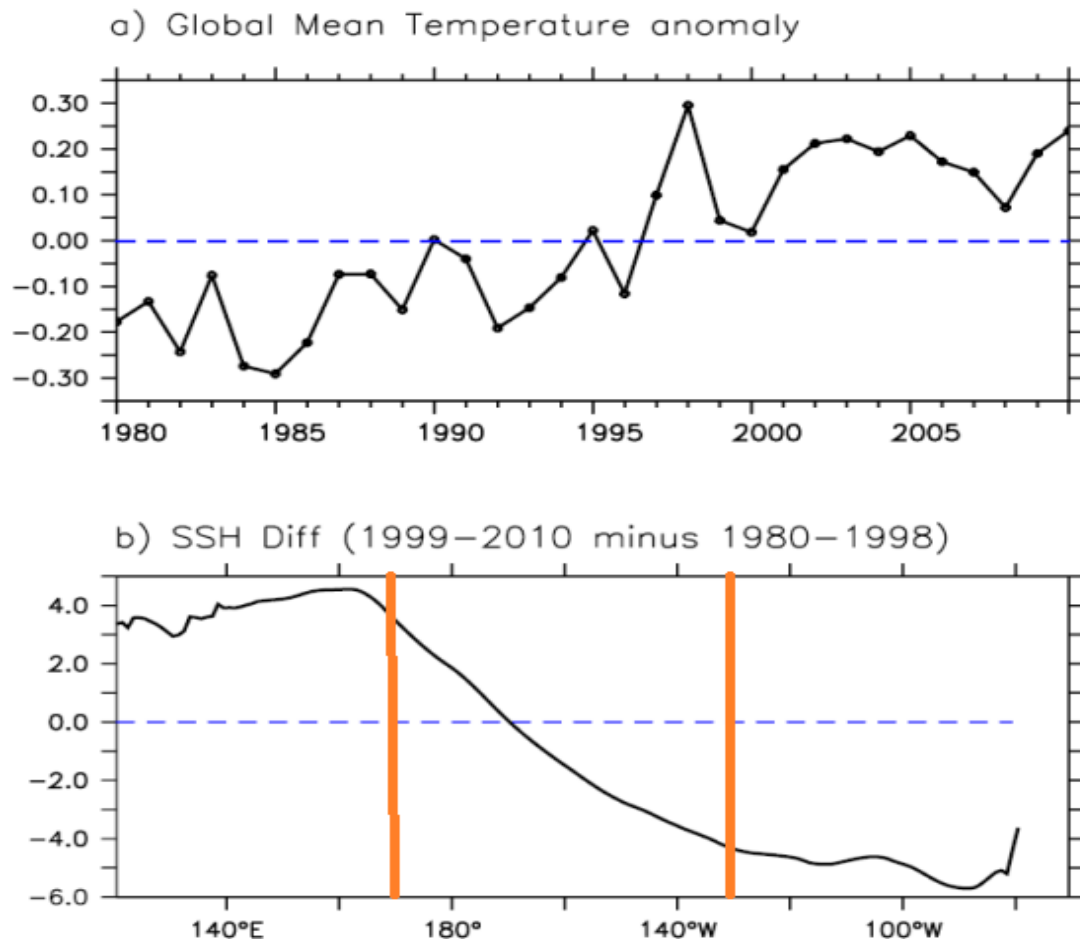


Figure 1.1 a) Global mean temperature anomalies ($^{\circ}\text{C}$) derived from HadCRUT3 [Brohan *et al.*, 2006]. b) Equatorial (2°S - 2°N) SSH difference (cm) between the two epochs, 1999-2010 minus 1980-1998. Here the change of SSH signifies the change in thermocline depth. The orange lines mark the edge of the central Pacific where the maximum SST warming occurs but the thermocline depth becomes even deeper after the late 1990s.

Model Development

POEM (POP-OASIS-ECHAM Model)

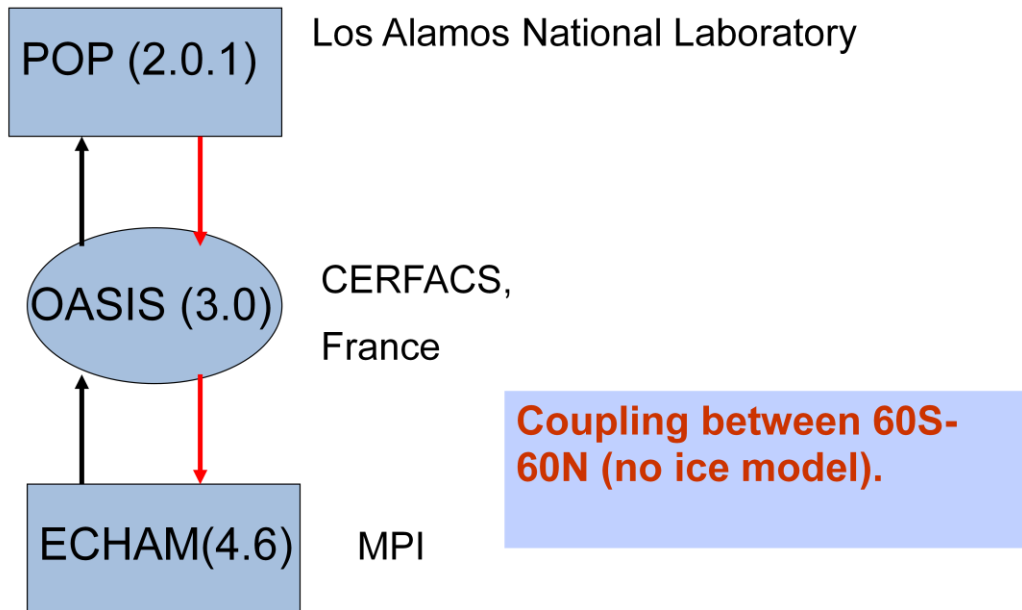


Figure 2.1 Component of the coupled model POEM.

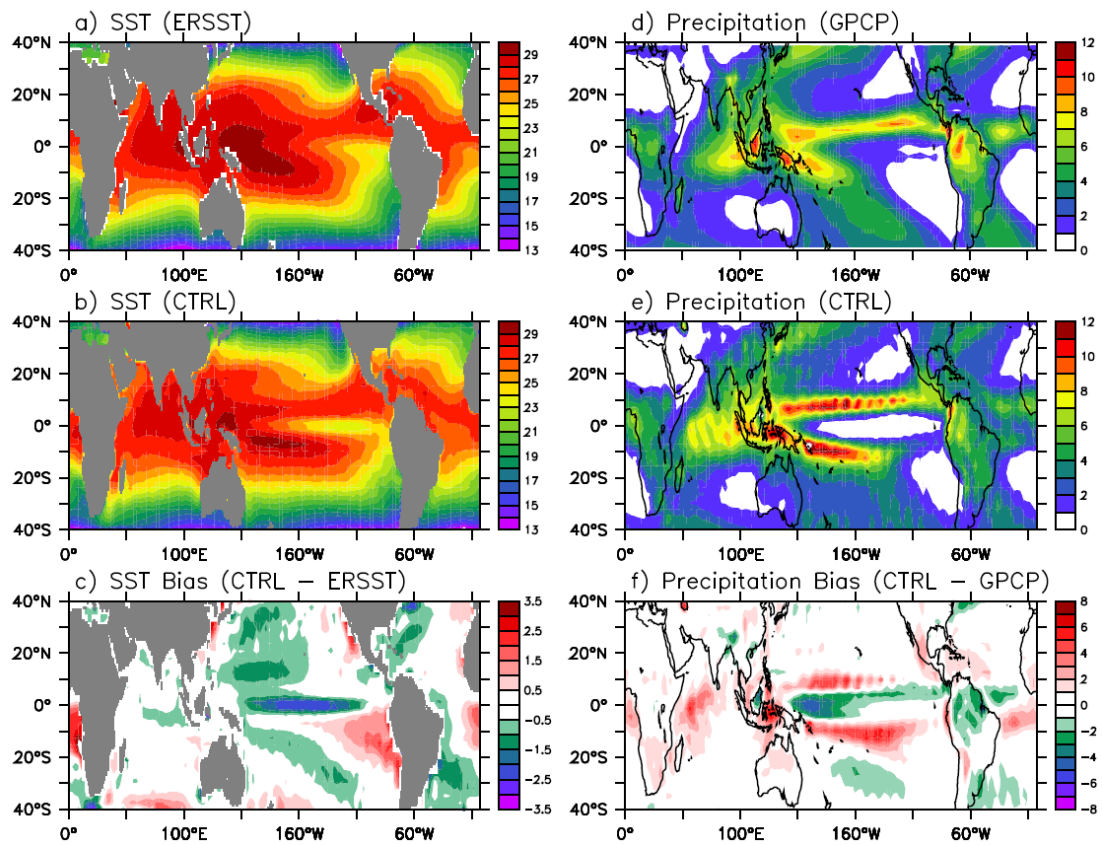


Figure 2.2 Left panel: Time-mean SST (°C) from a) ERSST, b) CTRL, and c) CTRL-ERSST difference. Right panel: Time-mean precipitation (mm day⁻¹) from d) GPCP, e) CTRL, and f) CTRL-GPCP difference.

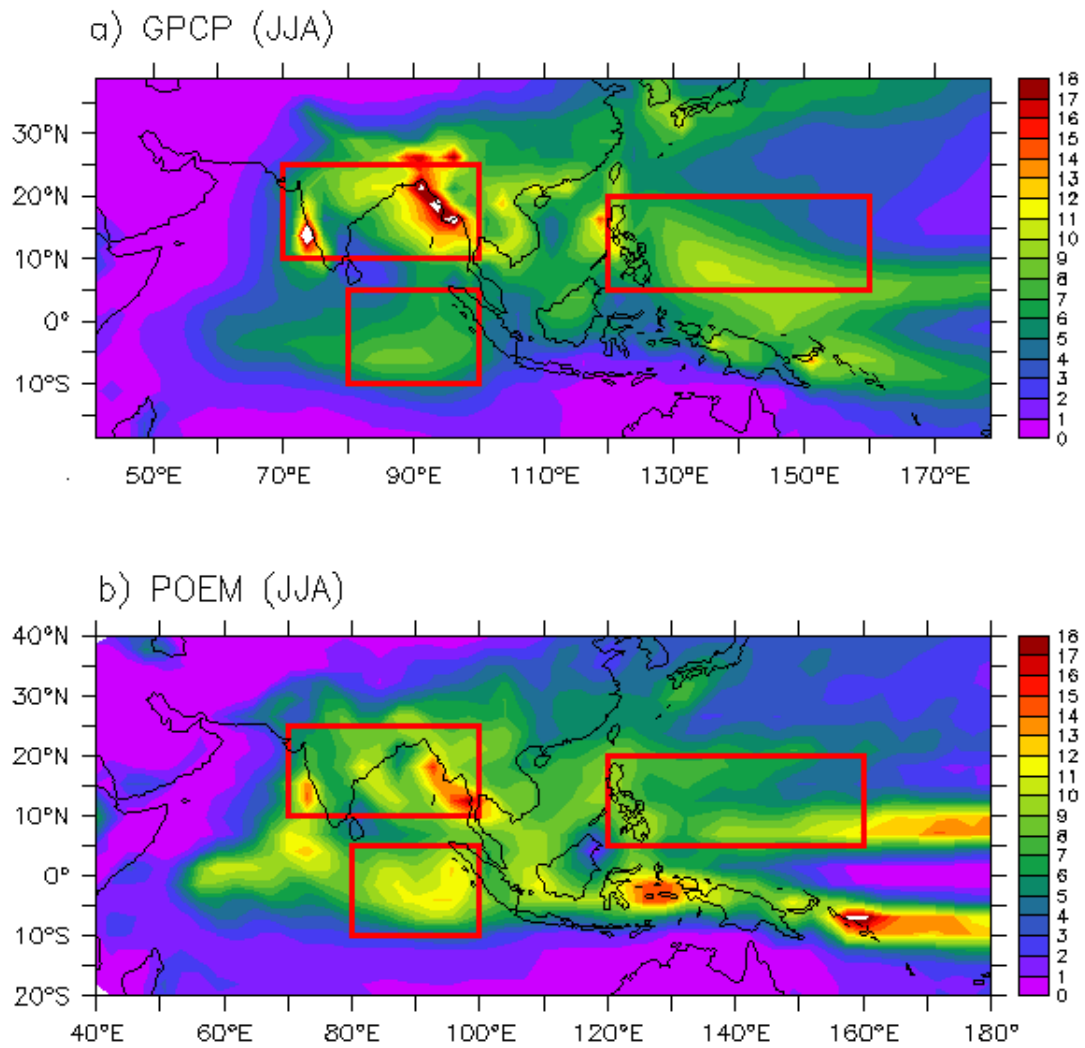


Figure 2.3 Boreal summer (JJA) mean precipitation (mm day^{-1}) from a) GPCP, b) POEM. The red boxes represent three major monsoon systems, the Indian Summer monsoon, the equatorial eastern Indian Ocean, the western North Pacific monsoon.

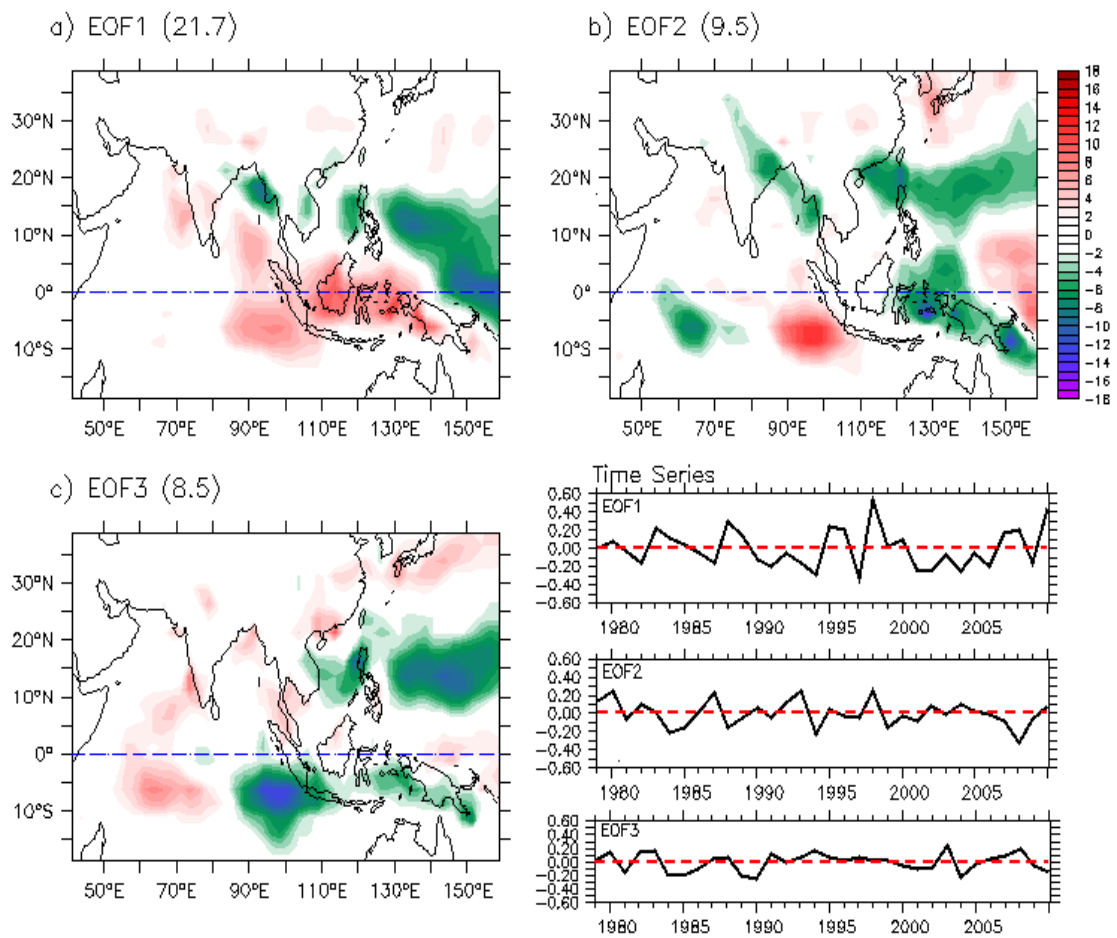


Figure 2.4 The first 3 leading EOF modes of boreal summer (JJA) precipitation from GPCP. a), b), c) are the corresponding spatial pattern of these three modes. The time series are shown in the lower right panel.

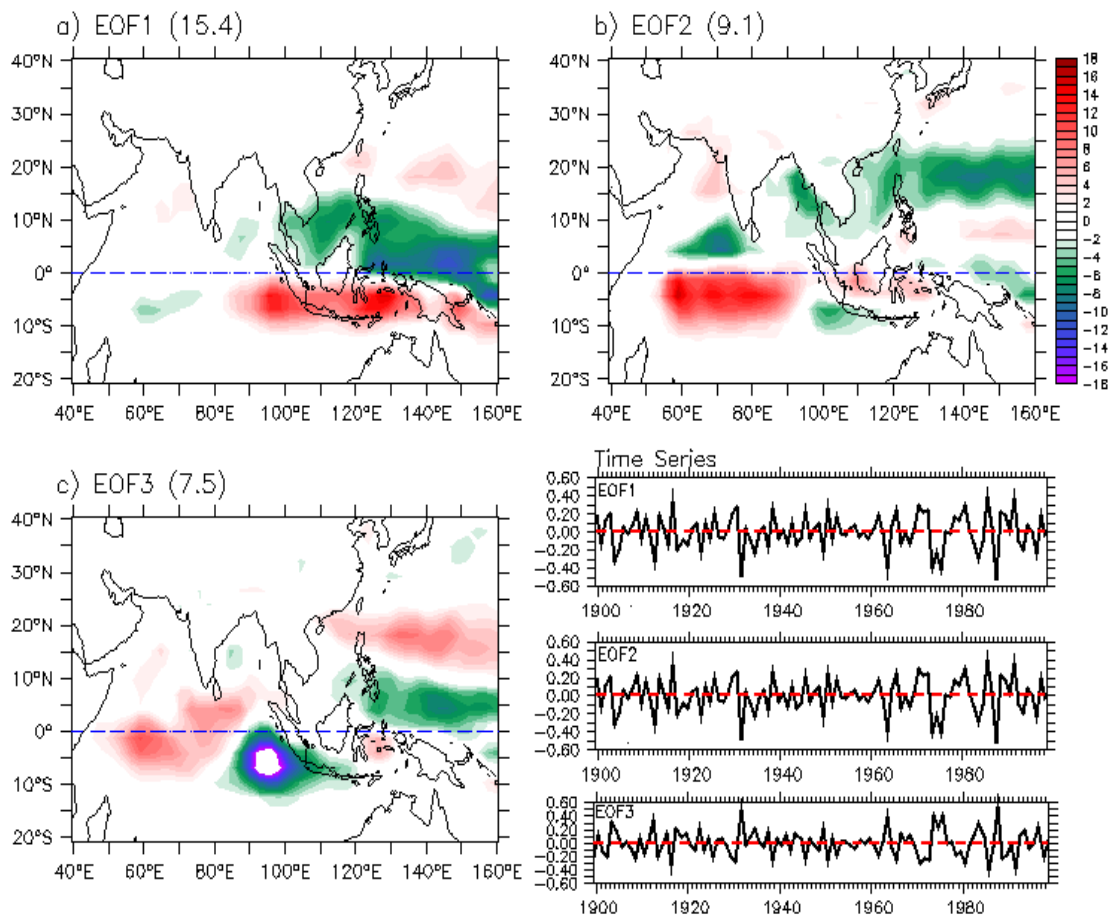


Figure 2.5 Same as Fig. 2.4 but from POEM.

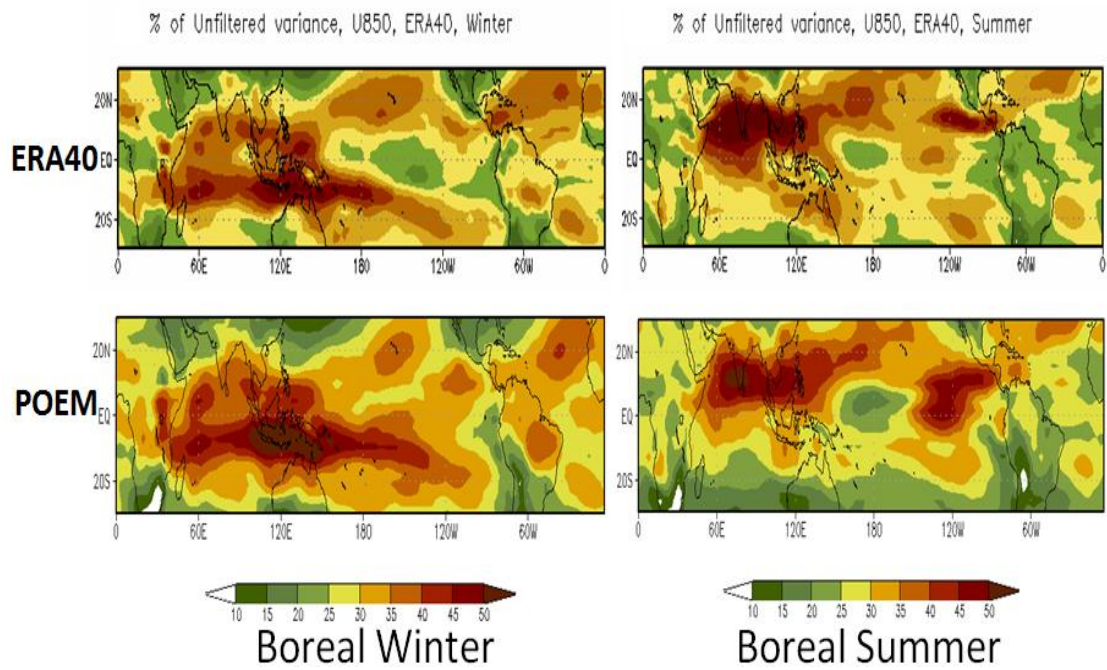


Figure 2.6 Percentage of the variance of 20-100 day bandpass filtered zonal wind (850 hPa) to the total variance from ERA40 (upper panel) and POEM (lower panel). The left panel is for boreal winter (Nov-Apr) and the right panel is for boreal summer (May-Oct).

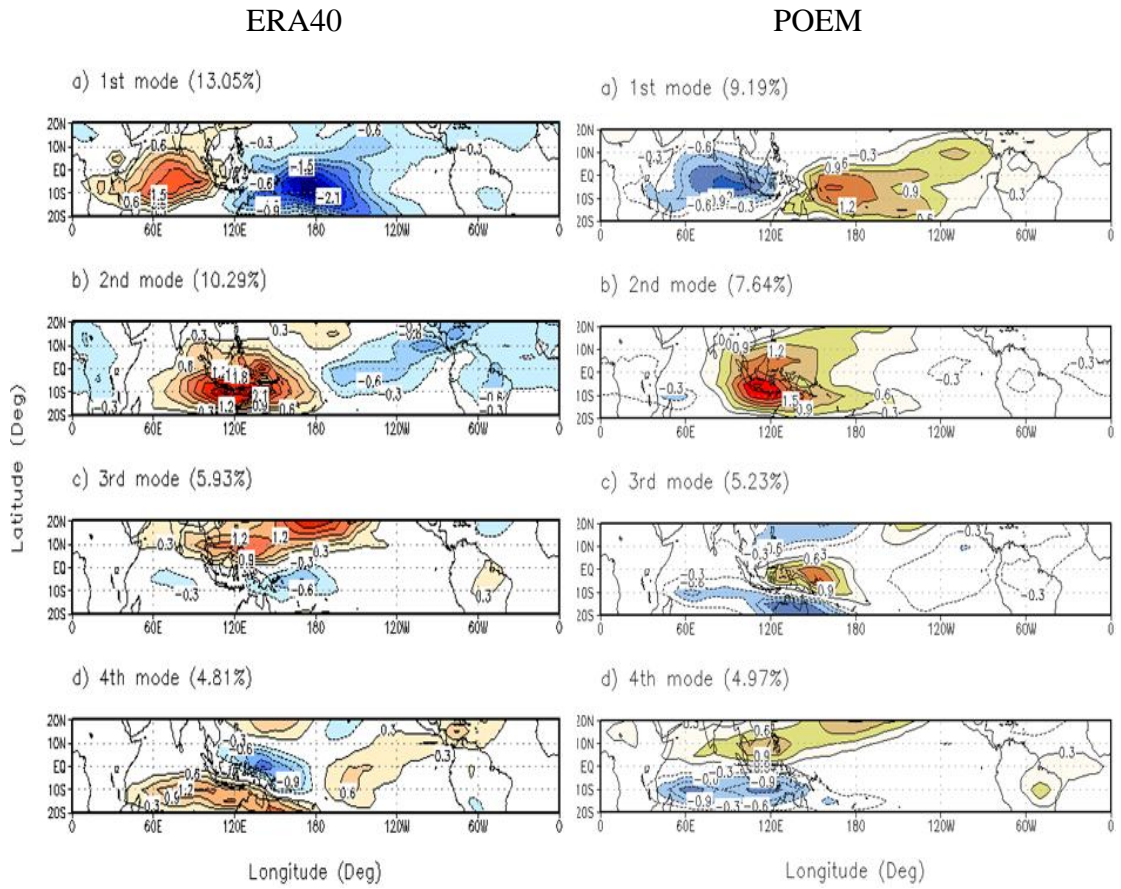


Figure 2.7 The first four leading EOF modes of 850 hPa zonal wind with 20-100 bandpass filtering during boreal winter. The left panel is from ERA40 and the right is from POEM.

ERA40

POEM

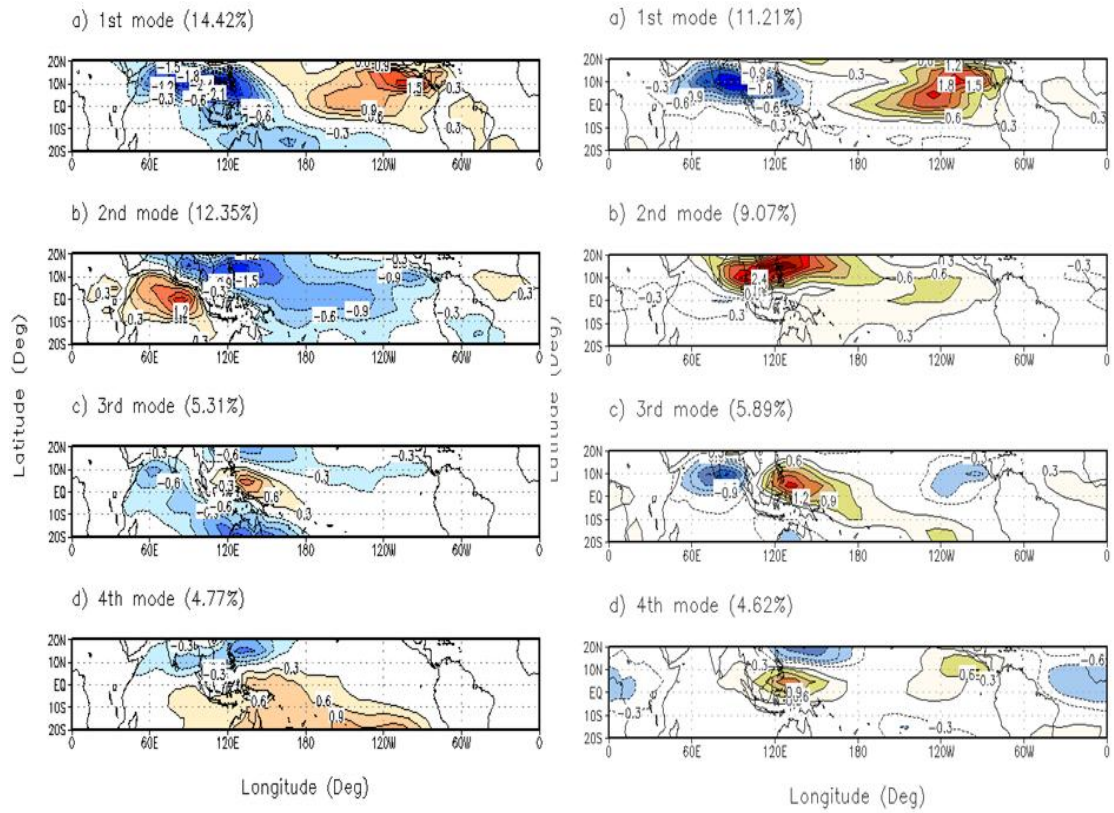


Figure 2.8 The same as 2.7 but for boreal summer season.

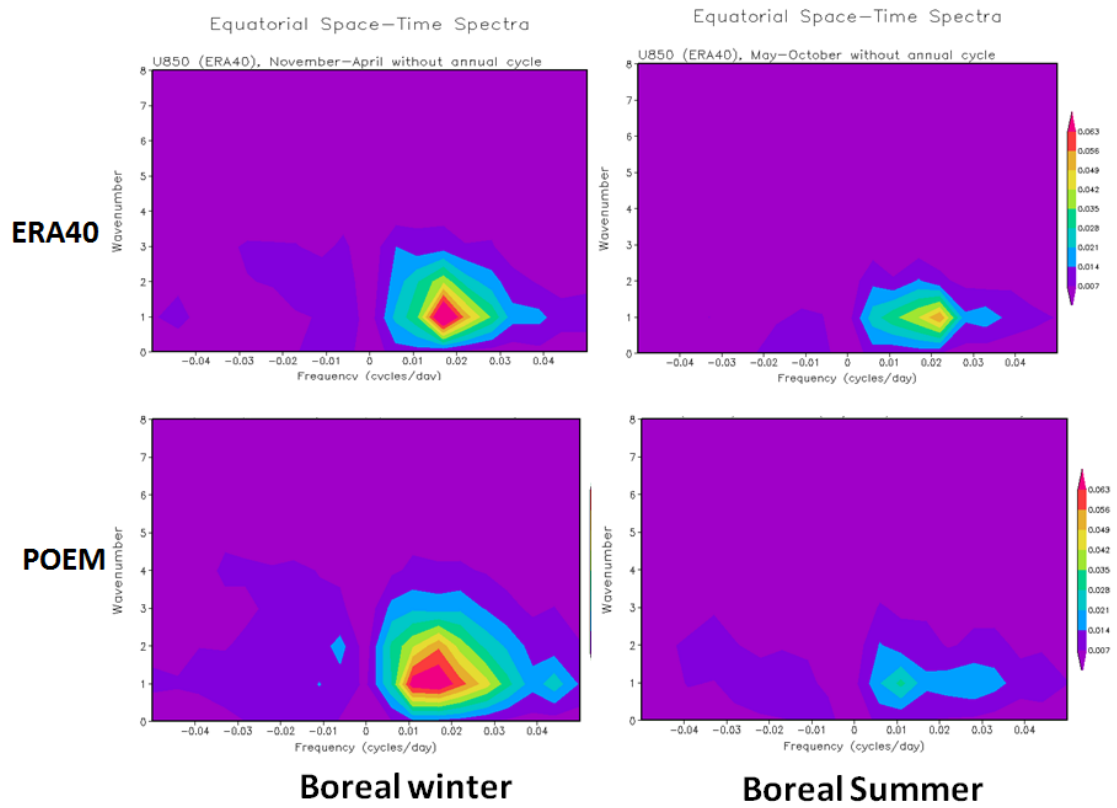


Figure 2.9 Wavenumber-frequency spectra of 10N-10N averaged 850 hPa zonal wind ($\text{m}^2 \text{s}^{-2}$) for the ERA40 (upper panel) and POEM (lower panel). The left panel is for boreal winter season and the right panel is for boreal summer season.

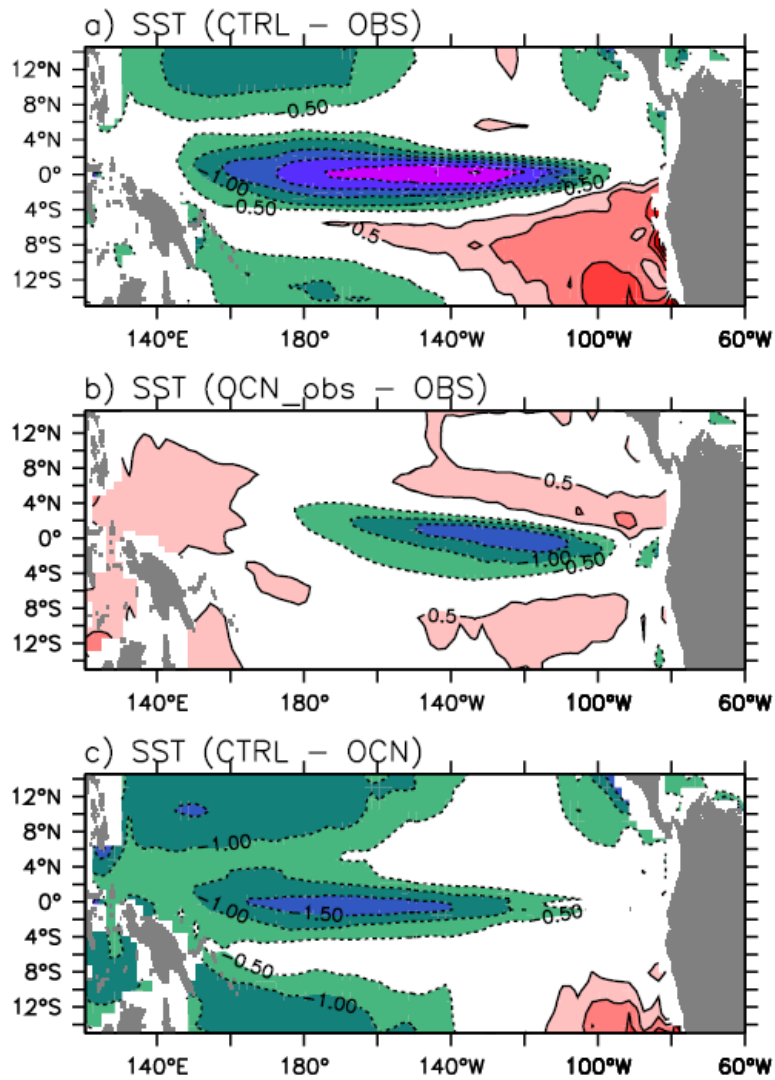


Figure 2.10 a) time-mean SST difference ($^{\circ}\text{C}$) between a) CTRL and observations, b) OCN_obs and observations, c) CTRL and OCN.

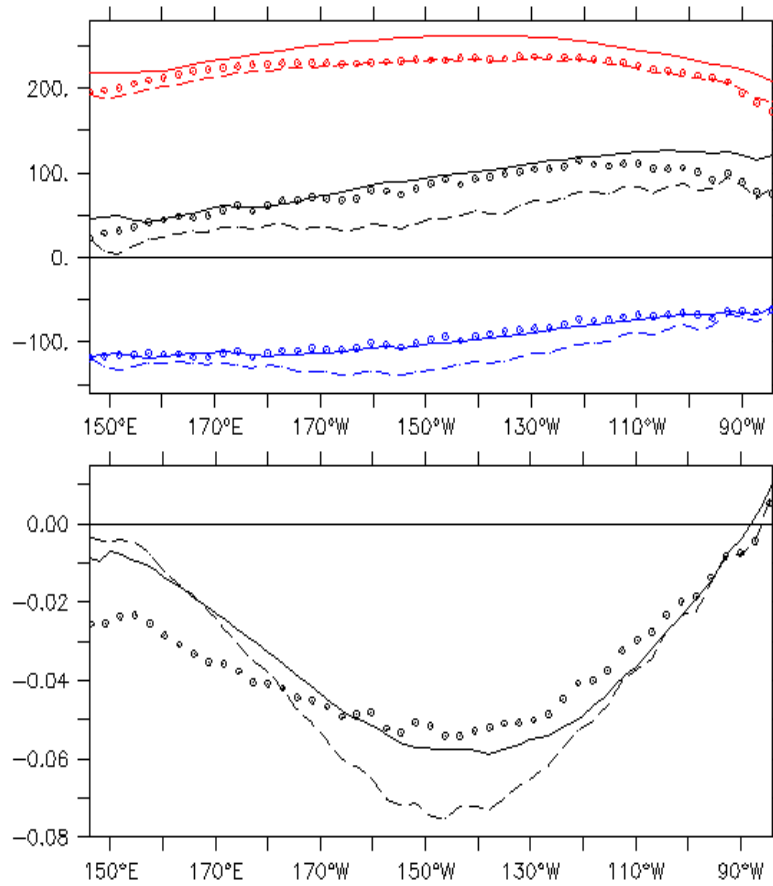


Figure 2.11 Equatorial (5°S - 5°N) heat flux (upper panel in W m^{-2}) and surface wind stress (lower panel in N m^{-2}) from observations (solid), AMIP (dashed) and CTRL (circle). In the upper panel, red line/circle represents the shortwave radiation and blue line/circle denotes the latent heat flux. The corresponding black line/circle shows the net heat flux.

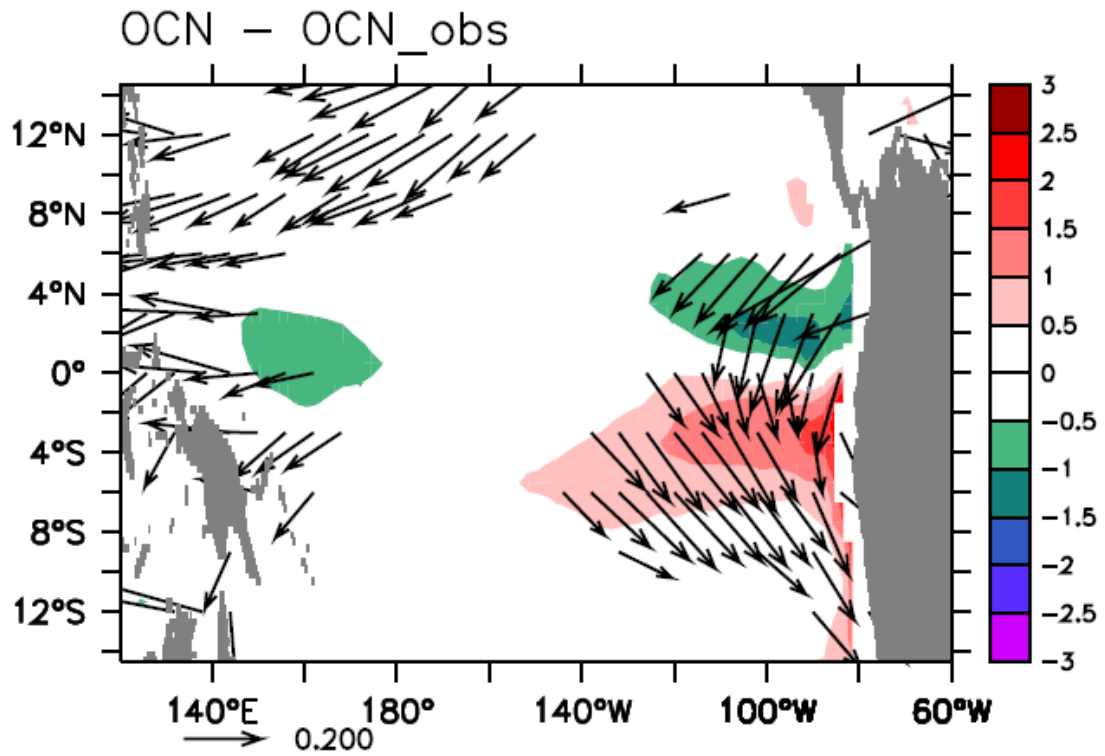


Figure 2.12 Time mean SST difference between OCN and OCN_obs experiments. Surface wind stress difference is shown as vectors (only shown when magnitude greater than 0.15 dyn cm^{-2}).

Chapter 3

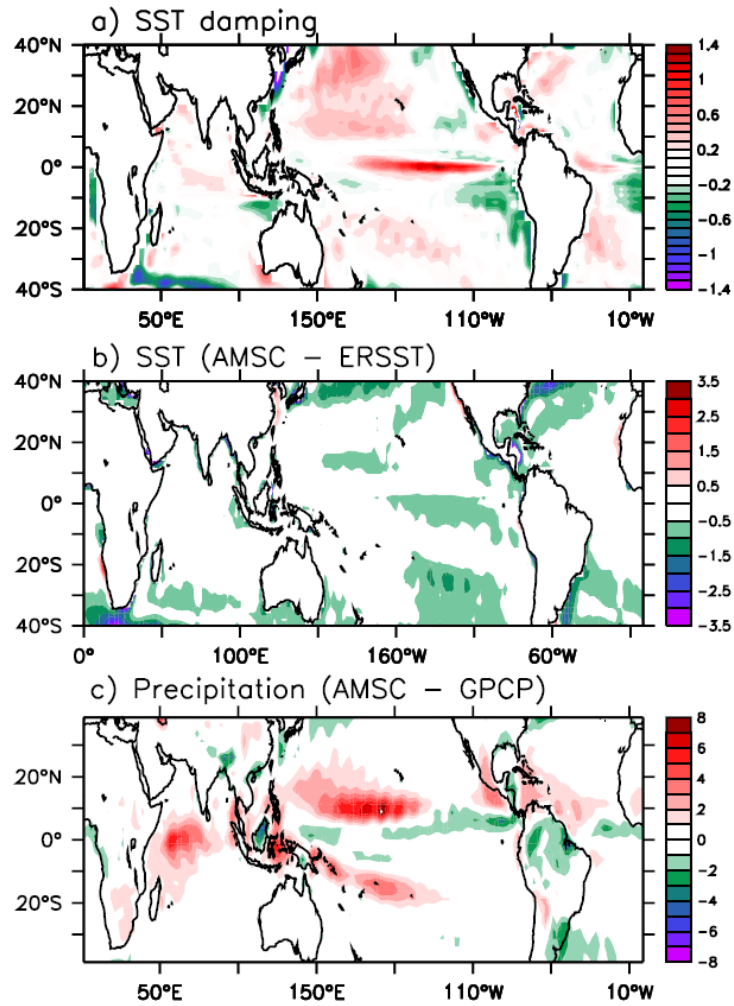


Figure 3.1 a) Horizontal map of the annual mean SST correction term (units: $^{\circ}\text{C}$ per 5 days), time-mean b) SST bias (AMSC-ERSST) and c) precipitation bias (AMSC-GPCP) for the AMSC run.

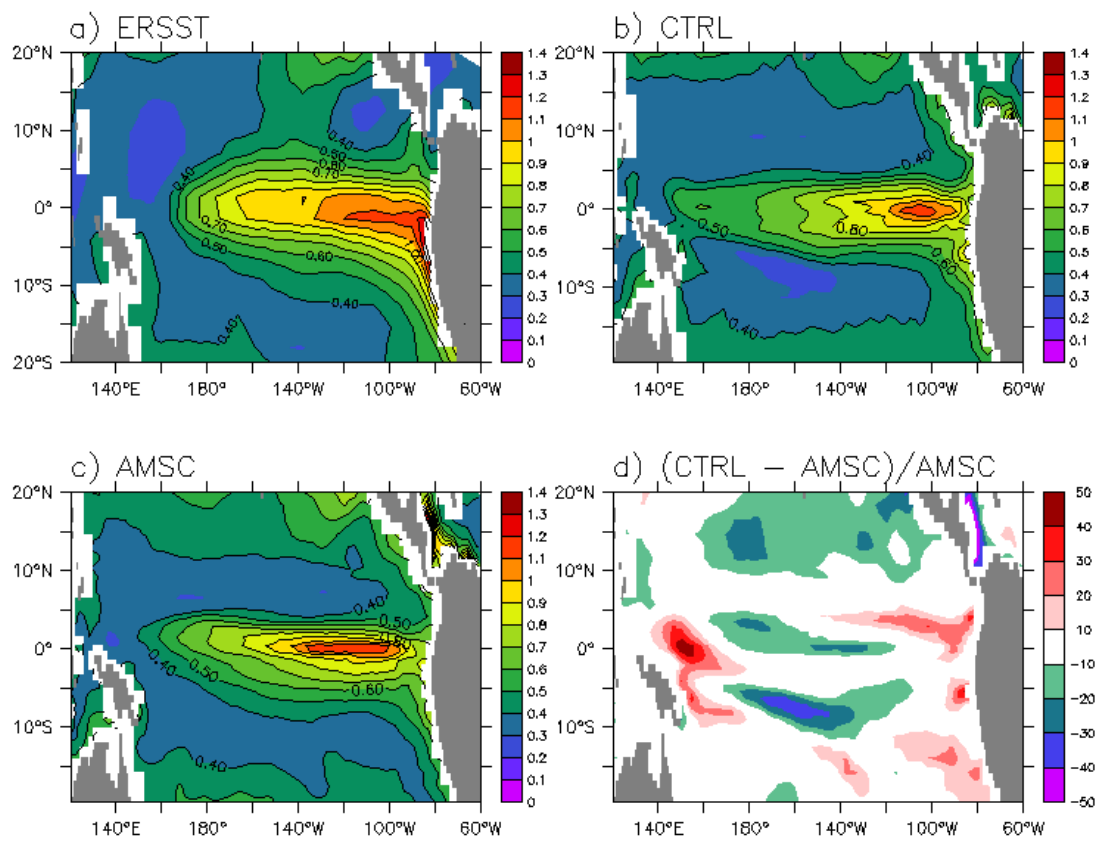


Figure 3.2 Standard deviations of SSTA (°C) from a) ERSST, b) CTRL, c) AMSC, d) the ratio of CTRL-AMSC and AMSC (percent).

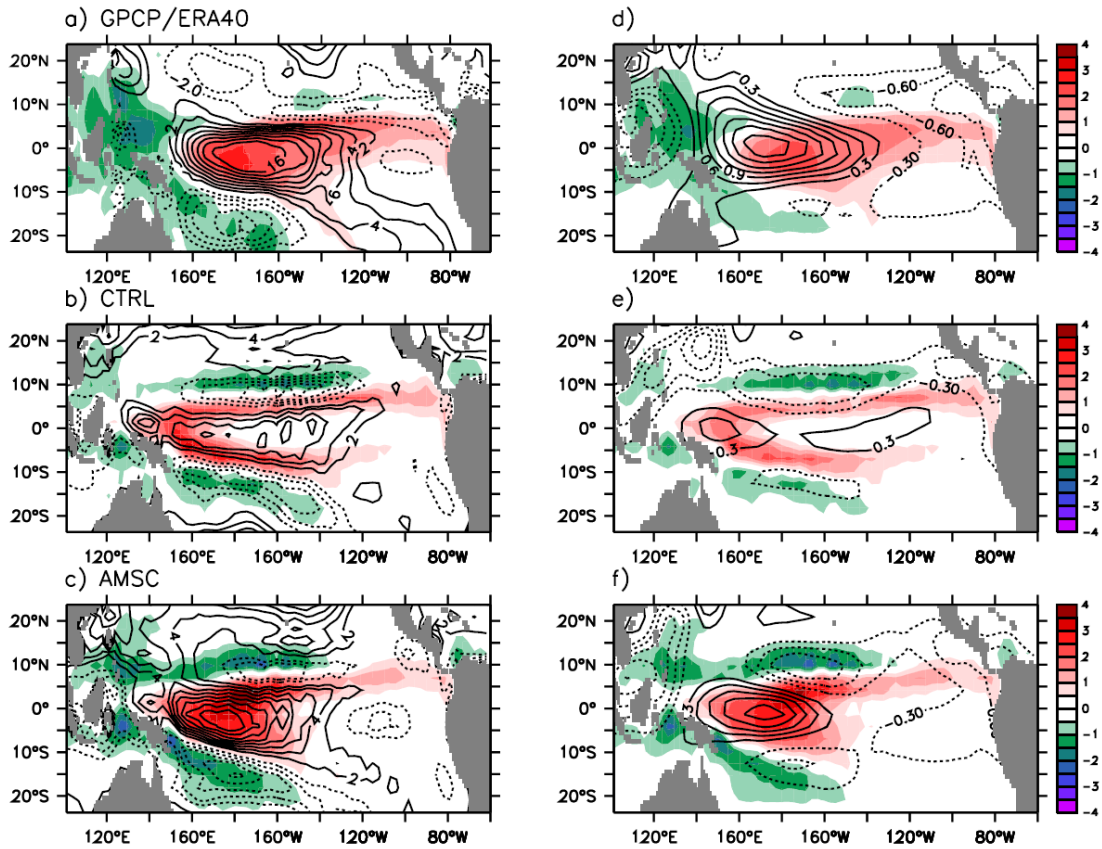


Figure 3.3 Precipitation (shading in $\text{mm day}^{-1} \text{ }^{\circ}\text{C}^{-1}$) and surface zonal wind stress (contours in $10^{-3} \text{ Nm}^{-2} \text{ }^{\circ}\text{C}^{-1}$) anomaly regressed onto Niño-3 index from a) GPCP/ERA40, b) CTRL, and c) AMSC. By using a dry AGCM, the right panel (d-f) shows the low level wind response (contours in m s^{-1}) to the prescribed mid-tropospheric forcing with the same regressed precipitation pattern from the left panel.

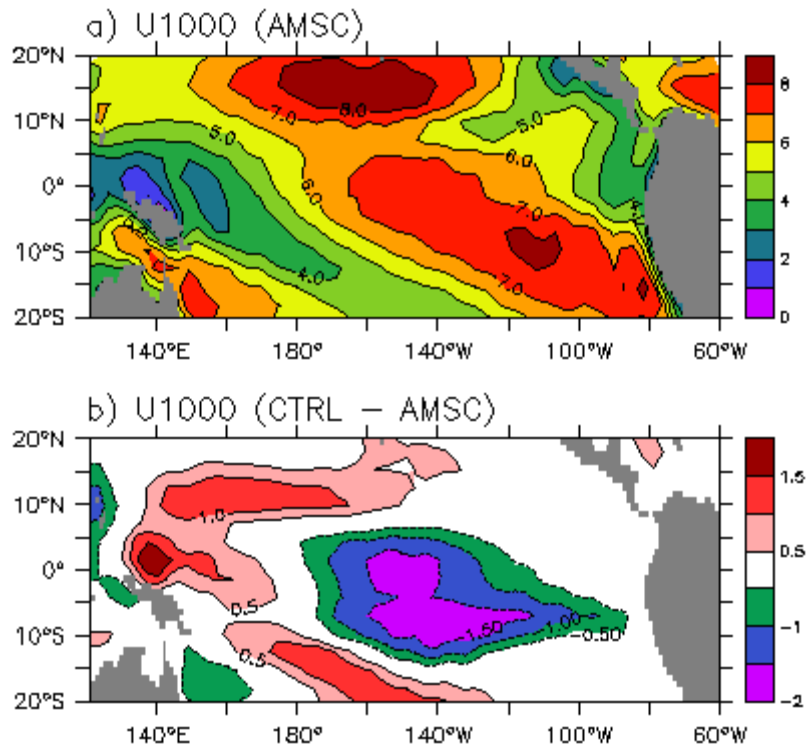


Figure 3.4 a) Time-mean 1000 hPa wind speed (m s^{-1}) for AMSC, b) Time-mean 1000 hPa wind speed difference between CTRL and AMSC.

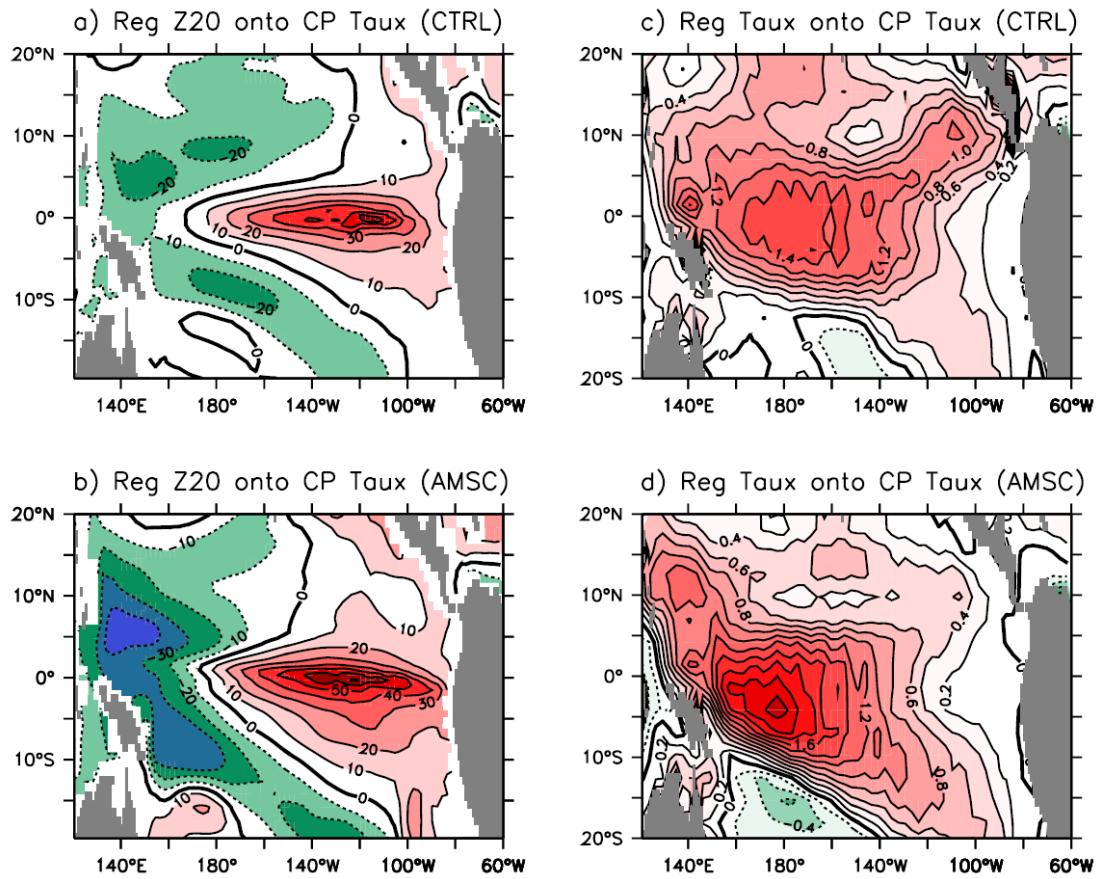


Figure 3.5 Thermocline depth (Z20) anomaly regressed onto equatorial zonal wind stress anomaly averaged over 160°E-130°W, 5°S-5°N (in $\text{m cm}^2 \text{dyn}^{-1}$) for the a) CTRL, b) AMSC. Zonal wind stress anomaly regressed onto equatorial zonal wind stress anomaly averaged over 160°E-130°W, 5°S-5°N for the c) CTRL, d) AMSC.

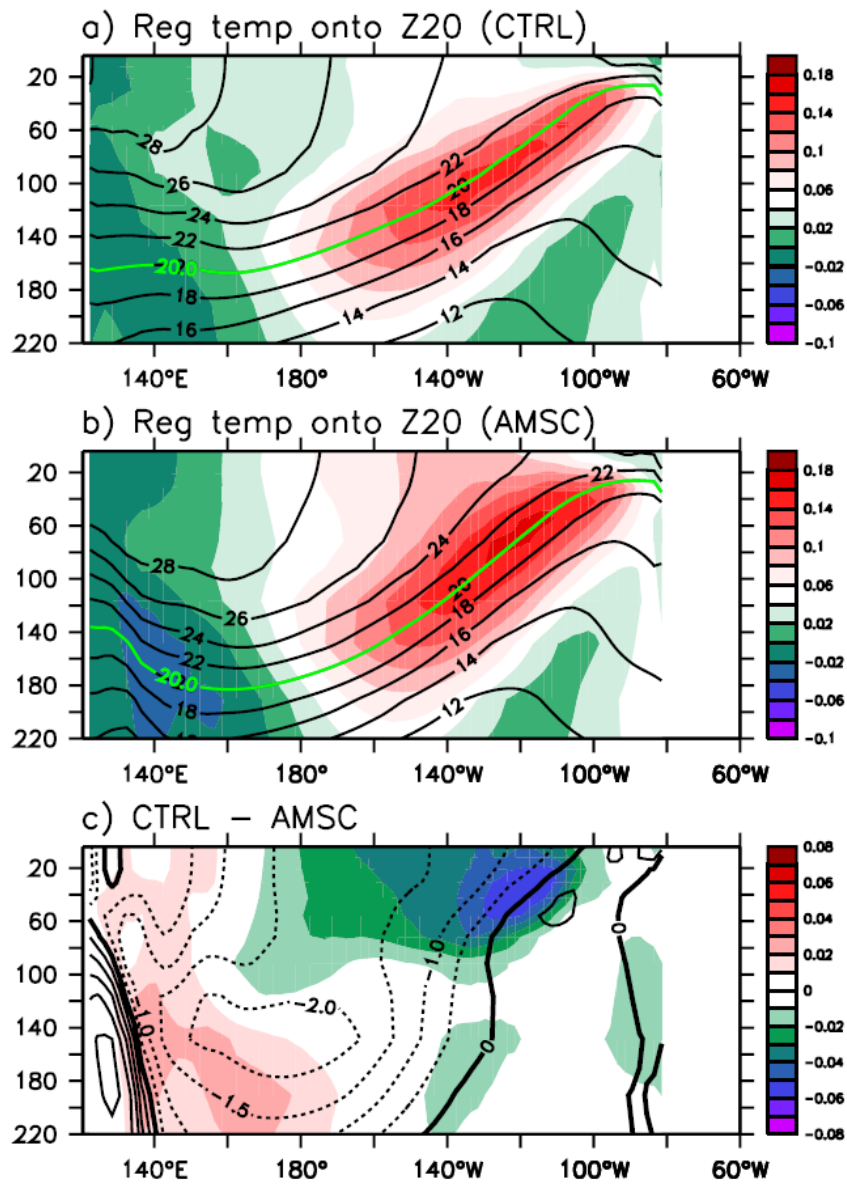


Figure 3.6 Equatorial (2°S - 2°N) temperature anomaly (shading in $^{\circ}\text{C m}^{-1}$) regressed onto equatorial thermocline depth anomaly averaged over 180° - 80°W , 2°S - 2°N for the a) CTRL, b) AMSC, c) CTRL-AMSC. Contours in the a), b) are the corresponding climatological temperature. Contours in c) is the climatological temperature difference between the CTRL and AMSC.

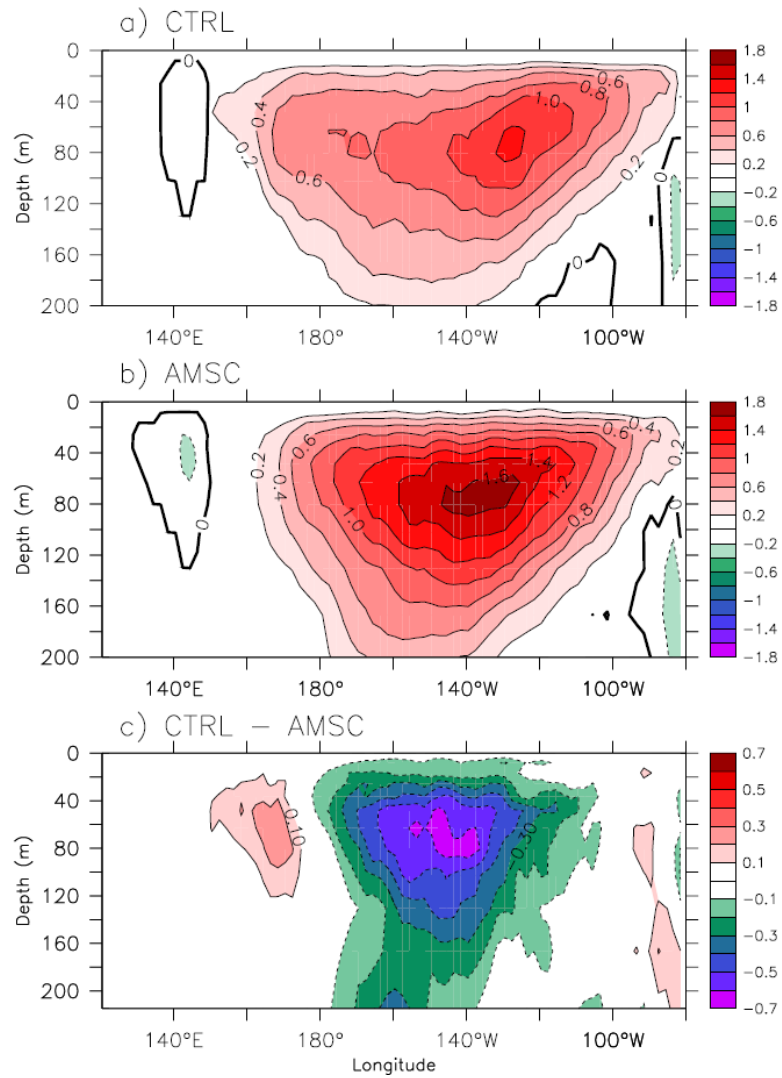


Figure 3.7 Time-mean equatorial (2°S - 2°N) upwelling (shading in m day^{-1}) from a) CTRL, b) AMSC, and c) CTRL-AMSC difference.

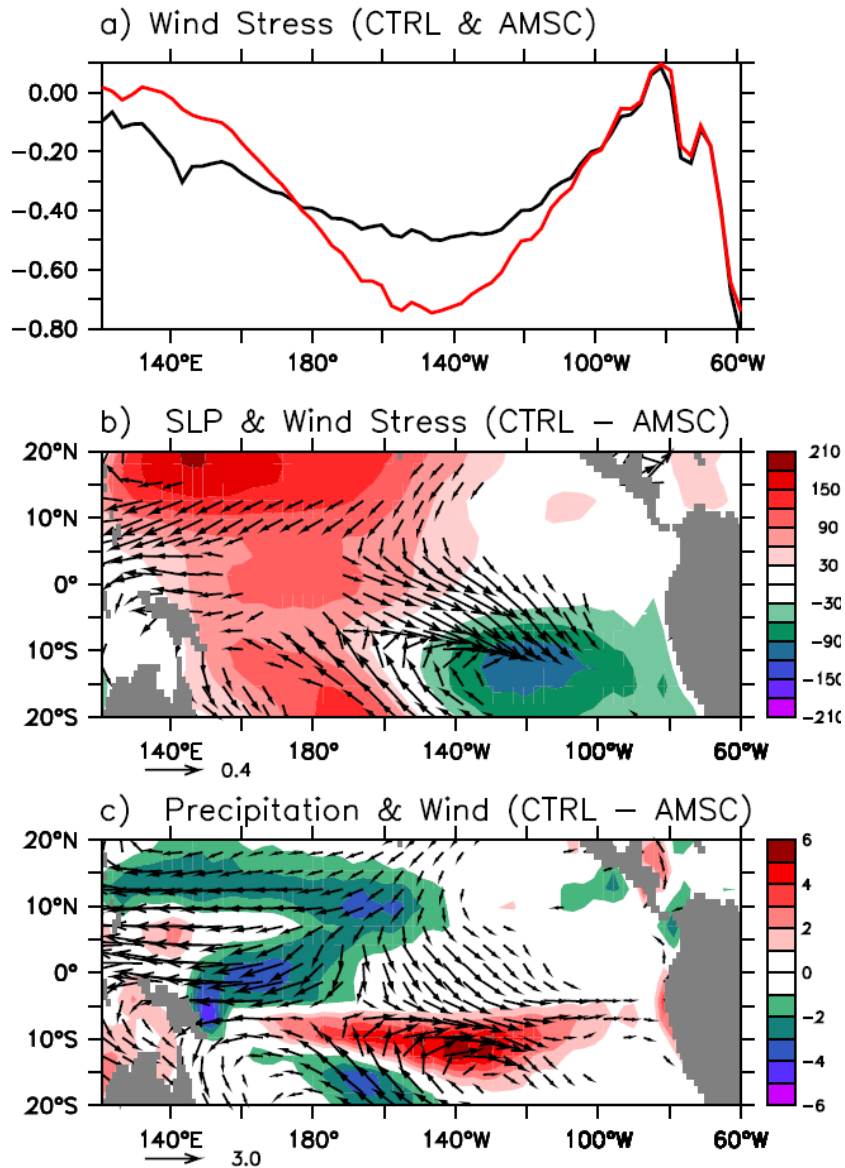


Figure 3.8 a) Time-mean equatorial (5°S-5°N) zonal wind stress (dyn cm⁻²) from the CTRL (black) and AMSC (red). b) Time-mean differences between CTRL and AMSC of SLP (shading in Pa) and surface wind stress (vectors with magnitude greater than 0.1 dyn cm⁻²), c) same as b) but for precipitation (shading in mm day⁻¹) and 850 hPa wind (vectors with magnitude greater than 0.4 m s⁻¹).

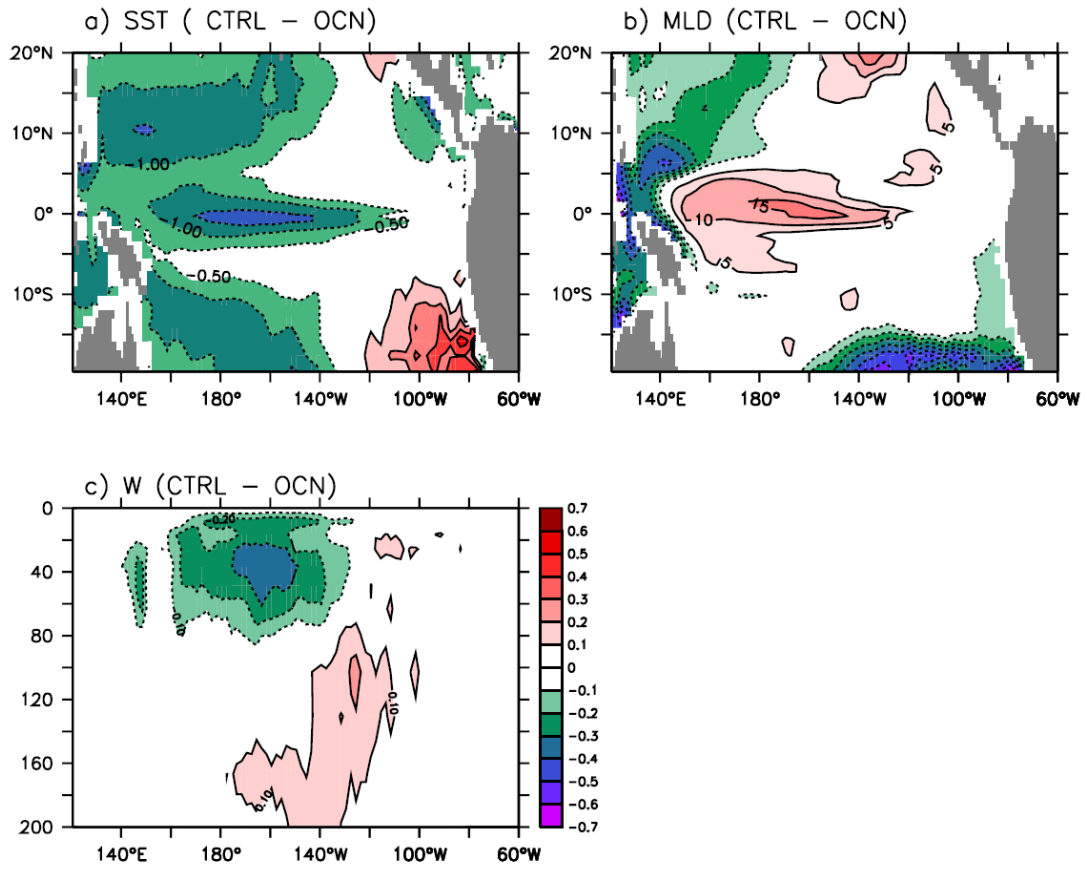


Figure 3.9 a) Time-mean difference of a) SST ($^{\circ}\text{C}$), b) mixed layer depth (m), and c) equatorial (2°S - 2°N) mean upwelling (m day^{-1}) differences between CTRL and OCN.

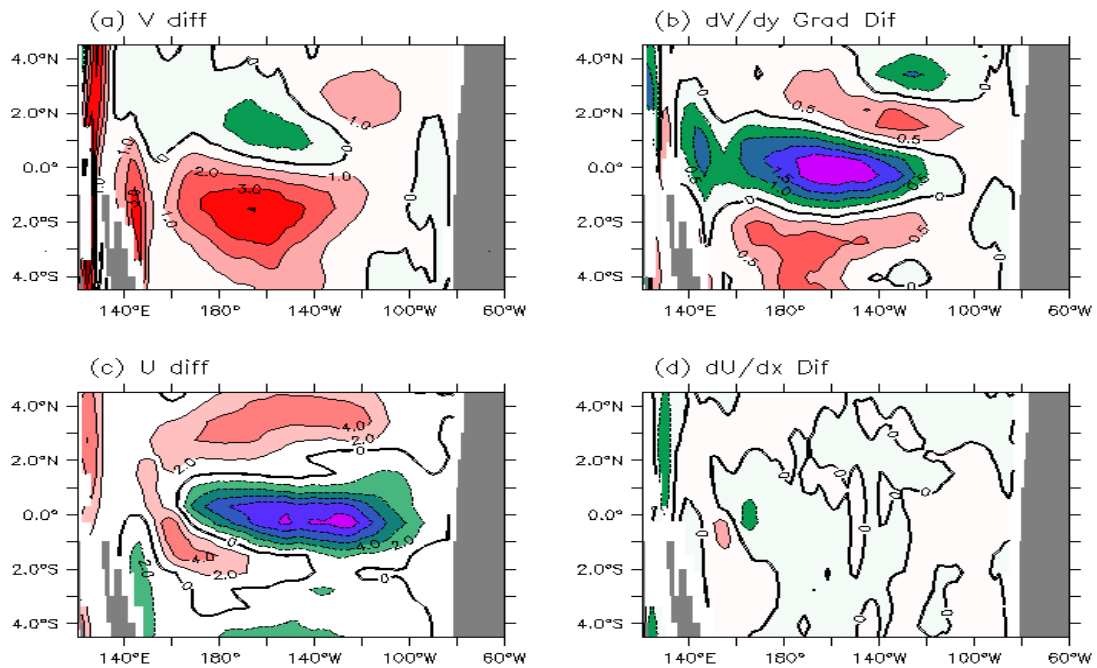


Figure 3.10 a), c) the meridional and zonal currents (cm s^{-1}) differences between CTRL and OCN averaged over the upper 30 m. b), d) are the corresponding meridional gradient of meridional currents and zonal gradient of zonal currents ($\times 10^{-7} \text{s}^{-1}$).

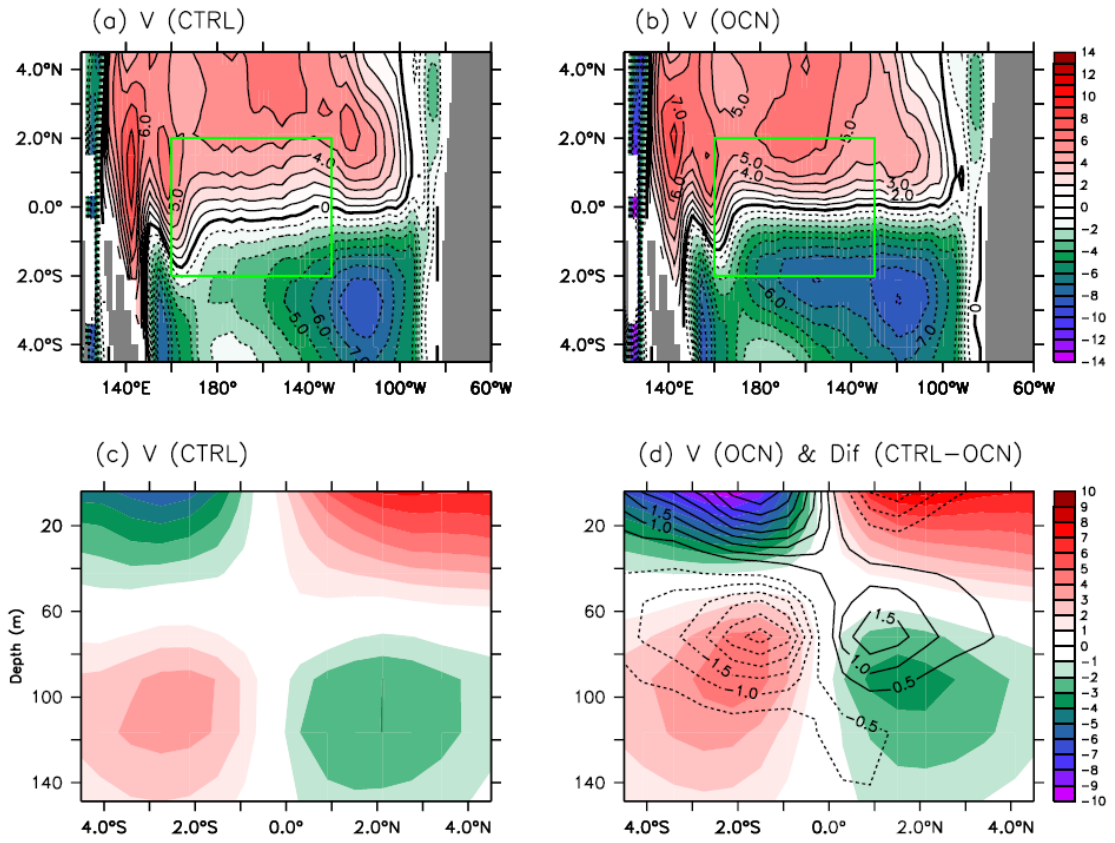


Figure 3.11 Time-mean meridional currents (cm s^{-1}) averaged over the upper 30 m from a) CTRL, b) OCN. Vertical-Longitudinal diagram of time-mean meridional currents from c) CTRL, d) OCN. Contours in d) indicates the corresponding meridional currents difference between CTRL and OCN.

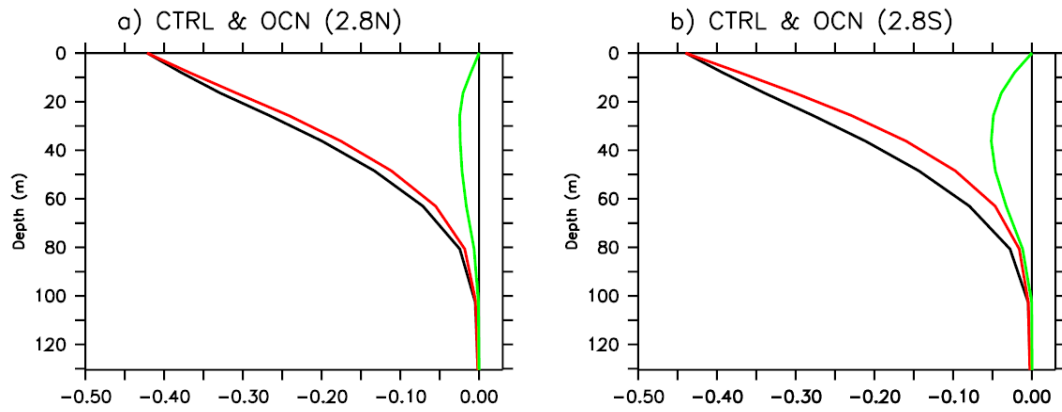


Figure 3.12 Time-mean horizontal viscous stress ($\text{cm}^2 \text{s}^{-2}$) along a) 2.8 N and b) 2.8 S . The black and red lines indicate the results from the CTRL and OCN experiments, respectively. The green line shows the difference between CTRL and OCN.

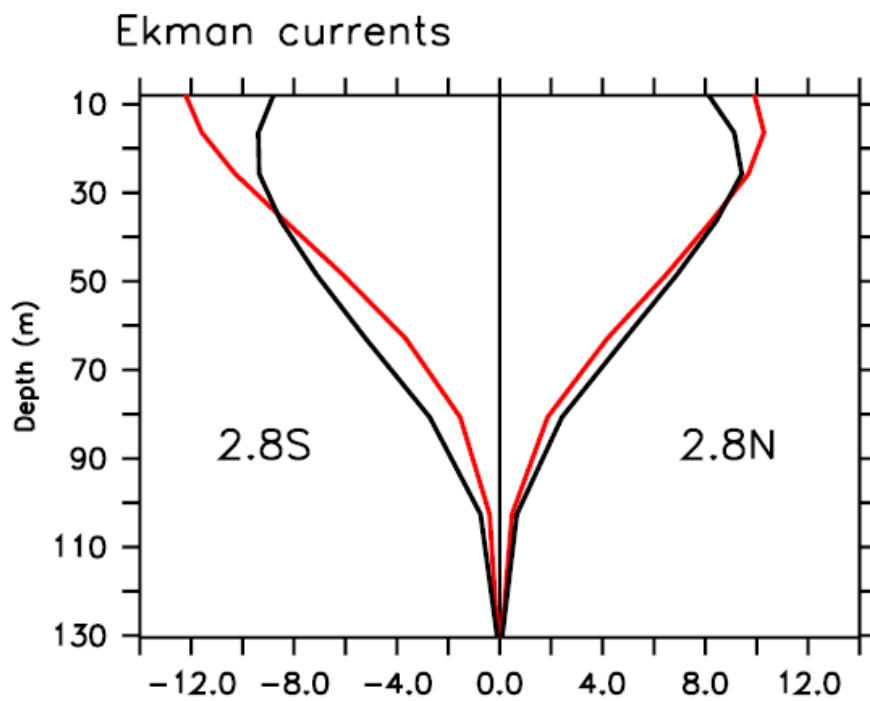


Figure 3.13 Estimated meridional Ekman currents (cm s^{-1}) from CTRL (black) and OCN (red) along 2.8 S and 2.8 N, based on the zonal viscous stress shown in Fig. 3.12.

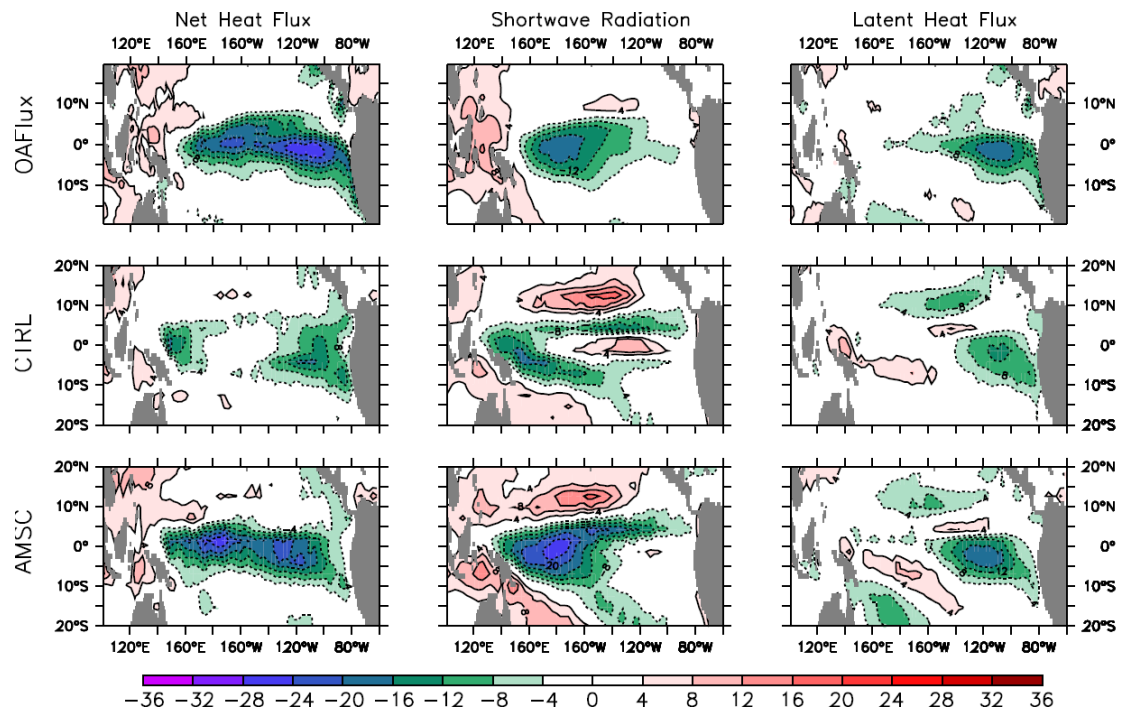


Figure 3.14 Thermal damping measured by the monthly heat flux anomaly regressed onto Niño-3 SSTA for observations (upper), CTRL (middle) and AMSC (bottom). The left panel is for net heat flux, the middle for solar radiation and right panel for latent heat flux. Units: $W/m^2/C$.

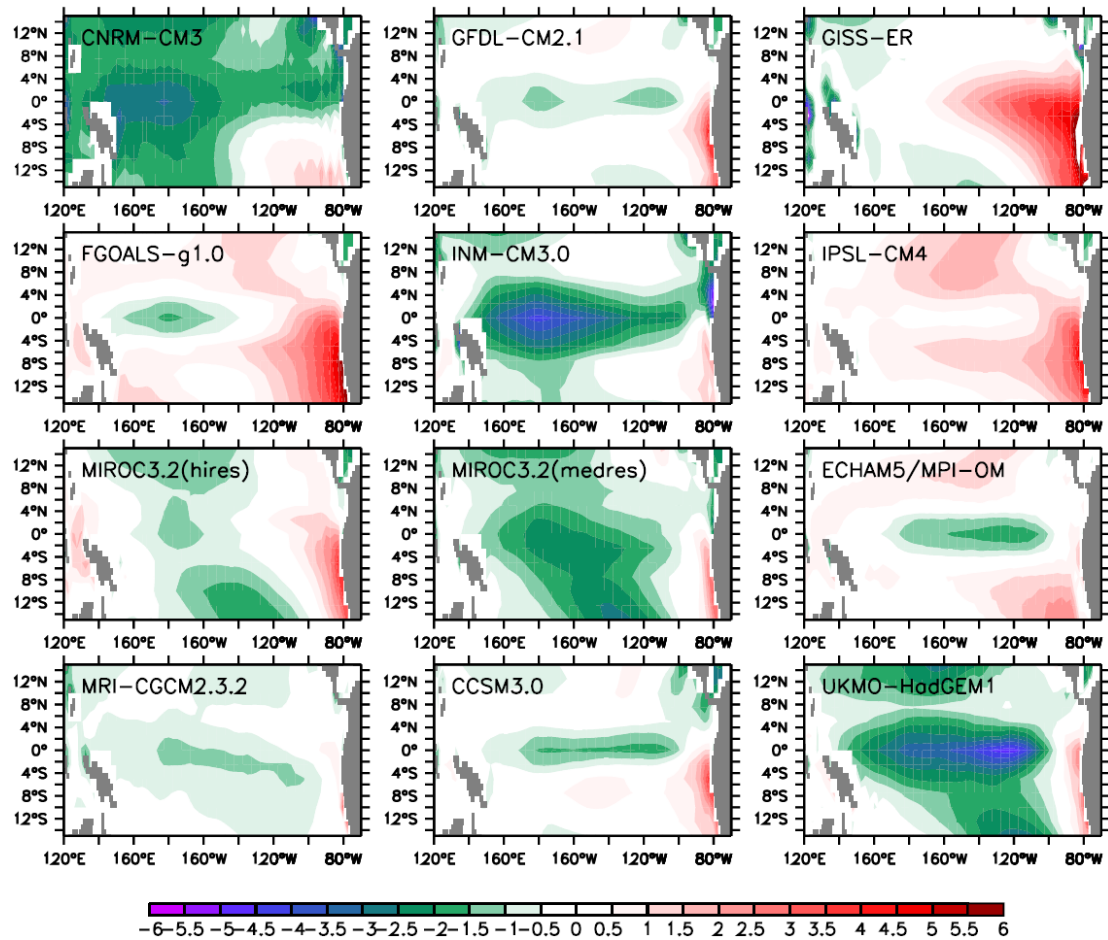


Figure 3.15 The SST bias ($^{\circ}\text{C}$) from 12 CGCMs in comparison to the ERSST climatology. The period 1980-1999 is chosen to be consistent with the AMIP run.

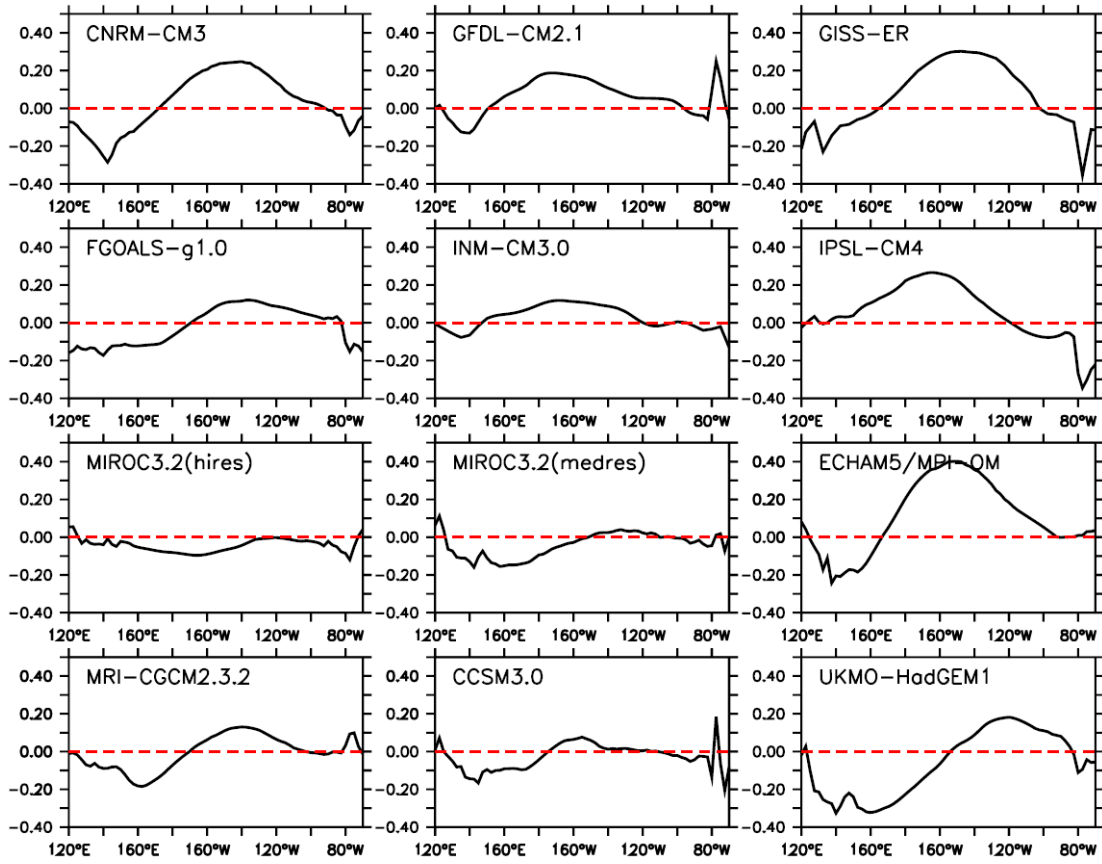


Figure 3.16 The equatorial (5°S - 5°N) zonal wind stress (dyn cm^{-2}) differences between the fully coupled run and AMIP run.

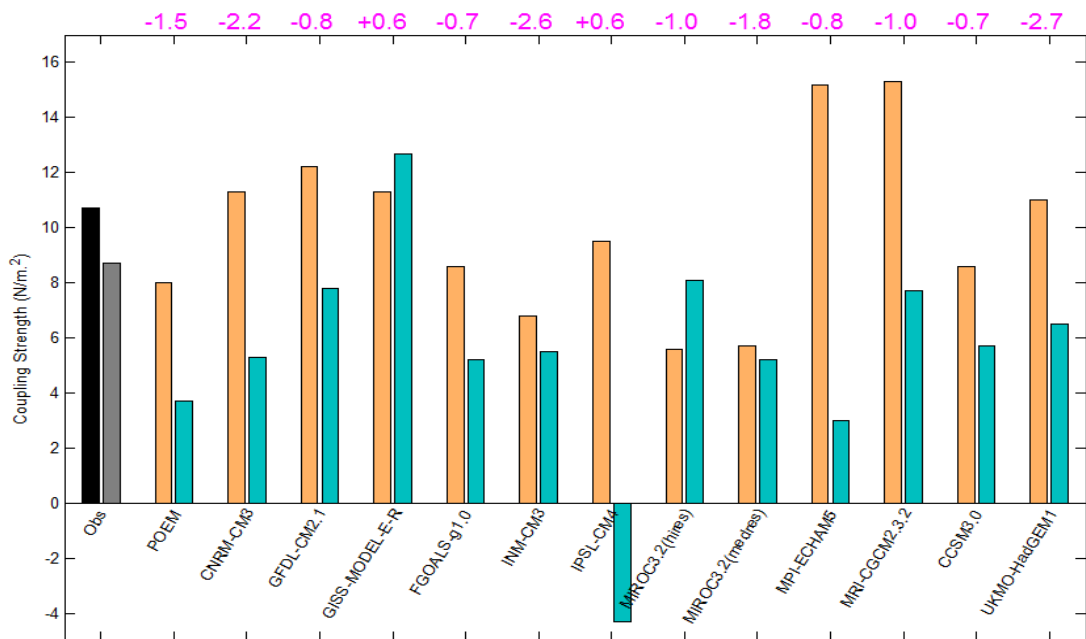
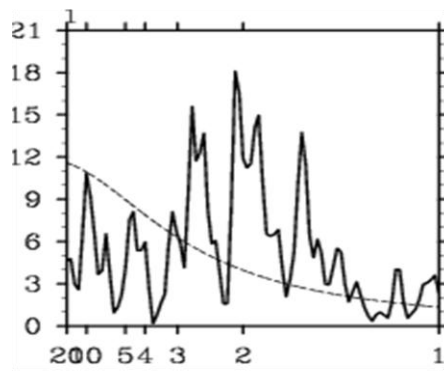
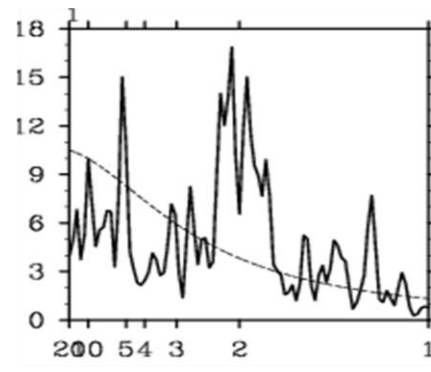


Figure 3.17 Air-Sea coupling strength ($10^{-3} \text{ Nm}^{-2} \text{ }^{\circ}\text{C}^{-1}$) from ERA40 (black), NCEP (grey), AMIP runs (orange) and the corresponding coupled runs (dark cyan).



CTRL



AMSC

Figure 3.18 The power spectrum of the Nino-3 index from the CTRL (left) and AMSC (right). The unit of horizontal axis is years.

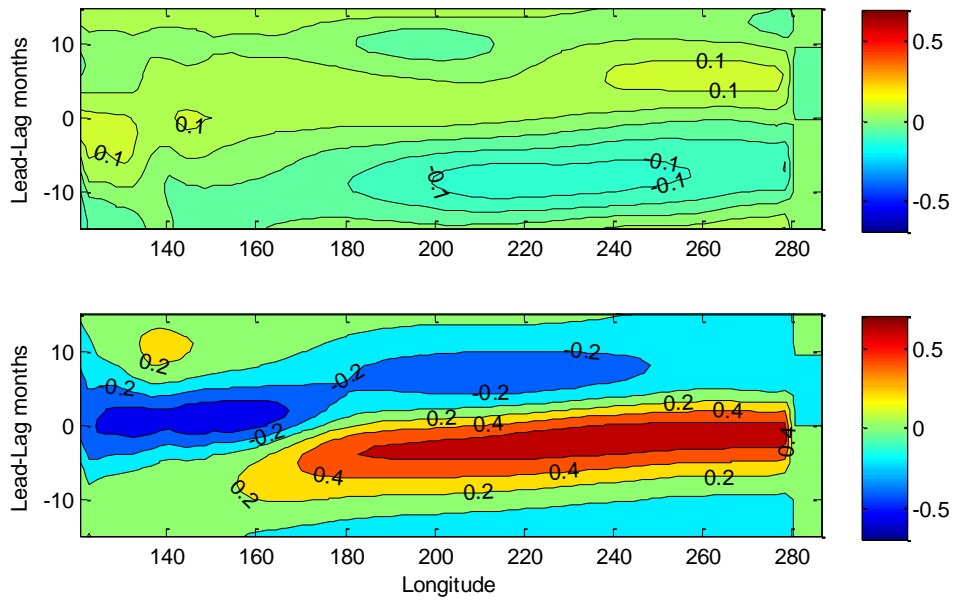


Figure 3.19 Lead-lag correlation between equatorial (5°S-5°N) thermocline depth (SSH) anomaly and the zonal wind stress curl ($-dT_{\text{aux}}/dy$) over the equatorial central Pacific (160°E-130°W, 5°S-5°N). Positive in the lead time means the zonal wind stress curl leads the equatorial thermocline depth anomaly. The zonal wind stress curl multiplies -1 in the southern hemisphere.

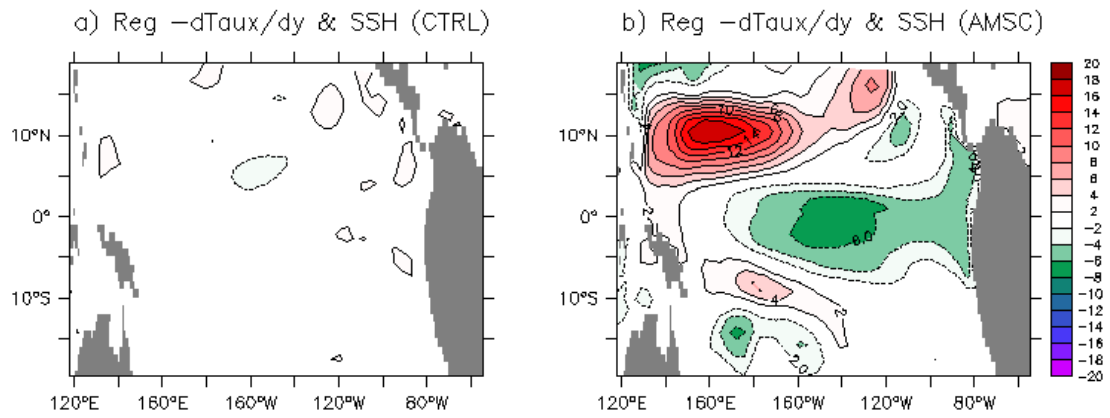


Figure 3.20 Thermocline depth (SSH) change regressed onto the zonal wind stress curl ($-dTaux/dy$) over the equatorial central Pacific ($160^{\circ}E-130^{\circ}W$, $5^{\circ}S-5^{\circ}N$). The thermocline anomaly lags the surface wind stress curl anomalies 9 months. The zonal wind stress curl multiplies -1 in the southern hemisphere.

Chapter 4

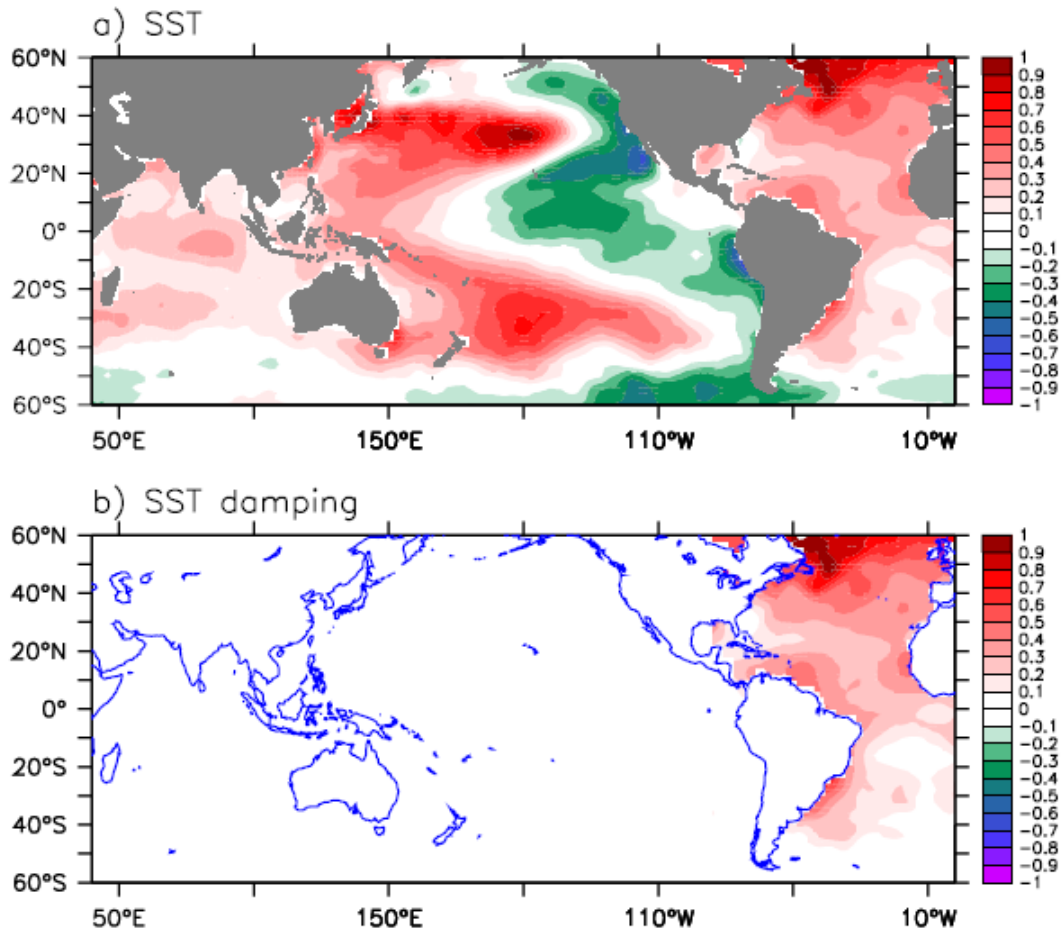


Figure 4.1 a) Epochal SST difference (1999-2010 minus 1980-1998) ($^{\circ}\text{C}$), b) annual mean SST correction term (units: $^{\circ}\text{C}$ per 5 days) in the EXP_AO.

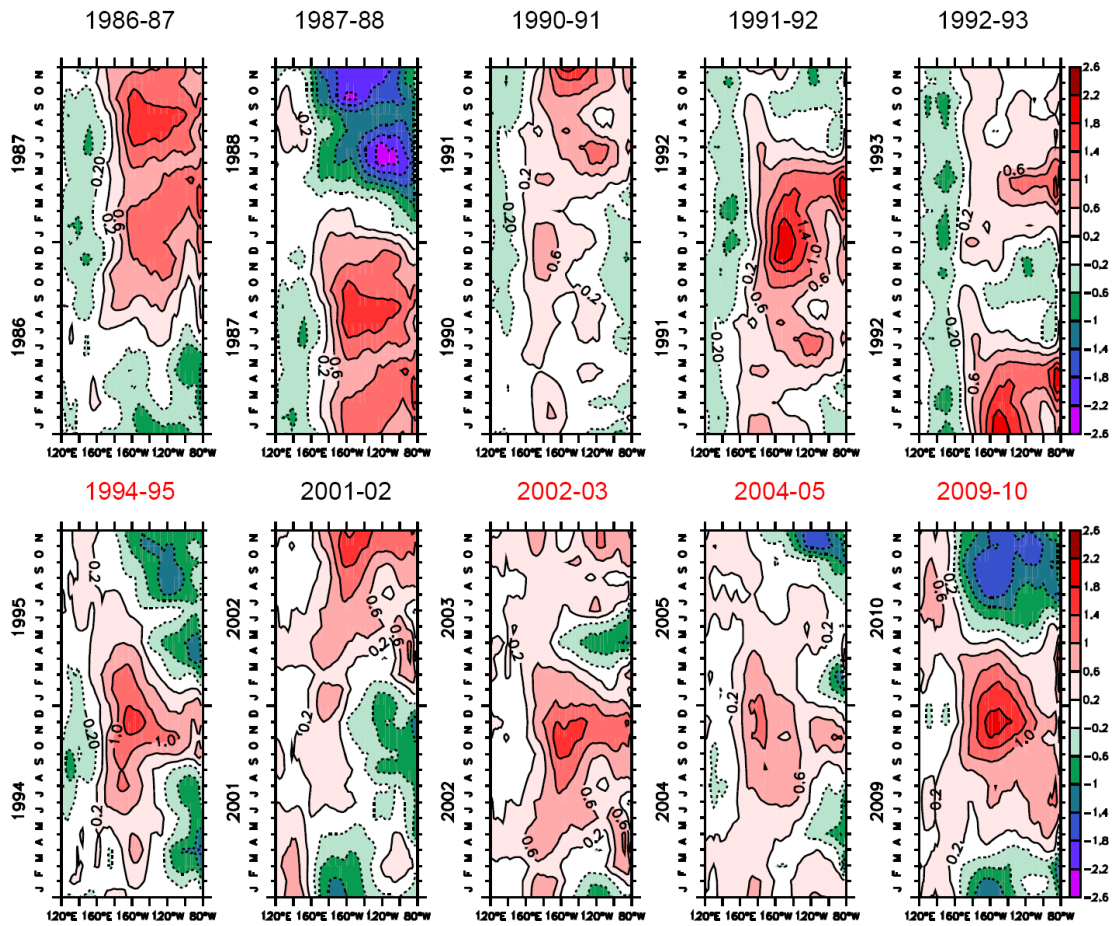


Figure 4.2 Longitude-time diagram of the equatorial (5°S-5°N) SSTA for 10 cases.

The years with red marks denote the robust and standing CPW cases.

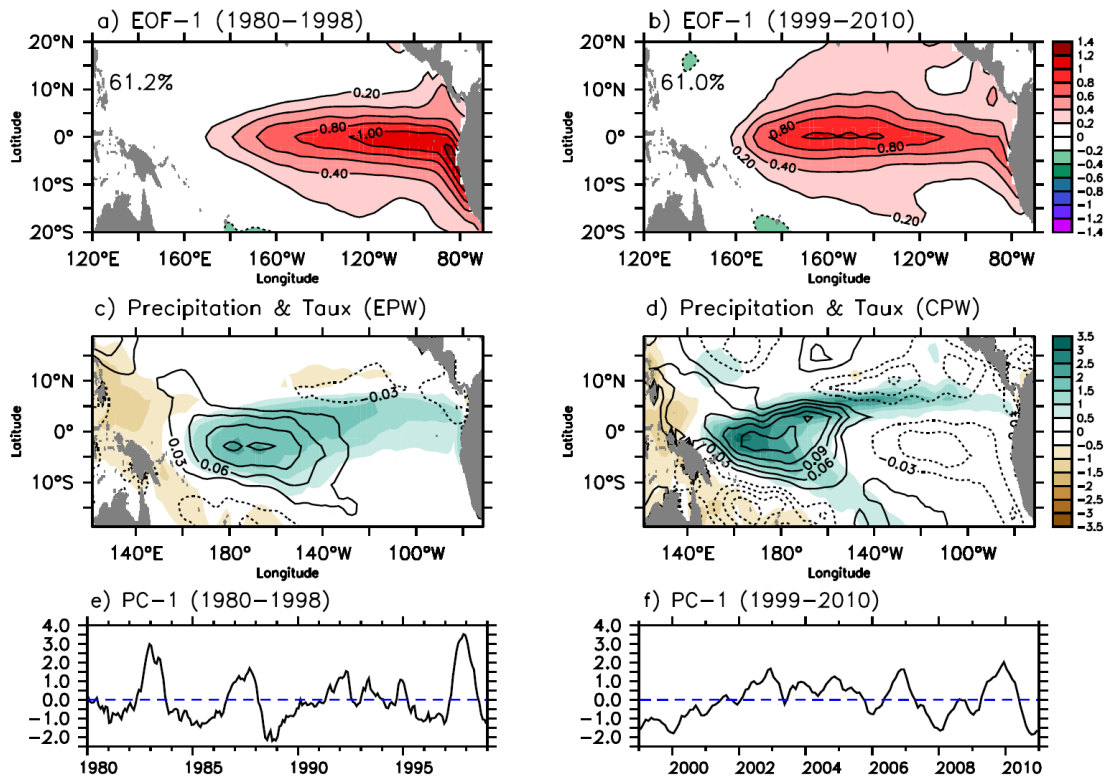


Figure 4.3 The leading EOF of monthly mean SSTA in the tropical Pacific domain during a) 1980-1998 and b) 1999-2010. The fractional variance that can be explained is 60.9%, 60.0%, respectively. c) and d) Linear regression of precipitation (shading in mm/day) and surface zonal wind stress (contours in dyn/cm^2) onto the time series of EOF-1 mode during these two epochs as shown in e) and f), respectively.

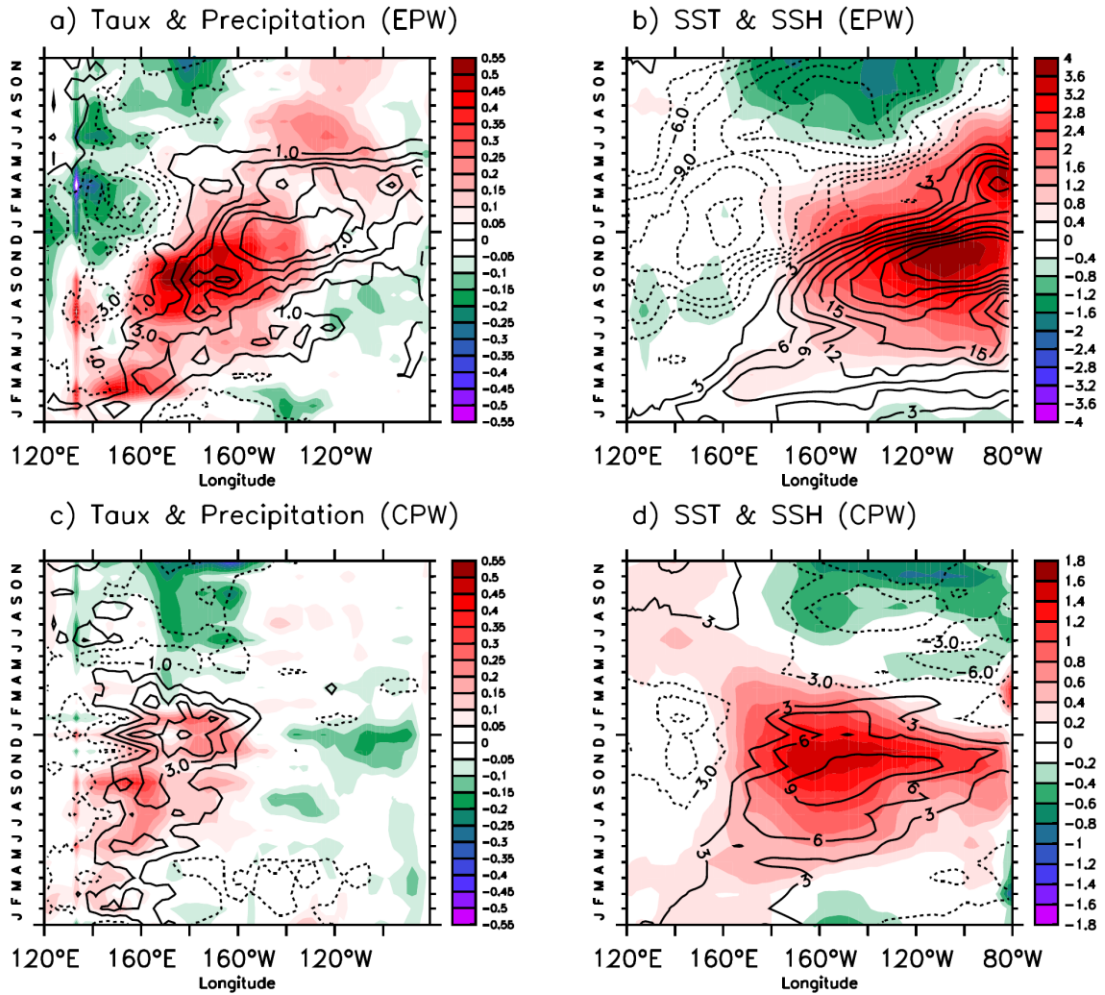


Figure 4.4 Evolution of the composite EPW (1982, 1997, upper panel), and CPW (2002, 2004, 2009, lower panel) averaged between 2°S and 2°N. Panels a) and c) show the anomalous zonal wind stress (shaded in dyn/cm²) and precipitation (contours in mm/day). Panels b) and d) display the SSTA (shaded in °C) and SSH anomaly (contours in cm). Note that the SSTA in b) and d) uses different intervals.

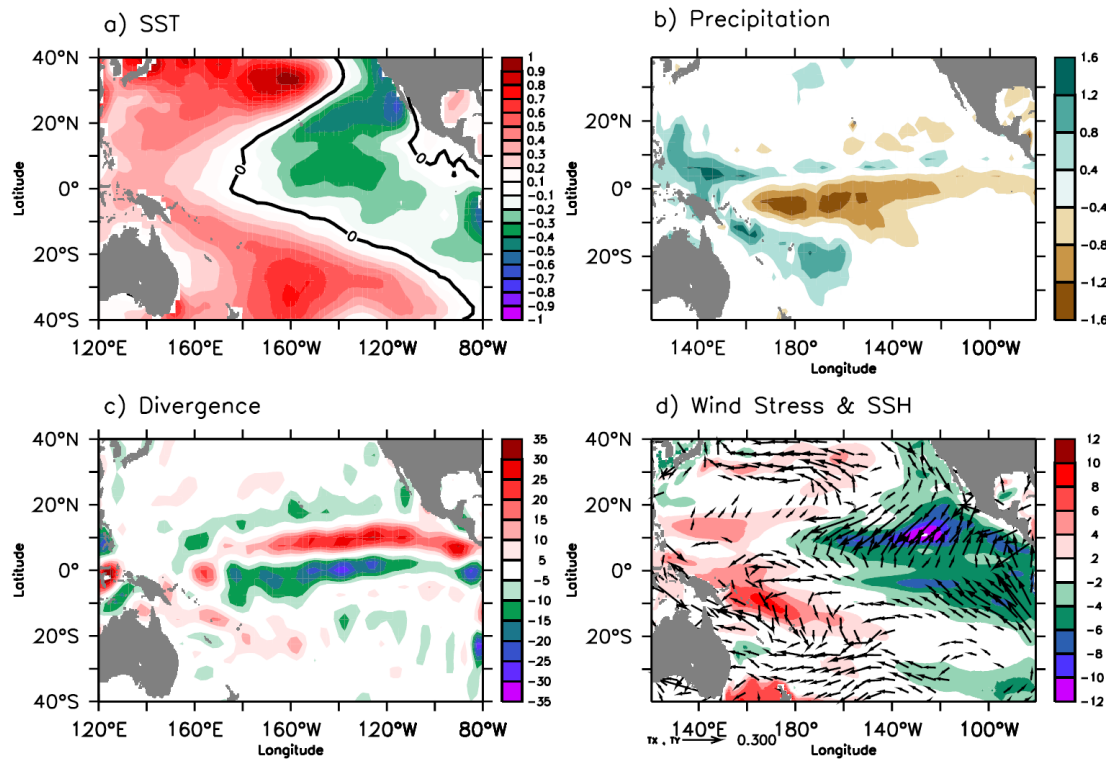


Figure 4.5 Epochal difference (1999-2010 minus 1980-1998) of a) SST ($^{\circ}\text{C}$), b) precipitation (mm/day), c) low-level (1000 hPa) wind convergence ($\times 10^{-7} \text{ s}^{-1}$), and d) SSH (shading in cm) and surface wind stress (dyn/cm²).

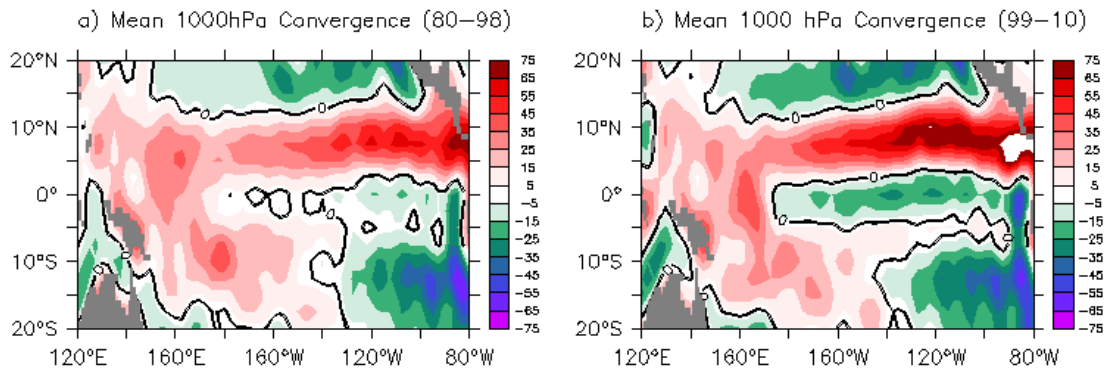


Figure 4.6 Mean low-level (1000 hPa) wind convergence ($\times 10^{-7} \text{ s}^{-1}$) during a) 1980-1998, b) 1999-2010.

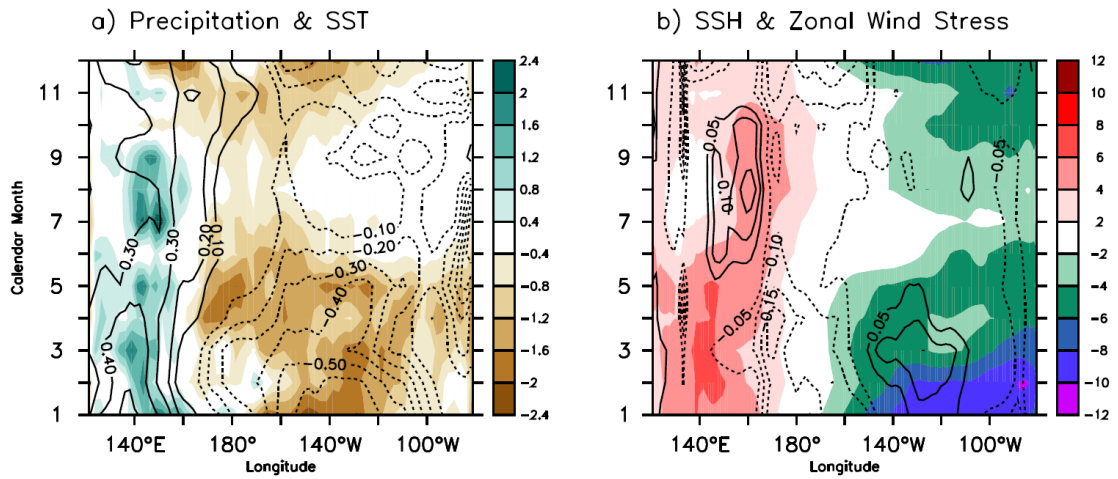


Figure 4.7 Annual cycle change of the equatorial (2°S-2°N) a) precipitation (shading) and SST (contours), b) SSH (shading) and zonal surface wind stress (contours).

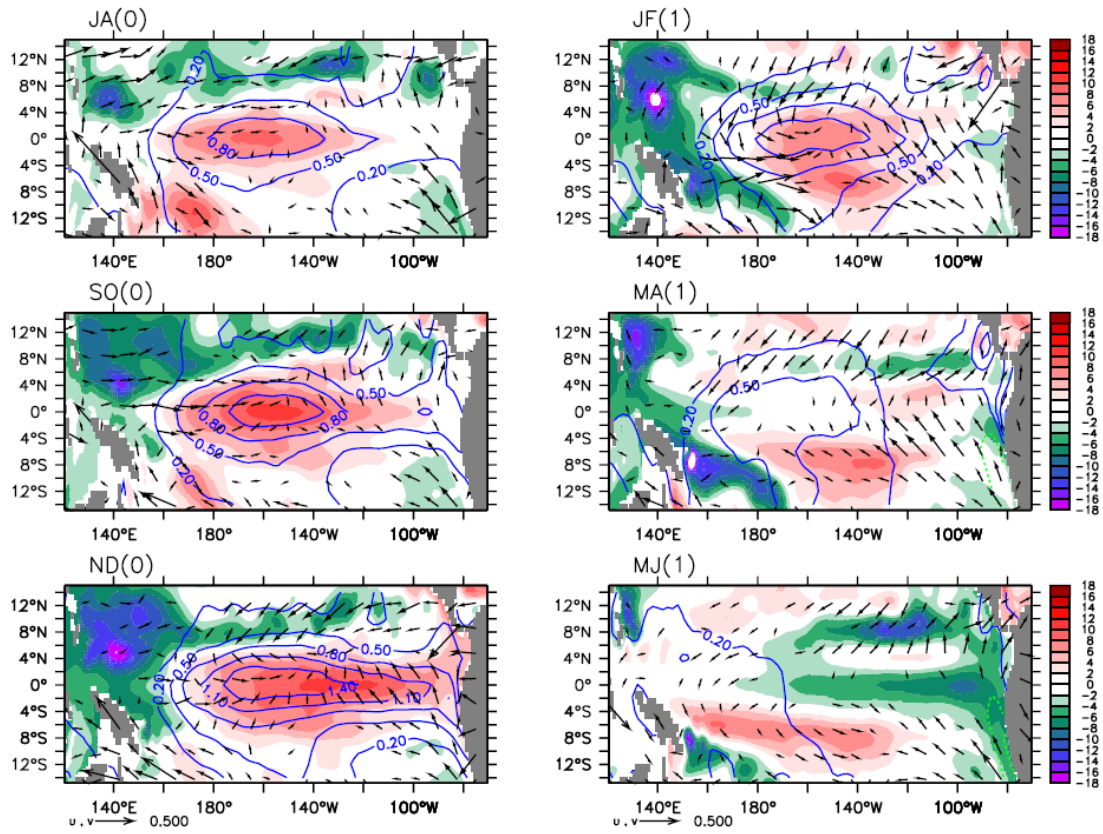


Figure 4.8 Time evolution of composite SSH (shading in cm), SST (contours in $^{\circ}\text{C}$) and surface wind stress (dyn/cm^2) anomalies from July-August (JA) in the developing year to May-June (MJ) in the next year. Three CPW cases are used, 2002, 2004, 2009. Here ‘0’ denotes the El Niño developing year and ‘1’ for the decaying year.

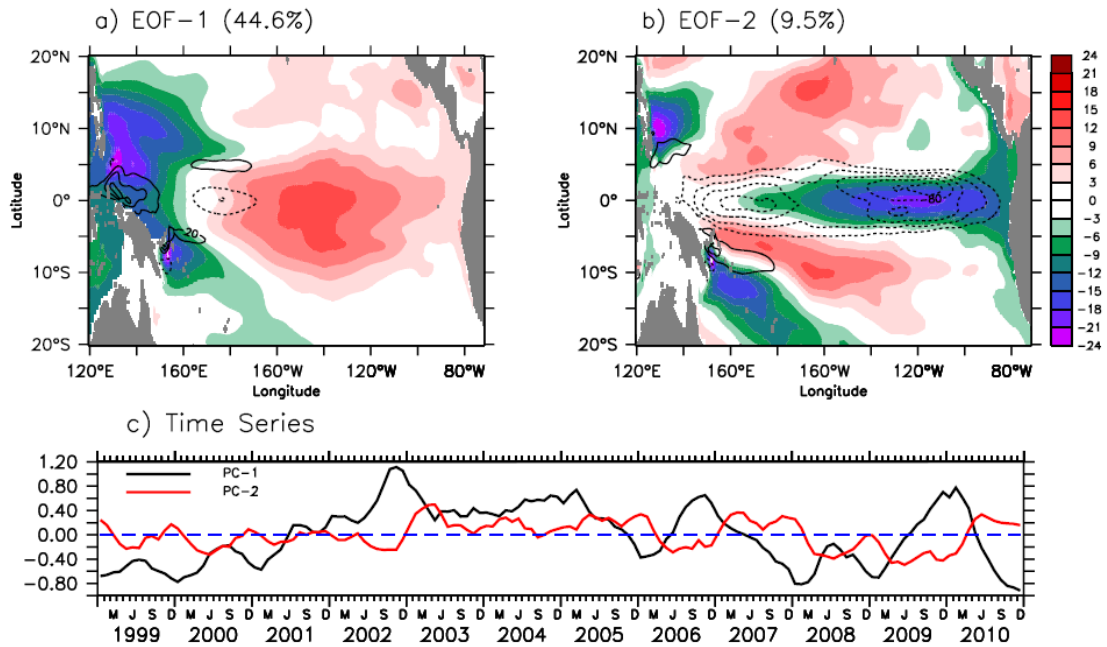


Figure 4.9 a), b) The first two leading EOF modes (shading) of SSH anomaly during 1999-2010. The contours in a) and b) are the linear regression of zonal current anomaly (cm/s) averaged over upper 35 m onto the time series of these two modes as shown in panel c). The fractional variance that can be explained by these two modes are 43.5%, 9.5%, respectively.

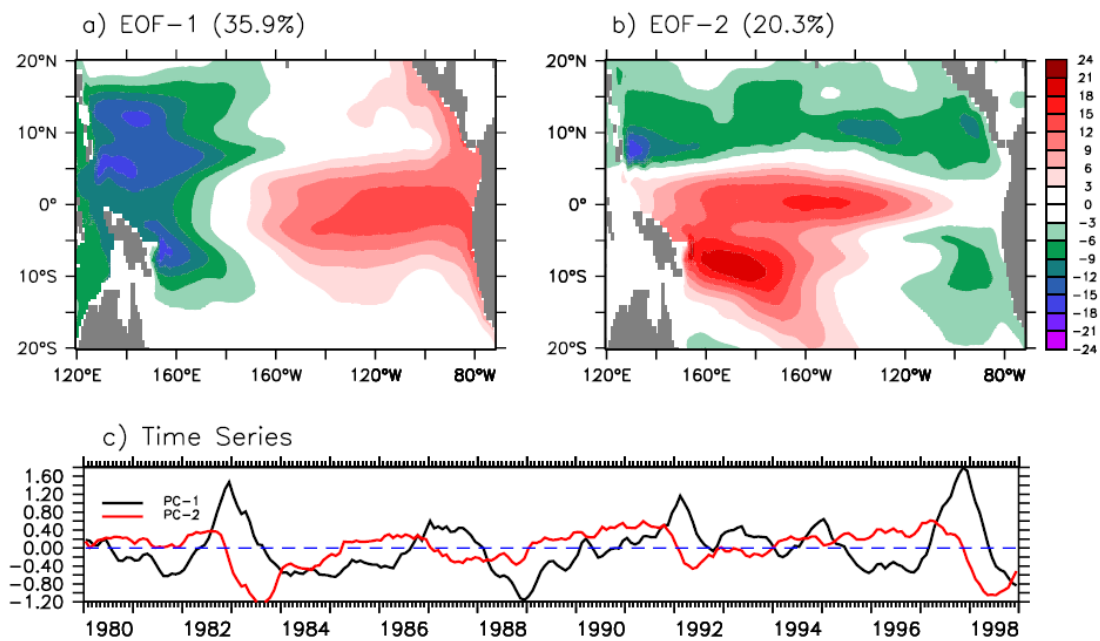


Figure 4.10 a), b) The first two leading EOF modes (shading) of SSH anomalies during 1980-1998. c) the time series of these two EOF modes.

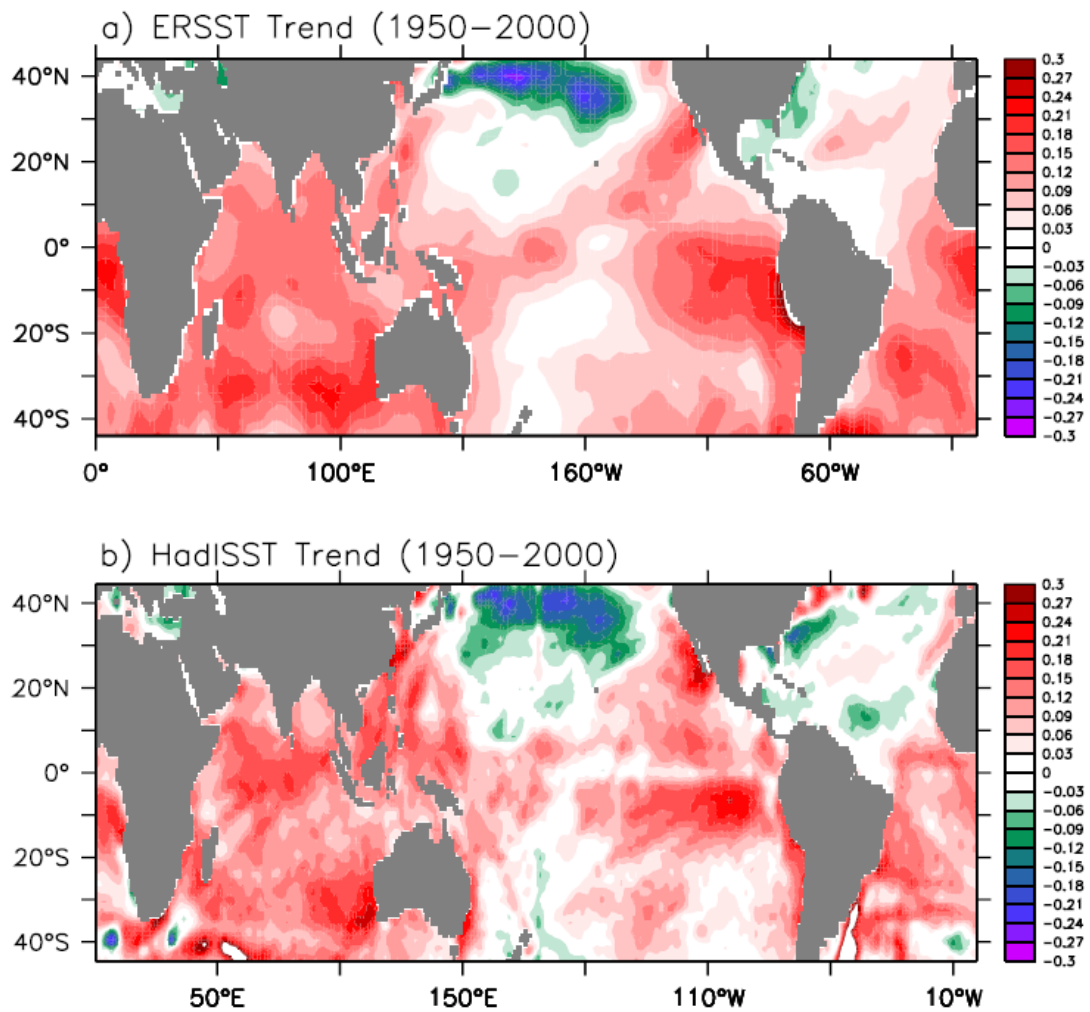


Figure 4.11 The linear trend of SSTA ($^{\circ}\text{C}$ per decade) for the period between 1950 and 2000 from a) ERSST and b) HadISST [Rayner *et al.*, 2003]. The reason to use this period is twofold: The most evident global warming occurs during this period and large uncertainty for the SST data exists before 1950 due to the lack of observations over ocean.

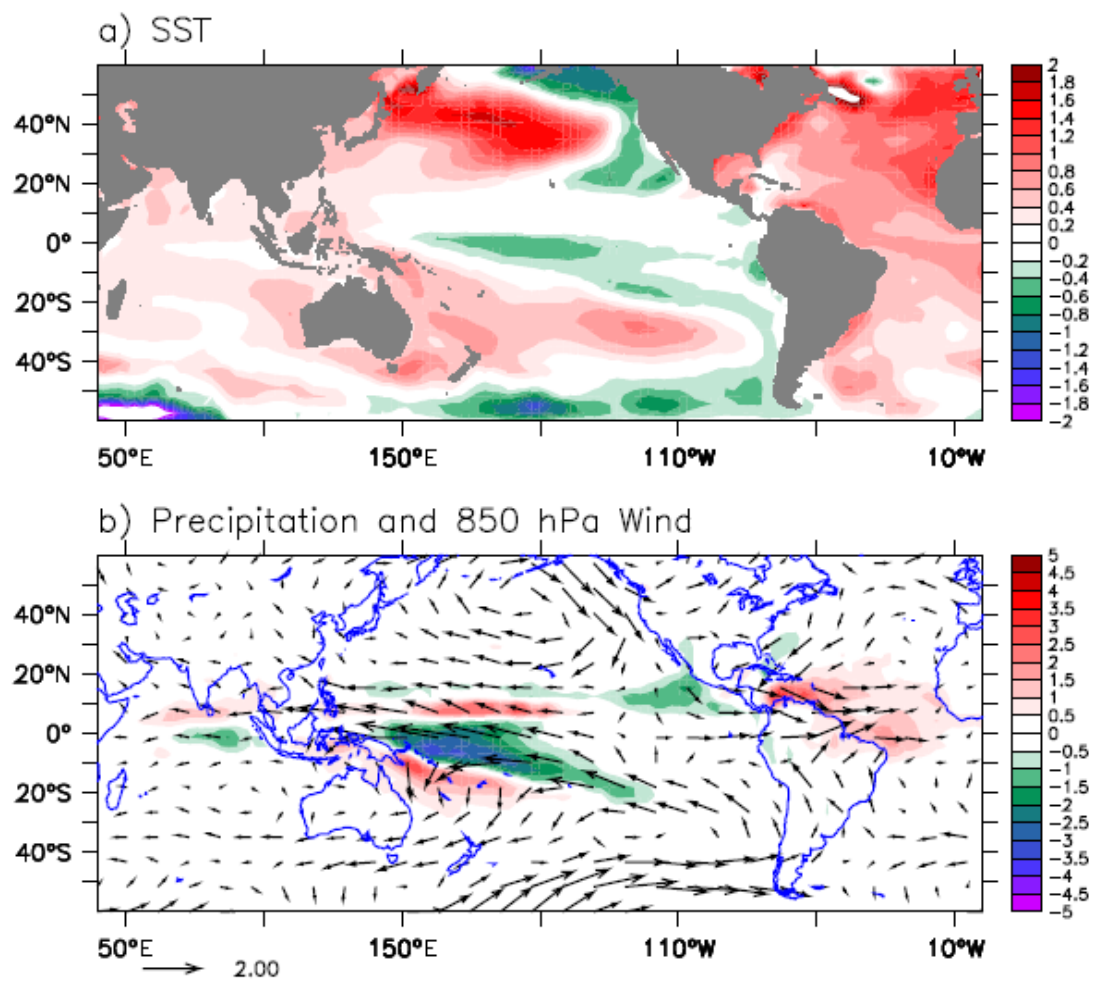


Figure 4.12 Time-mean a) SST, b) precipitation and 850 hPa wind differences between EXP_AO and AMSC.

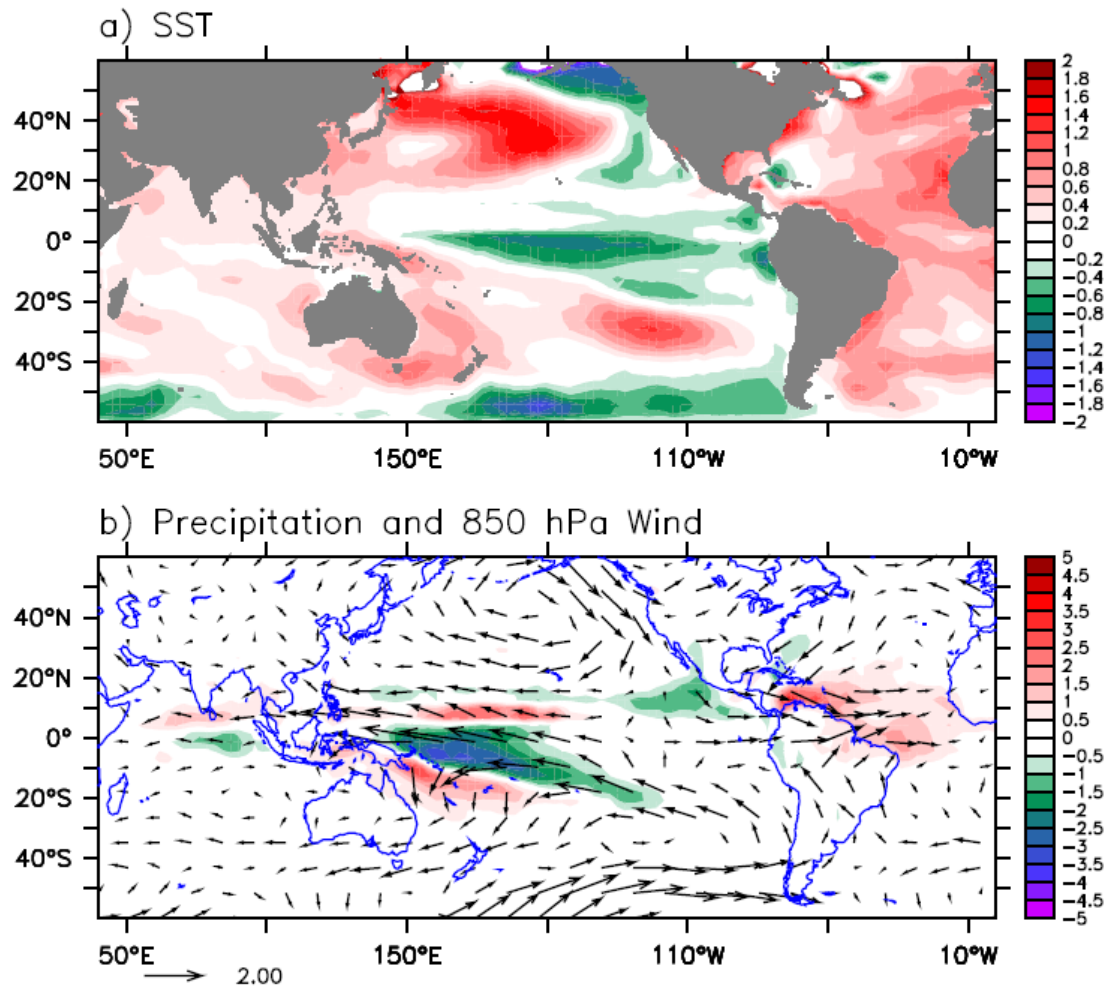


Figure 4.13 the same as Figure 4.11 but for boreal winter (DJF).

Chapter 5

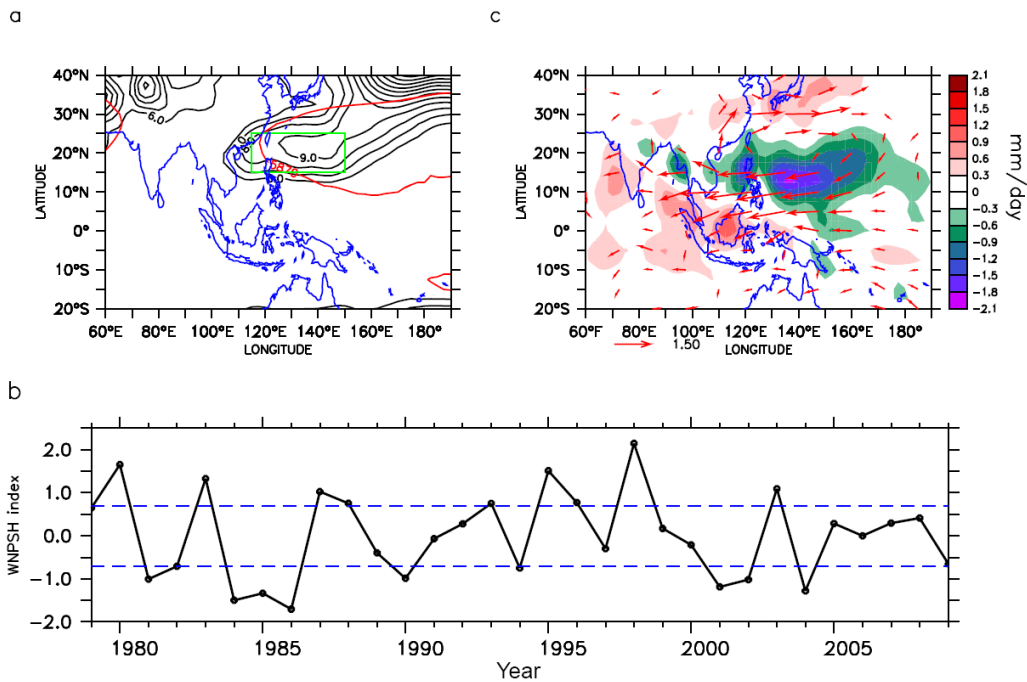


Figure 5.1 a) Standard deviation of H850 (black contours in m). The red contour line (5870 m at 500 hPa) outlines the western North Pacific Subtropical High (WNPSH). b) The normalized WNPSh index defined by the H850 anomaly averaged over the green box indicated in a). Blue dashed lines represent 70% of the standard deviation of the WNPSh index. c) The regressed patterns of 850 hPa wind vectors (not shown when smaller than 0.2 m/s) and precipitation (shading) onto the normalized WNPSh index during JJA.

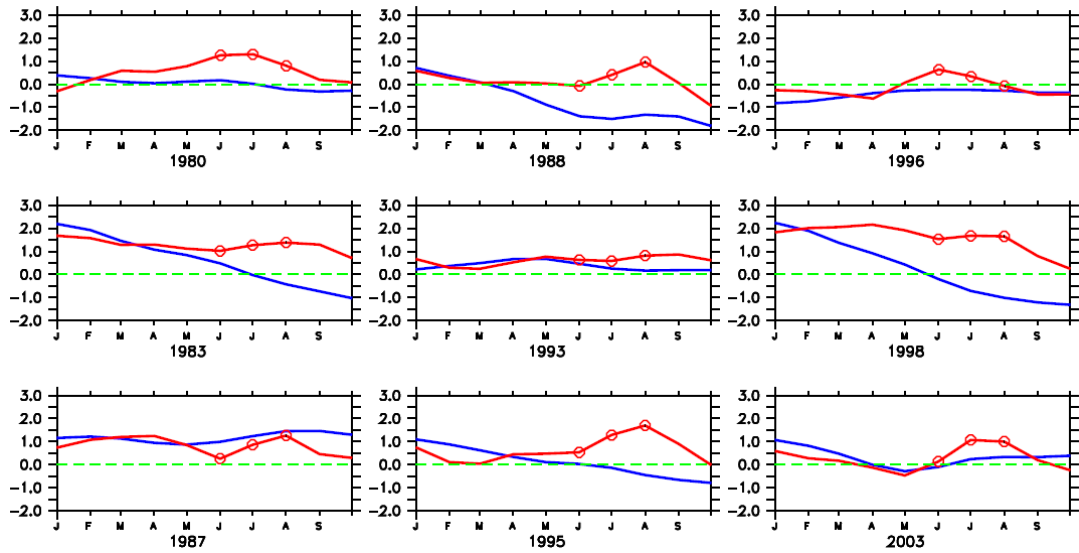


Figure 5.2 The 3-month running mean WNP5H index (red) and Niño 3.4 SSTA (blue) for the 9 strong WNPAC years. JJA season is indicated by circles in the WNP5H index. Note that only 4 cases (1983, 1988, 1995, and 1998) occurred during El Niño decay summers.

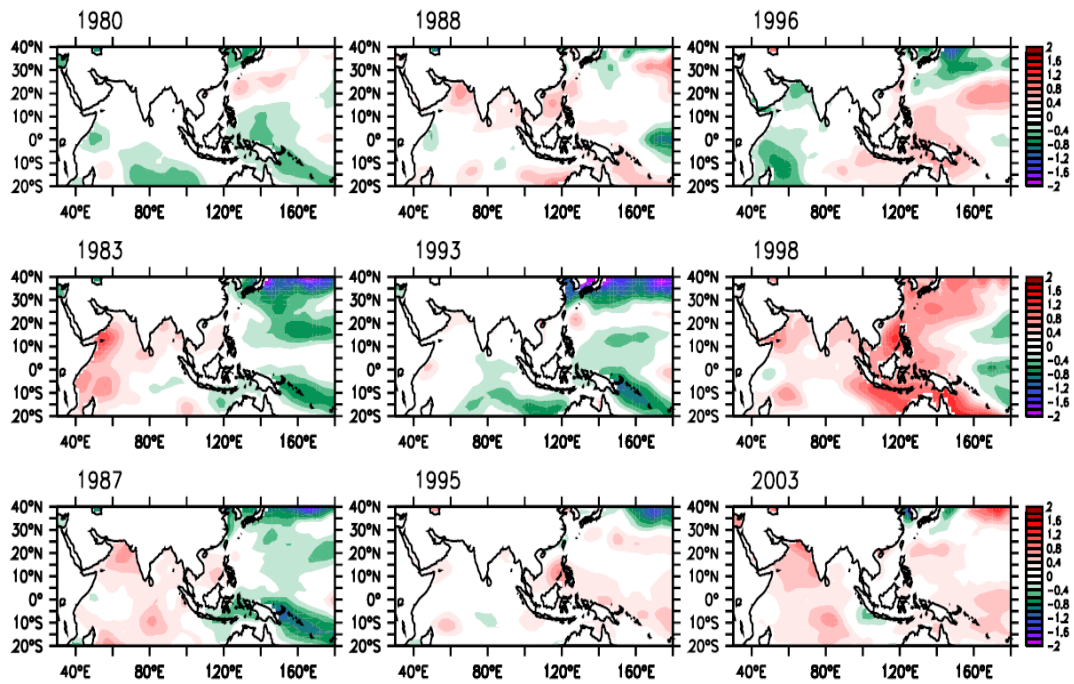


Figure 5.3 Summertime (JJA) SSTA during 9 strong WNPAC cases. Note that 4 cases do not accompanied by Indian Ocean warming (1980,1993, 1995, and 1996).

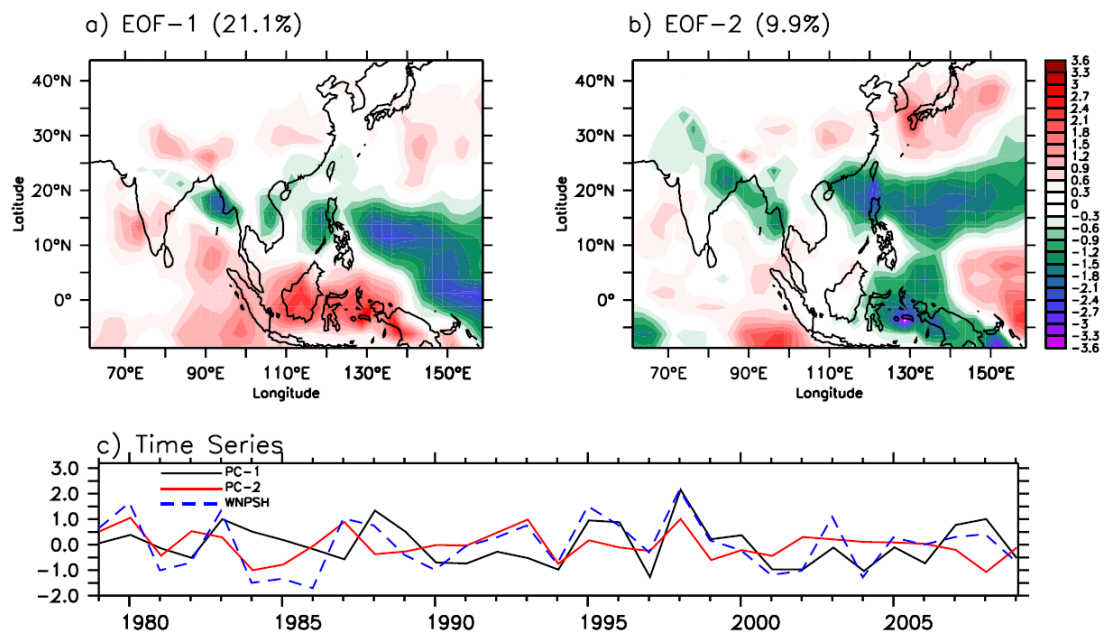


Figure 5.4 a), b) The spatial patterns of the first two leading EOF modes of Asian summer (JJA) monsoon precipitation anomaly during 1979-2009. The fractional variance that can be explained by these two modes are 21.1%, and 9.9%, respectively. c) The corresponding principal components, PC-1 and PC-2 with the WNPSH index. The correlation coefficients of the WNPSH with the PC1 and PC2 are 0.58 and 0.56, respectively.

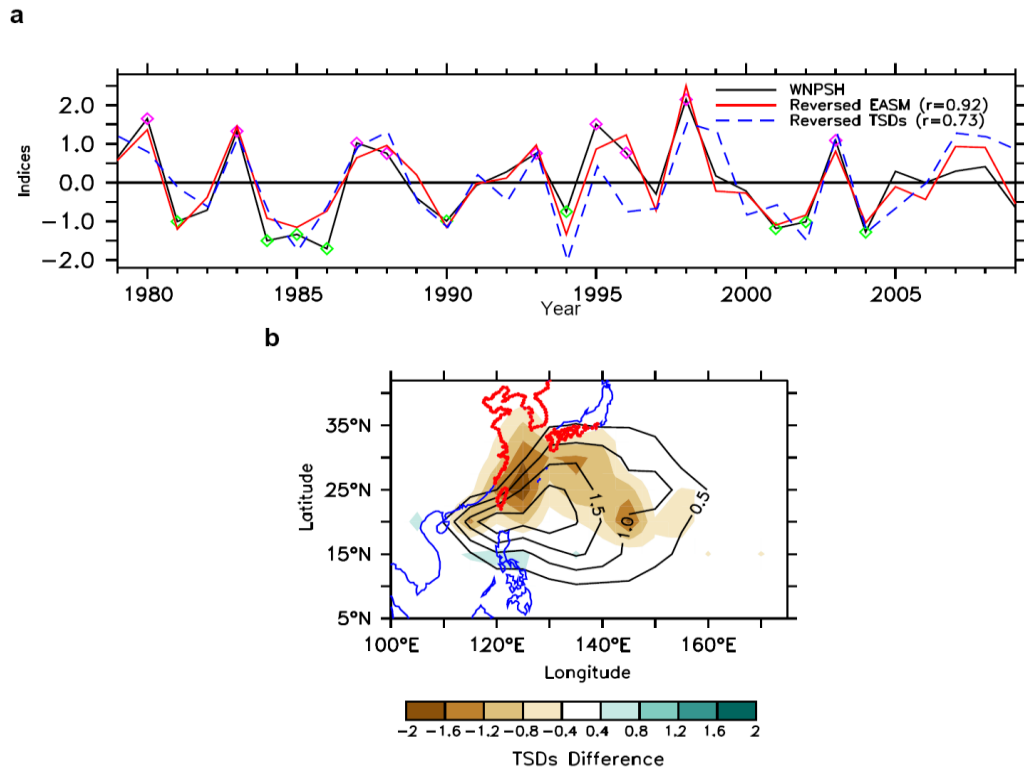


Figure 5.5 a) Interannual variations of the WNPSH intensity, East Asian summer monsoon (EASM) strength (reversed) and the total number of TS days (TSDs, reversed) over the subtropical WNP (20°N-35°N, 110°E-165°E). The WNPSH intensity is defined by the normalized H850 anomaly averaged over its maximum variability center (15°N-25°N, 115°E-150°E). The EASM strength is measured by the leading principal component of the precipitation, 850 and 200 hPa winds of the EASM system. The numbers in the brackets indicate correlation coefficients with the WNPSH intensity. The purple (green) polygons in the time series of WNPSH index indicate the strong (weak) WNPSH years with anomalous amplitudes exceeding 0.7 standard deviations. b), The long-term mean TSDs in JJA (contours in days per year) and the difference (shading) between 9 strongest and 9 weakest WNPSH years. The red line in b) shows the coastal regions of TS landing. The interannual variation of the landing TS numbers has a significant correlation with the WNPSH ($r=0.66$).

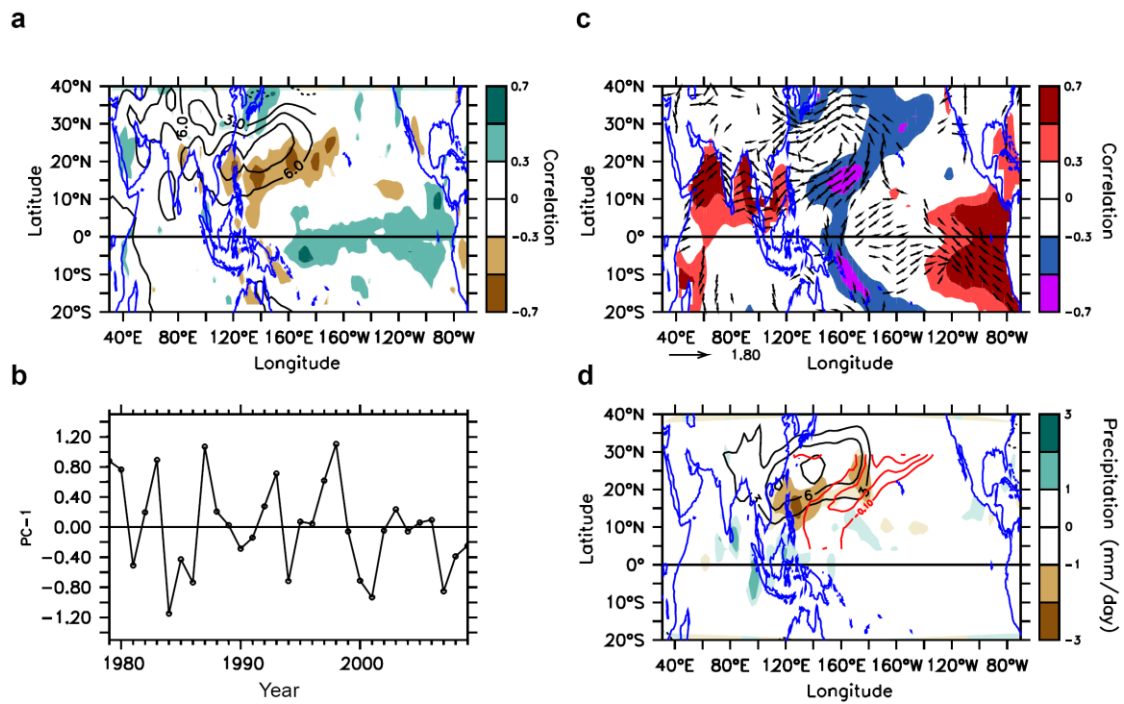


Figure 5.6 a) The spatial pattern of H850 anomaly (contours) and correlated precipitation (shading). b) the corresponding principal component (PC-1). c) The correlated SSTA (shading) and 850 hPa wind anomalies. The correlation fields were made with reference to PC-1 and only correlations significant at 10% confidence level ($r > 0.3$) are shown. d) Simulated JJA H850 (black contours in m) and precipitation (shading in mm/day) anomalies with ECHAM4 model forced by prescribed cold SSTA (red contours with interval of 0.1 °C).

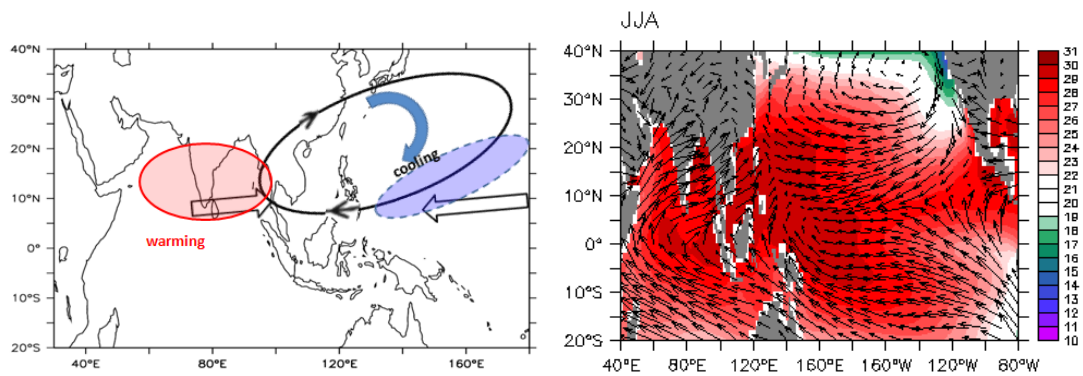


Figure 5.7 Left panel: Schematic diagram to show the IO-WNP anticyclonic coupled mode. The double arrows denotes the mean flow in boreal summer (JJA). The red (blue) shading regions indicate the SST warming (cooling). The heavy lines wind arrows show the anomalous circulation. Right panel: JJA mean SST (shading) and 1000 hPa wind (vectors).

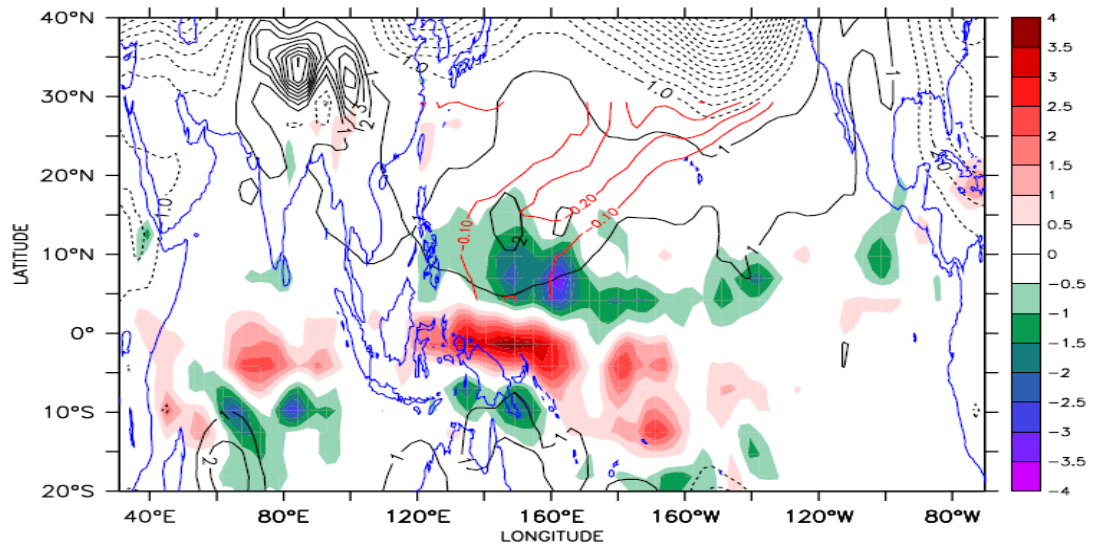


Figure 5.8 Same as Fig. 5.7d but for boreal spring (March-May) mean state. The solid red lines outline the SSTA forcing.

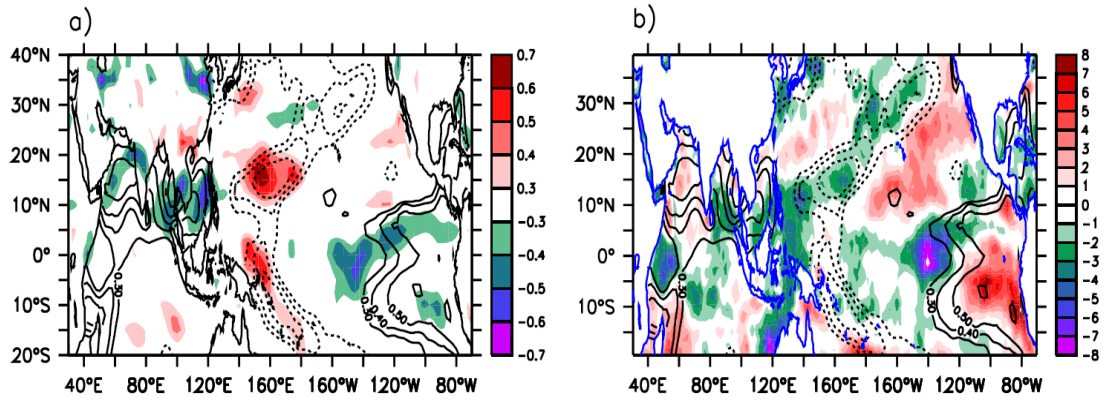


Figure 5.9 a) The correlation between PC-1, and 1000 hPa wind speed (shading), and SSTA (contours). b) Surface latent heat flux regressed onto PC-1 (shading, negative means loss heat flux from ocean surface), and the correlation between PC-1 and SSTA (contours).

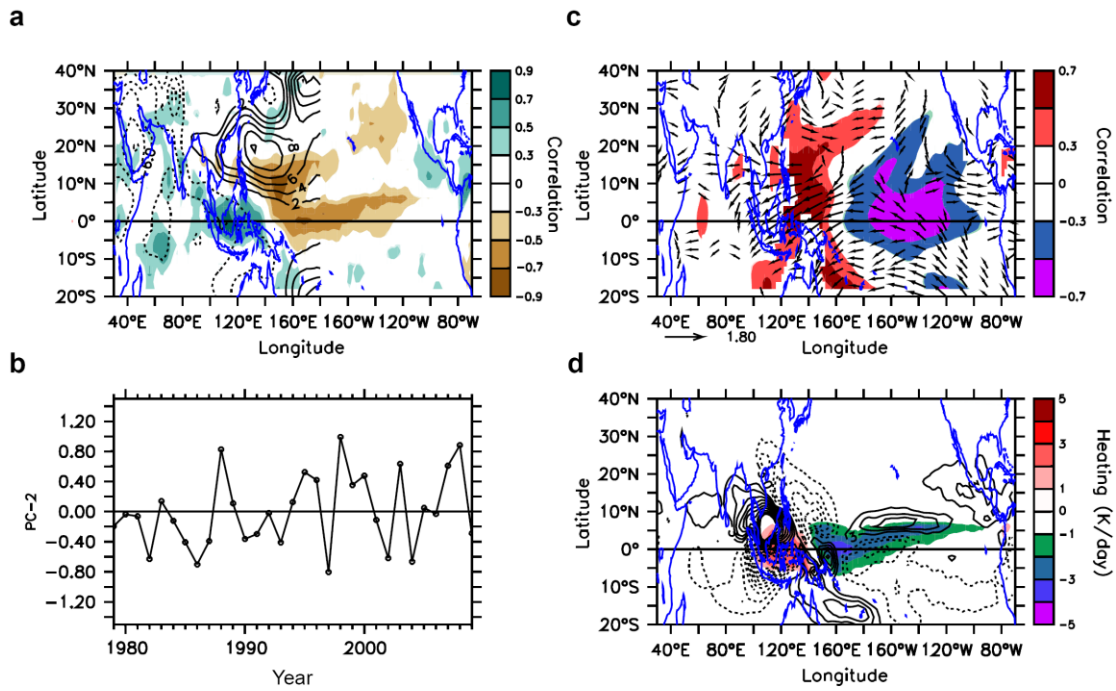


Figure 5.10 a), b), c) are the same as in Fig. 5.7 but for EOF-2 mode. d), Low-level vorticity (contours in 10^{-7}m/s^2) in response to a specified mid-tropospheric heating (shading) obtained from an intermediate atmospheric model with JJA mean flow.

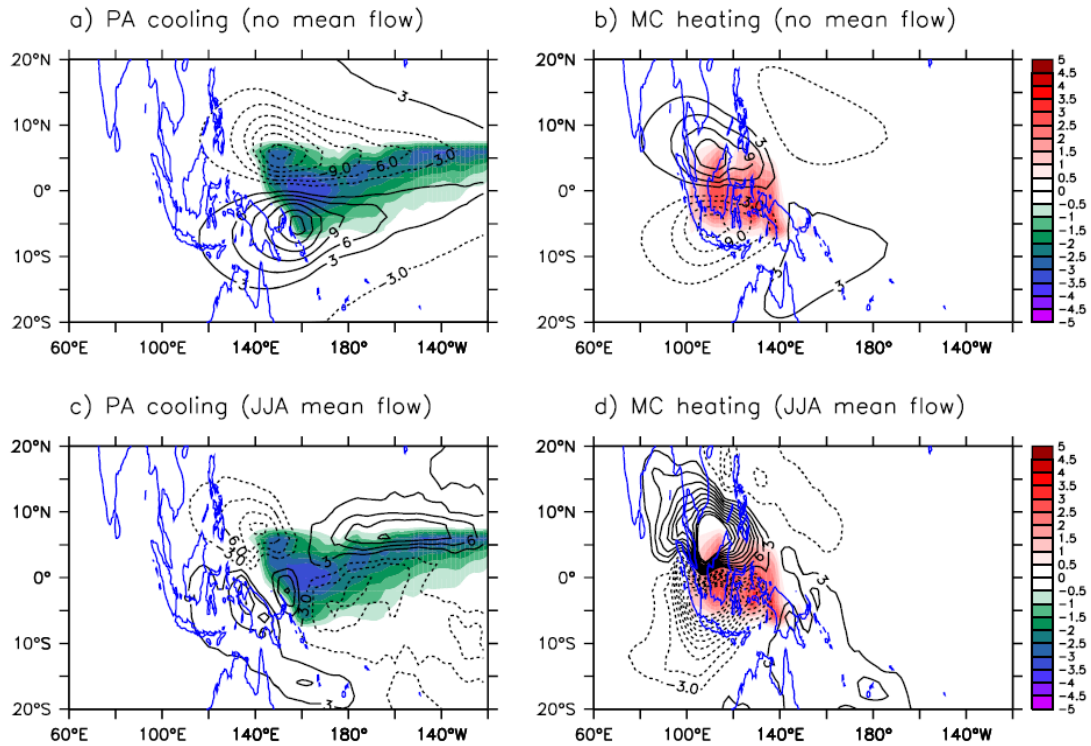


Figure 5.11 Atmospheric low-level vorticity responses ($\times 10^{-7} \text{ s}^{-1}$, contours) to the prescribed Pacific cooling (left panel) and maritime continental heating (right panel) (colour) in an intermediate atmospheric model. Upper panel shows the experiments without mean flow and the lower panel is with boreal summer (JJA) mean flow. Note that in the presence of mean flows, the response is enhanced over the monsoon regions due to the fact that a background easterly vertical shear can amplify Rossby wave responses (Wang and Xie 1996).

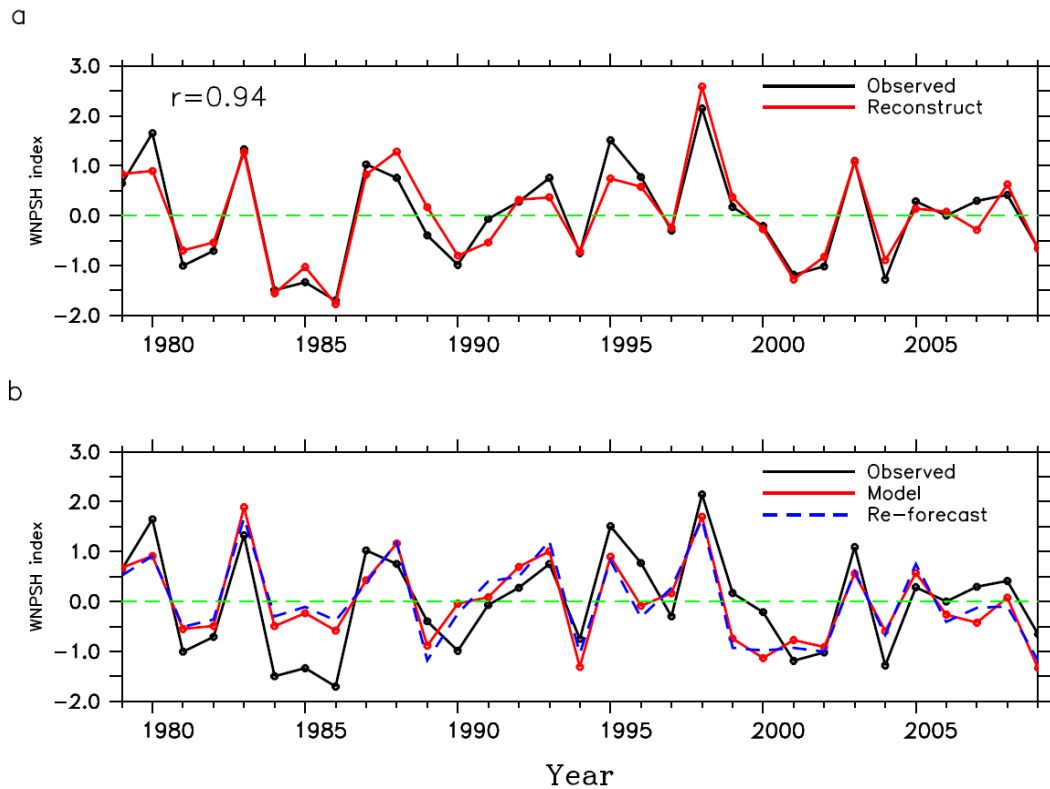


Figure 5.12 a) Reconstruction of the JJA WNPSH index with the first two principal components. Shown are the normalized WNPSH index (black) and the reconstructed (red) index based on PC1 and PC2 ($1.226 \times PC-1 + 1.245 \times PC-2$). They have a correlation coefficient of 0.94. b) The observed WNPSH index (black) and the model simulated index (red) and re-forecasted index (blue). The simulation of the WNPSH intensity was made based on the Eq. (1) (see text). The correlation between the observed WNPSH index and the simulated (re-forecasted) WNPSH index is 0.81 (0.75).

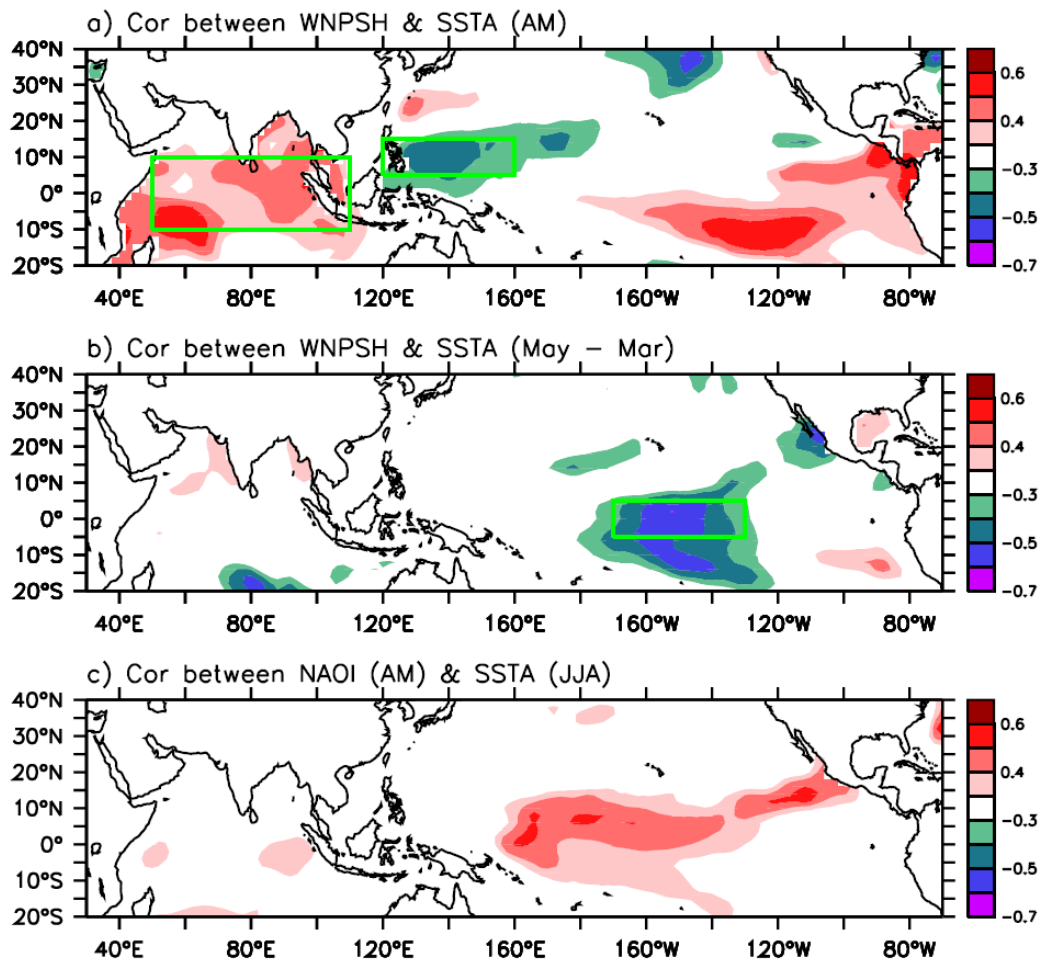


Figure 5.13 Selection of predictors based on the correlation maps between a, the WNP5H (JJA) index and the April-May mean SSTA, b) the WNP5H (JJA) index and the May-minus-March SSTA, and c, the NAO (April-May) index and boreal summer (JJA) SSTA. Only values with significance level above 90% are shown. The boxes in the panels a and b indicates the area where area-averaged SSTAs are selected for constructing the corresponding predictors.

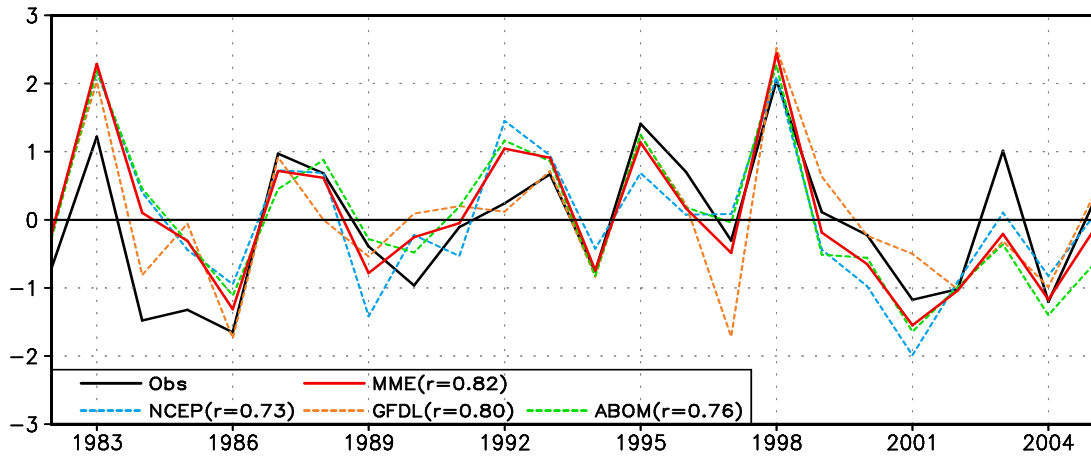


Figure 5.14 The observed WNPSH index (black) from 1982 to 2005. The red line denotes the multi-model ensemble (MME) result using the June 1st initial condition (zero-month lead forecast). Results from three individual models (NCEP, GFDL, ABOM) are shown by dashed lines. The correlation between the observed WNPSH index, and MME, NCEP, GFDL, ABOM are 0.82, 0.73, 0.80, and 0.76, respectively. The hindcast experiments data were provided by NCEP (National Center for Environmental Prediction), GFDL (Geophysical Fluid Dynamics Laboratory), and ABOM (Australian Bureau of Meteorology) through APEC Climate Center(APCC)/ climate prediction and application to society (CliPAS) project (Wang et al. 2008, Lee et al. 2011).

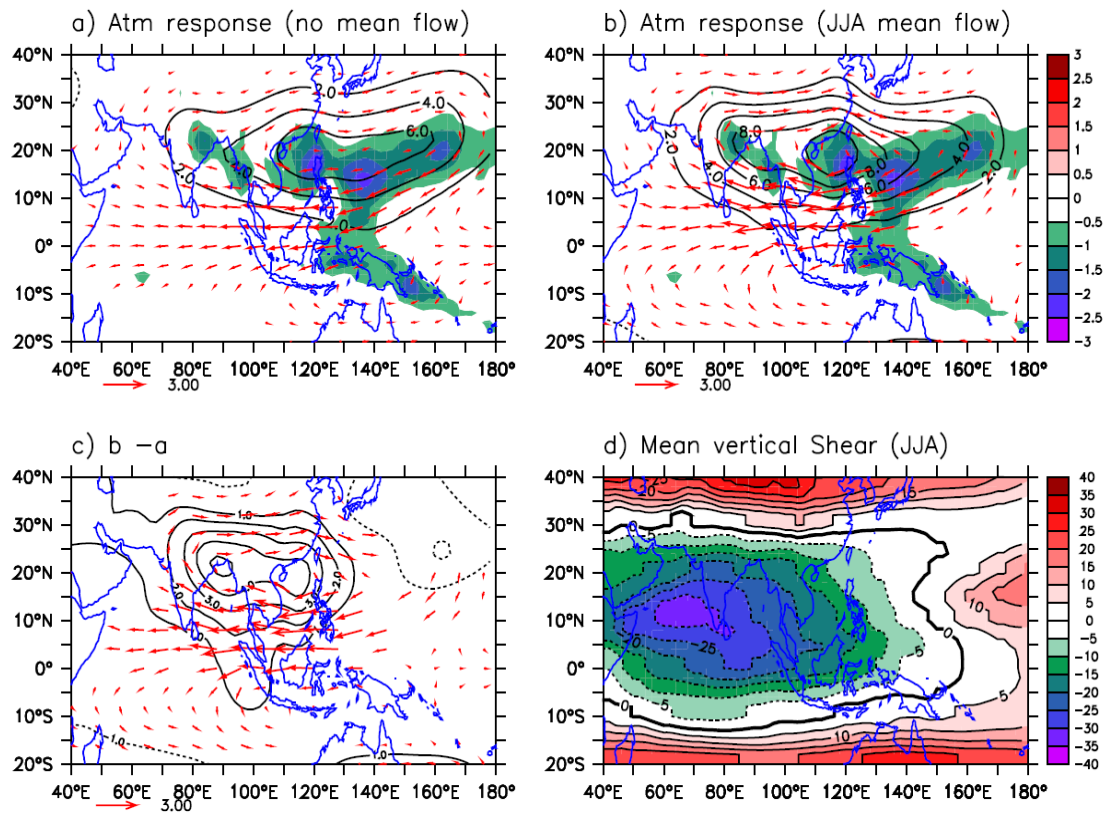


Figure 5.15 Low level wind (vectors) and geopotential height response to the prescribed heating (shading in K/day) with a) no mean flow, b) boreal summer (JJA) mean flow. c) is the difference between b) and a). d) mean vertical shear (m/s) during JJA by the zonal wind difference between 200 hPa and 850 hPa. The model we used here is a two and half layer atmospheric model (Wang and Li 1993).

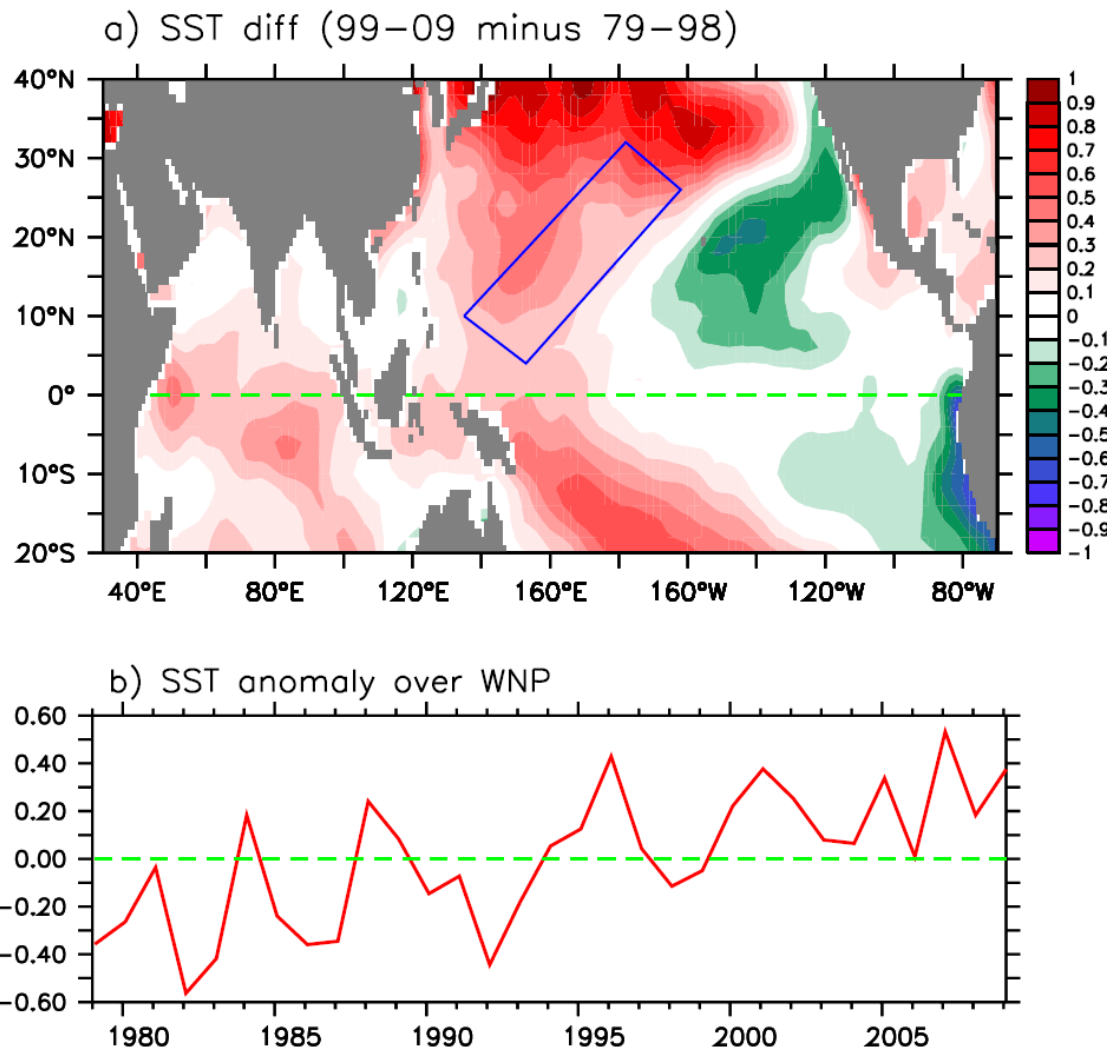


Figure 5.16 a) Summertime (JJA) SST difference between two epochs, 1999-2009 and 1979-1998. b) SSTA averaged over the blue box in a) during JJA. The blue box is the location of the WNP cooling associated with EOF-1.

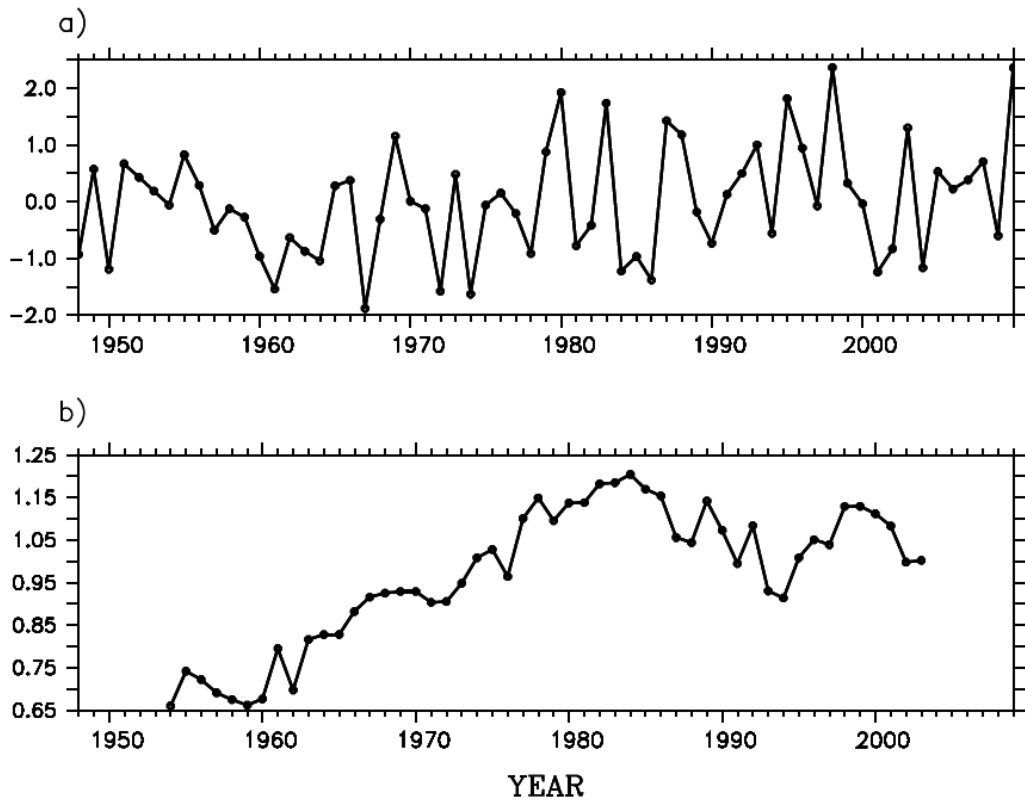


Figure 5.17 a) The normalized WNPSH index (JJA) during 1948-2009 from NCEP-NCAR reanalysis dataset (Kalnay et al. 1996). b) The standard deviation of the WNPSH index with a 13-year window that moves year by year.